Strategies for Monitoring Pathologic Conditions and Treatment Efficacy in Murine Models

by

Andrew David Brannen

A dissertation submitted to the Graduate Faculty of
Auburn University
in partial fulfillment of the
requirements for the Degree of
Doctor of Philosophy

Auburn, Alabama
December 10, 2016

Keywords: *Staphylococcus aureus* Pathogenesis, *in vivo* Molecular Imaging, Multi-angle Bioluminescence Imaging, *Bacillus amyloliquefaciens* AP183

Approved by

Peter R. Panizzi, Chair, Associate Professor of Department of Drug Discovery and Development
Robert D. Arnold, Associate Professor of Department of Drug Discovery and Development
Jianzhong Shen, Associate Professor of Department of Drug Discovery and Development
Jack DeRuiter, Professor of Department of Drug Discovery and Development
Mark R. Liles, Professor of Biological Sciences

Abstract

On the surface, the pathologies of infectious disease and cancer appear fundamentally different; however, there exist several commonalities including pharmacological targets and resistance mechanisms, immune response, and the role of commensal microbes for response to therapeutic intervention. The lessons learned from each of these pathologies can provide valuable insights which may benefit preclinical research as a whole. This dissertation represents the work of three distinct, but interrelated projects with the central focus on strategies for monitoring pathologic conditions and novel treatment efficacy of *Staphylococcus aureus* (*S. aureus*) infection and an improved method for monitoring longitudinal progression of cancer in preclinical models. Specifically, (1) the development of a device for semi-automated multi-angle *in vivo* bioluminescence, fluorescence, and X-ray imaging, (2) the efficacy of a novel probiotic, *Bacillus amyloliquefaciens* strain AP183, for the biocontrol of cutaneous *S. aureus* infection, and (3) investigation of species-specificity of *S. aureus* strains through bioinformatics and biochemical tests involving the prothrombin activator staphylocoagulase. In Chapter 2, we demonstrate the utility of our in-house developed system for multi-angle rotational optical imaging which we showed improved the accuracy and consistency of longitudinal bioluminescence imaging datasets in a model of prostate cancer. In Chapter 3, we evaluated the efficacy of a novel probiotic microorganism *B. amyloliquefaciens* strain AP183 for inhibiting *S. aureus* infection *in vivo* in a cutaneous wound model. And, in Chapter 4, we present new evidence that elucidates the mechanism of *S. aureus* clotting preference to specific host species.

Acknowledgments

I would like to express my sincere gratitude to the many special people who have encouraged and supported me throughout my graduate studies. First, to my amazing wife, Lindsey Kay Brannen, for her unwavering love, support, and patience during all of the triumphs and tribulations of my graduate studies. I am thankful for my parents, Don and Beth, and my little sisters, Lindsey and Amanda, who have been a continuous source of encouragement, guidance, and inspiration. I am thankful to the many wonderful colleagues and friends that have supported me along the way, especially Dr. Richard Davis, Dr. Jiansheng Huang, Dr. Shamima Nasrin, Mary Smith, Amber Milton, Aziz Al Mouslem, Matt Eggert, and Tareq Anani. A special thanks to my dear friends Chris and Sherry Smith for their generosity and support. I am grateful to my mentor Dr. Peter Panizzi and my graduate committee, Dr. Mark Liles, Dr. Jianzhong Shen, Dr. Jack DeRuiter, and Dr. Robert Arnold for their time, dedication, and guidance. Thank you to all of the wonderful staff at the Harrison School of Pharmacy for the hard work and dedication. I would also like to thank Dr. Bruce Smith and the Auburn University Research Initiative in Cancer for the generous financial support during my graduate fellowship. Thanks also to the many collaborators that have made this research possible.

Table of Contents

List of Tables

List of Figures

1. Of Mice and Men: Murine Models of Bacterial Infection and Cancer in the Preclinical Research Pipeline

Introduction

Many sources in the literature draw parallels between the pathologies of infectious disease and cancer and, indeed, there exist several surprising commonalities among the two pathologies including pharmacological targets and resistance mechanisms, immune response, and the role of commensal microbes for response to therapeutic intervention [1-4]. While there has been much discussion over the similarities and differences among neoplastic and infectious pathologies, little has been discussed regarding commonalities of the animal models used to study these disease states in the preclinical setting. Animal models are a mainstay of the preclinical research pipeline and much effort has been made to best replicate the human condition of disease, particularly in mouse models. Despite these efforts, however, shortcomings of animal models are often blamed for the low success-rate of translational drug development, particularly with development of novel anti-neoplastic therapeutics where 85% of drugs fail in early clinical trials and only half of those remaining earn approval for clinical use [5-7]. Further, ethical considerations call for continuous reduction, refinement, and replacement for these models wherever possible [10]. Studying the parallels between murine models of infectious disease and cancer may serve as a fruitful source for improvements in animal models for each pathology. Therefore, this chapter will compare and contrast the mechanisms of infectious and neoplastic conditions, leading into a discussion of the current state of murine models used to study each pathology and the technology for monitoring their respective pathologic conditions in the preclinical setting.

Common Pharmacological Mechanisms of Anti-neoplastic and Antibiotic Drugs

Bacterial infection and cancer are each characterized by a rapid, uncontrolled growth of cells. Accordingly, therapeutic development has often targeted biological mechanisms that support the rapid growth of bacterial or neoplastic cells, specifically DNA replication, RNA synthesis, and protein translation. While antimicrobials have the benefit of molecularly-distinct targets for interruption of these processes, classical chemotherapeutic targets are often non-specific, resulting in damage to normal host tissues as a side-effect of treatment. As an example, fluoroquinolones interrupt DNA replication of bacteria by inhibiting prokaryotic topoisomerase II (DNA gyrase). Similarly, anthracyclines, such as doxorubicin, inhibit eukaryotic topoisomerase II function by targeting cells undergoing division [12]. However, anthracyclines are somewhat indiscriminate and equally affect neoplastic cells and those that divide under normal physiological conditions, leading to such well-known side effects as hair loss and infertility [12]. This problem has been the driving force behind research into controlled release formulations and targeting of tumor-specific ligands for improved drug delivery and selectivity to malignant cells [13-15]. Other drugs, namely sulfonamide and trimethoprim antibiotics and methotrexate anti-neoplastic drugs, target DNA synthesis through inhibition of folate pathways, specifically inhibition of dihydrofolate reductase [12]. RNA synthesis and protein expression are common targets of many antibiotic and anti-neoplastic drugs. Rifampin inhibits RNA polymerase and drugs such as tetracyclines and aminoglycosides inhibit the bacterial 30S ribosomal subunit, with others such as macrolides, linezolids, and clindamycin targeting the 50S ribosomal subunit. Specific targeting of protein expression in neoplastic cells is more challenging because of the necessity of this process for many cell types under normal conditions. However, *L*-asparaginase is one example that has had remarkable success in the treatment of acute lymphoblastic leukemia, owing to its unique

mechanism involving the deamination of asparagine that has been found to be a critical process of lymphoblastic proliferation [16].

Drug resistance has become a topic of great concern in both the treatment of infection and cancer. Interestingly, the mechanisms of resistance are often similar, as are the strategies for combatting resistance. In a popular review published in *Cell,* Glickman and Sawyers describe four major resistance mechanisms common among infectious and neoplastic pathologies [3]. In brief, these mechanisms include 1) drug target mutation, 2) bypass pathways, 3) drug modification or destruction, 4) and intrinsic, or tolerant persister cells. Further, resistance can be developed to a particular drug through multiple different mechanisms. For example, fluoroquinolone resistance can be incurred through a number of gene mutations encoding DNA gyrases, active efflux of drug from the cell, or through reduced permeability from changes in membrane structure [17, 18]. Similarly, many cancers have demonstrated resistance to anthracyclines through several distinct mechanisms including expression of altered topoisomerase II, as well as active efflux pumps, most notably P-glycoprotein which is associated with the "classical" multidrug resistance phenotype in a variety of cancers [19, 20].

Drug resistance is a major problem in the treatment of both infectious and neoplastic disease. However, the development of successful antibiotic and anti-neoplastic drugs has been stifled in recent years, albeit for different reasons. Despite tremendous expenditures from governmental and private industry on the development of new cancer therapeutics, 85% of novel drugs fail in early clinical trials and only half of those remaining earn approval for clinical use [6, 7]. The failings of novel anti-cancer drugs in clinical trials are often blamed on inadequate preclinical murine models as predictors of success, with the average successful translation from animal models to humans at less than 8% [5-7]. On the other hand, despite the alarming rise of

multi-drug resistant pathogens such as methicillin-resistant *Staphylococcus aureus* (MRSA), vancomycin-resistant *Enterococci* (VRE), and *Clostridium difficile*, the development of novel antibiotic compounds has stifled over recent years due primarily to decreased governmental funding and divestment of large pharmaceutical companies from antimicrobial research and development [21-23]. However, the *National Action Plan for Combatting Antibiotic Resistant Bacteria*, a recent initiative from the White House, has renewed interest in research and development of novel antimicrobials. The failings of new anti-neoplastic drugs in clinical trials illustrates the inherent need for improved animal models in the preclinical pipeline and may foreshadow the fate of future trials of novel antibiotic compounds if improved models are not implemented.

Murine Models of Bacterial Infection and Cancer in Preclinical Research

The ideal animal model is one that best replicates the phenotype of human disease. Murine models are often favored in preclinical research despite the many differences that exist between mice and men. Some sources in the literature argue that mice are poor models of human disease due to differences in genetic, immunologic, and cellular makeup and attribute these differences to the high failure rate of novel anti-neoplastic therapeutics in clinical trials [6, 7]. However, the use of mouse models in preclinical drug discovery and development cannot be easily dismissed, as there are currently no proven alternatives which adequately replicate the complexities of pathophysiology or pharmacokinetics on a whole-organism level. Until which time suitable alternatives are available, testing in animal models will remain a necessary step preceding clinical trials. Therefore, it is imperative that we continue to refine animal models to best predict drug efficacy and safety prior to human testing.

There are a variety of models currently employed in drug discovery and development efforts for bacterial infection and cancer. For human cancer models, immune-compromised mice are typically necessary to prevent rejection of implanted human xenograft tumors. The athymic nude mouse was first reported in 1962 and marked the beginning of the use of immune compromised mouse models for xenotransplantation [24, 25]. The NCr-nude mouse (NCr-*Foxn1*^{nu}) is a common model for xenotransplantation of various cancers and was discovered through a spontaneous homozygous mutation of *Foxn1*, causing hairlessness and impaired thymus generation, ultimately resulting in the inability of the mouse to produce functional T-lymphocytes [26, 27]. Further advances in xenotransplantation were made possible through the discovery of an autosomal recessive mutation (*Prkdc*^{scid}) which resulted in mice with severe deficiencies of B and T lymphocytes, referred to as severe combined immunodeficiency (SCID) mice [26, 28]. These developments have allowed for high levels of xenotransplantation and engraftment of human hematopoietic stem cells (HSCs) to better replicate human pathophysiology and immune response in preclinical murine models. For a comprehensive review of humanized mouse models in biomedical research, see Shultz *et. al.* 2007 [26]. The advent of these humanized mouse models may lead to improvements in translational anti-neoplastic drug development efforts, particularly in late-stage preclinical trials. Humanized mice have also been instrumental in modeling certain infectious diseases where human lymphocytes are the targets of infection, particularly human immunodeficiency virus (HIV) which targets T-cells [29-31]. However, intact immune systems are often critical for meaningful study of bacterial infection and as such, mouse strains such as C57BL/6 and BALB/c are most commonly used. Although, recent interest has emerged for the use of humanized mouse models for the study of *Salmonella typhi* and *Mycobacterium tuberculosis* infections [32-37].

The methods for disease establishment in laboratory animals is the focus of frequent debate as well, especially for models of human cancers. The classical "gold standard" of preclinical cancer models has involved subcutaneous implantation of human tumor cell lines on the flank of athymic nude mice. This model has the advantage of rapid tumor measurement by calipers to assess growth and response to therapy, particularly for large cohorts of mice. However, this model is frequently criticized, and the paradigm of cancer research is currently shifting towards orthotopic patient-derived xenografts (PDX) and humanized mouse models to better replicate the conditions of individual cancers [25, 38, 39]. Orthotopic cancer models come with their own sets of challenges though, as tumor size often cannot be determined through caliper measurement. Therefore, these models must frequently rely on *in vivo* imaging strategies for routine assessments of tumor growth and response to therapeutic intervention.

Similar to orthotopic models in cancer, some specialized models of bacterial infection have been developed to replicate specific pathological events, such as endocarditis [40]. In this model, the aortic valve is damaged using a suture inserted through the right carotid artery, followed by tail-vein injection of *Staphylococcus aureus* which establishes infection on the damaged valve. Another example is the intracisternal (IC) injection of meningitis-causative pathogens, such as *Streptococcus pneumoniae,* to replicate bacterial meningitis in animal models [41]. Other common models of bacterial infection include subcutaneous injection (often for cutaneous-resident opportunistic pathogens such as *S. aureus*) [42], tail-vein injection (bacteremia and sepsis models) [43], and intra-muscular injection (e.g. necrotizing fasciitis by *Streptococcus pyogenes*) [44].

Molecular Imaging Strategies for Monitoring Pathologic Conditions and Treatment Efficacy in Murine Models

Tracking of tumor growth in pre-clinical cancer studies in mice is essential for assessing the efficacy of new cancer therapies. In the past, manual caliper measurements have been the "gold standard" for monitoring changes in subcutaneous xenograft tumors over time. Yet, this method is often inconsistent, resulting in high standard deviations between independent measures among observers as a function of tumors size [45] and due to the inability of observers to access all dimensions of the tumor. Models of bacterial infection, however, frequently rely on reporters such as fluorescent proteins and bioluminescent cell lines for tracking of infection progress.

Of late, several imaging modalities, such as contrast enhanced micro-computed tomography (μCT) and magnetic resonance imaging (MRI), have shown potential for accurate measures of tumor volume, especially within the body of the animal [46]. However, limited access broadly to these technologies and the significant expense incurred acquiring of these type datasets reduces the frequency of use by cancer researchers. Ultrasound-based imaging modalities have a lower barrier-to-entry than these modalities and may address this gap in capabilities [47]. However, these technologies have limited utility for infectious disease research except in specialized models of infection such as osteomyelitis [48].

In some instances, researchers have been utilizing surrogate signals to approximate tumor volumes and monitor bacterial infection *in vivo*. These techniques include optical imaging approaches, such as bioluminescence and fluorescence (fluorescence reflectance imaging (FRI) and fluorescence molecular tomography (FMT)) and radiologic methods such as single positron emissions computed tomography (SPECT) and positron emissions tomography (PET). Other hybrid technologies also exist such as photo-acoustic systems, including the multispectral opto-

acoustic tomography (MSOT) and Vevo LAZR systems. These modalities use the absorptive properties of endogenous chromophores and exogenous probes to measure signal deep within the animals [49].

Use of bioluminescence imaging (BLI) in pre-clinical studies of bacterial infection and cancer is common and, in general, is used to track infection, tumor growth, and treatment efficacy [50]. Traditional *in vivo* BLI is a 2-dimensional planar summation of the signal of interest and there is no capacity to equate volumes from these measures. However, the approach is quite attractive as the animal is given a luciferase-expressing tumor and the subcutaneous administration of substrate luciferin generates a burst of light only at the site of positive-luciferase cancer cells. Bioluminescent bacteria do not necessitate exogenous luciferin, as expression of both luciferase and luciferin can be accomplished simultaneously, resulting in constitutively-active production of light.

Despite its appeal, there are a number of biases that exist for BLI, such as the availability of both ATP and presence of molecular oxygen in the proximity of the bacterial or tumor cell, and the physical orientation of the bioluminescent signal relative to the detector. For cancer, the former maybe primarily affected by the presence of a defined vasculature or vascular mimicry that would aid in providing ample luciferin substrate, oxygen, and ATP to the luciferase containing cell for conversion to light [51-54]. The physical location of the signal is another difficulty that has profound impact on BLI. As light moves through the animal, there is a scattering effect due to the inherent properties of tissue as a non-homogenous medium for light propagation and diminished intensity caused by the absorptive properties of blood, fat, and muscle [55]. The positioning of the animal relative to the detector further complicates BLI. For example, the image obtained from a tumor or infection on the back of an animal would be dramatically different if the detector was

positioned in front or behind the animal. These tissue scattering considerations make longitudinal studies challenging as the positioning needs to be consistent among all time points in a dataset for optimal results. Fluorescence imaging is not immune to these problems and, in fact, the light-scattering doubly affects fluorescence imaging from a source deep within an animal, as light is scattered from both the excitation and emission independently [46]. To address positional bias, researchers often manually orient the animal and acquire multiple images in an attempt to find the optimal orientation for each time point. This process is tedious and subjective without a standardized means for acquisition of multiple angles. Chapter 2 discusses a method for semi-automated multi-angle BLI acquisition to alleviate positional bias in longitudinal imaging studies.

Conclusions

There exist many commonalities between the pathologies of infectious disease and cancer and many sources in the literature draw parallels between the basic biology, pharmacology, immunological response, and therapeutic resistance mechanisms between the two. However, no sources have specifically discussed the animal models used for each pathology in the preclinical setting. The failings of novel anti-neoplastic drugs in late clinical trials is often blamed on inadequate animal models as predictors of drug success in regards to safety and efficacy. Preclinical models for infectious disease research are often highly successful, but the lack of governmental funding and divestment of pharmaceutical companies has stifled novel antibiotic development despite the urgent need for new antibiotics to combat microbial pathogens resistant to existing antibiotics. This chapter discussed some of the current models used for both infectious disease and cancer and the methods for monitoring their respective pathologic conditions in the same context with the hopes that lessons may be learned from each that can benefit the other.

2. Correlation of 360-degree *In Vivo* Bioluminescence with Multi-Spectral Optoacoustic Tomography in a Murine Cancer Model

Introduction

Routine tracking of tumor growth in mice is an essential component of most pre-clinical cancer studies. In the past, caliper measurements have been the "gold standard" for monitoring development of subcutaneously implanted tumors over time. While these measures can establish trends, they often suffer from inherently high relative standard deviations caused by the inability to circumvent the true periphery of the tumor in a living animal and variability in the shape of the tumors [45, 56]. Specifically, observers can easily measure the length and width of a tumor (x and y axis), although the depth (or z-axis) cannot be accurately determined by caliper measurements without resecting the tumor. To account for this problem, subcutaneously implanted tumors are often presumed to be ellipsoidal in shape, with volumes often calculated with the assumption that the z-axis is equal to the shorter of the x/y axis dimensions [46, 47, 57]. However, this assumption often does not reflect the true morphology of implanted tumors and thereby results in noisy tumor development progress curves and, ultimately, higher animal usage in comparative studies in order to reach a measure of statistical power.

The advent of contrast-enhanced micro-computed tomography (μCT) and magnetic resonance imaging (MRI) has revolutionized tumor volume determination along the continuum of disease progression [46, 58]. However, both modalities have their inherent weaknesses. CT requires ionizing radiation and strict requirement for the use of exogenous agents to deliver soft tissue contrast to define the tumor borders. MR imaging requires longer acquisition times and increased budgetary considerations, especially for routine measurements of tumor size in large

cohorts of animals [47]. Furthermore, there is limited access to these technologies in most academic settings and vivarium, thereby limiting the utility of both modalities for routine assessment of tumor volume. The use of surrogate signals to approximate tumor volumes is an attractive alternative to quantifying tumor size and response to therapy. These techniques include optical imaging approaches, such as bioluminescence, fluorescence (fluorescence reflectance imaging (FRI) and fluorescence molecular tomography (FMT)), and radiologic methods such as single positron emission computed tomography (SPECT) and positron emission tomography (PET). Other technologies such as photo-acoustics and hybrid photo acoustic / ultrasonic imaging use the absorptive properties of endogenous chromophores for contrast whilst allowing for the detection of exogenous probes to measure signal deep within animals [49, 59].

Use of bioluminescence imaging (BLI) in pre-clinical cancer studies is a popular alternative used by many academic labs and, in general, it is used to track tumor growth and anti-cancer treatment efficacy [50]. Traditional *in vivo* BLI is a 2-dimensional planar summation of the light production and there is no capacity to equate volumes from these measures. However, BLI is quite attractive, as the animal is implanted with a luciferase-expressing tumor and the intra-peritoneal administration of substrate luciferin generates light only at the site of luciferase-positive cancer cells. This affords it a distinct advantage over calipers as tumors located within the body cavity can be monitored. Despite its appeal, BLI is limited by the availability ATP and molecular oxygen necessary to catalyze the oxidation of the luciferin and the physical location of the bioluminescent signal source within the body relative to the detector. The former is dependent on how well perfused the tumor is as it develops. The rate of tumor growth is highly-dependent on vascularity or vascular mimicry of the tumor [51, 53, 54]. These vessels or networks provide key nutrients and serve as the way in which luciferin substrate, oxygen, and ATP are supplied to

luciferase-expressing cells. The physical location of the signal is another difficulty that has profound impact on BLI. As light moves through the animal, there is a scattering effect due to the inherent properties of tissue as a non-homogenous medium for light propagation and diminished intensity caused by the absorptive properties of blood, fat, and muscle [55]. These tissue scattering considerations make longitudinal studies using BLI challenging, as the positioning of the animal needs to be relatively consistent among all time points in a given dataset for optimal results. Fluorescence imaging is not immune to these problems, in fact light-scattering doubly affects fluorescence imaging from a source deep within an animal as light is scattered from both the excitation and emission independently [46]. To address positional bias, researchers often manually orient the animal and acquire multiple images in an attempt to find the optimal orientation for each time point. This process is laborious and subjective.

The goals of this study were (1) to develop a method to improve correlations of longitudinal BLI to tumor volume by eliminating positional bias, (2) to create a method that can be quickly and cost-effectively used in many labs to create multi-angle BLI dataset around a full 360°, and (3) to validate the use of multi-spectral optoacoustic tomography (MSOT) for assessment of tumor volumes. To this end, we tracked the growth of subcutaneous prostate cancer xenografts in athymic mice by use of our in-house developed prototype for the acquisition of 360° *in vivo* BLI, namely the *Mouse Imaging Spinner* (MiSpinner) over a 9-week time course. In these animals, we evaluated standard planar BLI, MiSpinner-determined optimal angle BLI, and area under the curve (AUC) of 360° BLI and correlated these measures with volumes determined by digital caliper measurements, volumetric MSOT segmentations, and *ex vivo* digital caliper measurements. Using this approach, we show that data from multi-angle BLI correlates more significantly with measures of tumor volume than standard BLI using parametric analysis. Further, we show that volumes

determined *in silico* from MSOT scans correlate much more closely to *ex vivo* measured tumor volumes than caliper volumes.

Materials and Methods

Animals and Tumor Model

All experiments were performed in accordance to national and institutionally approved animal care and use guidelines. Xenografts of luciferase-expressing human prostate cancer cells (PC-3-Luc2 Bioware Ultra, PerkinElmer, Inc.) were established subcutaneously in the left flank of NCr nude, 6-8 week-old, male mice (Taconic Biosciences, Inc, Albany, NY). In brief, PC-3-luc2 cells, cultured routinely in F-12K medium (Mediatech, Inc.) and supplemented with 10% (v/v) fetal bovine serum (Hyclone Laboratories, Inc.) were harvested at sub-confluence using 0.25% (v/v) trypsin (Mediatech, Inc.) and collected as a suspension with complete medium. Total cells were counted, pelleted by centrifuging at 250 x*G* for five minutes, followed by media removal by aspiration and resuspension in phenol-free and serum-free F-12K media to a final concentration of $1x10^7$ cells per mL. Prior to injection, the cell suspension was mixed (1:1, v/v) with ice-cold, Matrigel (BD Biosciences). While providing 1-3% isoflurane gas (Henry-Schien) with oxygen to the mice, a 1.0 mL syringe with 26-gauge needle (BD Biosciences) was used to implant 200 µL of cell mixture ($1x10^6$ prostate cancer cells) subcutaneously into the left flank of each mouse. In total, 15 mice were used for this study.

Tumor Volume Determination from Digital Caliper Measurements

Tumor growth was assessed three times per week using digital caliper measurements of tumor x/y dimensions. Prior to imaging sessions, mice were maintained under anesthesia using 1-

3% isoflurane gas with medical grade oxygen while three independent reviewers measured tumor dimensions in order to determine a mean volume as a basis for correlation. Volumes were calculated using a standard formula, derived from the volume of an ellipsoid, *equation 2.1*.

Equation 2.1 - Caliper Tumor Volume = (π/6) ● (larger diameter) ● (smaller diameter)^2

Humane endpoints were defined as tumors that approached or exceeded 1500mm^3. Otherwise, tumors were monitored for a duration of nine weeks before mice were euthanized followed by resection of tumors. Resected tumors were measured relative to three axial dimensions of diameter and volumes were calculated using *equation 2.2.*

Equation 2.2 - Volume = (π/6) ● (diameter X) ● (diameter Y) ● (diameter Z)

MiSpinner Modified Imaging System for Bioluminescence Measurement

The MiSpinner prototype is comprised of a step motor, remote controller, and an animal holder that is connected to the standard gas anesthesia system within the imaging chamber. The motor can be programmed to turn a defined number of precise iterations within 360°, as pre-determined by the user prior to imaging. The stage connected to the motor was custom designed using 123D Design v11.2.1 (Autodesk, Inc.) and 3D printed. The animal holder is designed for single-use to prevent cross-contamination and consists of a modified polystyrene 50 mL conical tube without obvious markings (Denville Scientific, South Plainfield, NJ). The screw cap of the conical tube was punched with a centered 8x8 mm square hole for attachment to the axle of the motor. The conical end of the tube serves as a nose cone, with the end cut open to allow for gas exchange. Mice were inserted into the animal holder with the head oriented toward the conical end and stabilized by a foam cylinder wrapped around the base of the tail. The motor and animal holder were placed within the imaging chamber of the *IVIS Lumina XRMS* (PerkinElmer, Inc.) and

connected remotely to the controller and power supply on the outside of the chamber via data and power cords fed through a light-tight port. The MiSpinner system is placed inside of the imaging chamber of the *IVIS Lumina XRMS* as shown in *figure 2.1,* with the controller placed on the outside of the chamber.

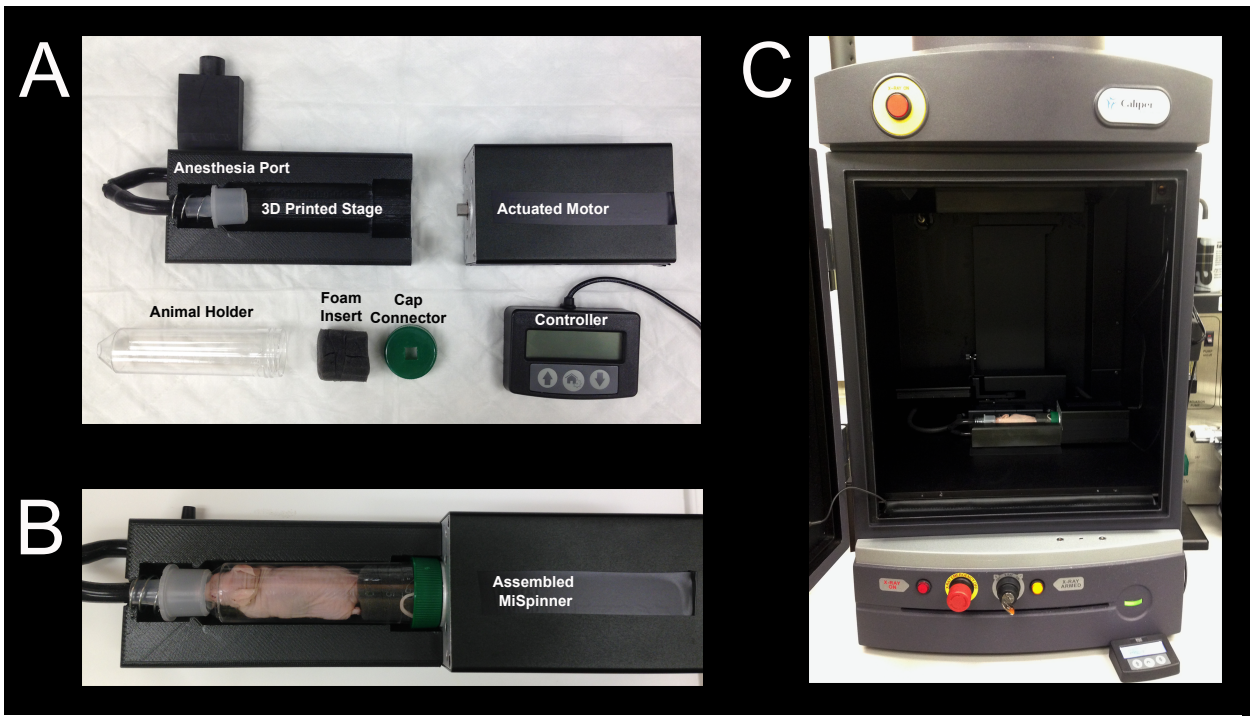

Figure 2.1. (**A**) The *MiSpinner* is comprised of a step motor attached to a custom 3D-printed stage with integrated gas anesthesia port. The animal holder consists of a polystyrene 50 mL conical tube with the conical end cut open to allow for gas flow. The cap is modified with a square hole for attachment to the axle of the motor. The mouse is oriented in the holder with the head toward the conical end and the holder is placed in on the 3D printed stage (**B**). The assembled system is placed inside the imaging chamber with the motor wired to a remote controller fed through a light-tight port on the side of the IVIS Lumina XRMS (**C**).

MSOT Acquisition and In Silico Tumor Volume Determination

MSOT imaging was performed using the *InVision 256-TF* and *ViewMSOT* v3.6.0.119 (iThera Medical GmbH). Prior to imaging, all mice were anaesthetized with 1-3% isoflurane and medical grade oxygen. Scans were performed using a 0.5 mm slice separation spanning the entire tumor region for each mouse. Light wavelengths for optoacoustic measurement included 715, 730, 760, 800, and 850 nm, with 850 nm used for anatomical background. Slices from each scan were exported from *ViewMSOT* (iThera Medical, GmbH) to *ImageJ* v2.0.0-rc-15/1.49h (https://imagej.nih.gov/ij), followed by export as TIFF hyperstack files. Tumor segmentation, *in silico* volume determinations, and 3D rendering (*figure 2.3B*) were performed using *3D Slicer* v4.5.0 (https://www.slicer.org) with the *Editor*, *Models,* and *Volume Rendering* tools, respectively.

Multi-Angle In Vivo BLI

Prior to each imaging session, three mice were chosen for a kinetic assay to determine the enzyme saturation time point, i.e. optimal imaging window during which luciferases are saturated with luciferin as evidenced by a plateau in luminescent signal. Mice were anaesthetized with medical grade oxygen supplemented with 1-3% isoflurane, injected intra-peritoneal (IP) with 500 µL of 30 mg/mL *D*-luciferin (PerkinElmer, Inc.), and kinetic assay was performed with standard bioluminescence images acquired every 30 seconds for a period of 45 minutes (data not shown). The following day, mice were injected IP with 500 µL of 30 mg/mL *D*-luciferin and standard BLI was performed at the beginning of the saturation point, immediately followed by 360° BLI using the *MiSpinner* with 15° intervals (24 images total). Exposure time varied from 1-5 seconds (dependent on the total counts) with small binning and subject height set to 4.0 cm.

Additionally, once per week throughout a 9-week time course, a single mouse was selected for BLI with X-ray performed at precise 7.5° turns (48 images) around 360°, with results shown in *figure 2.3A*. X-ray was acquired using the high-resolution setting, 5-second exposure per image, and the scintillator swing-arm positioned to "large animal" to accommodate the *MiSpinner* system.

Analysis of a Multi-Lobular Tumor Signal Using Multi-Angle BLI

During preliminary studies, a mouse with a multi-lobular PC3-Luc2 tumor was selected for multi-angle BLI to assess differences in signal detected at different angles at a single point in time. BLI was performed at precise 7.5° intervals around 360° (48 images total). In *figure 2.2*, square ROI of equal quadrants were centered on the tumor region. The photon flux for each individual quadrant and the sum of all quadrants at each orientation were plotted against their respective degree of rotation.

360° Bioluminescent Image Processing and Statistical Analysis

Following acquisition, all images in each multi-angle dataset were loaded as a batch sequence in *Living Image* for simultaneous thresholding of luminescent signal in each acquired image. Regions of interest (ROI) were measured by the rate of photons reaching the CCD (flux), determined using rectangular ROIs (9x4 cm) placed in the exact location around the animal across all degrees of rotation and time points. Bioluminescent flux from each ROI was plotted against the relative degrees of rotation for each respective dataset. AUC and optimal BLI angle were determined for each dataset using the "area-under-the-curve" and "column statistics" functions in *Prism 6* (GraphPad Software Inc.). Correlations among caliper determined tumor volumes, MSOT *in silico* determined tumor volumes, AUC, optimal Angle BLI, and standard BLI were assessed

using parametric (Pearson) and non-parametric (Spearman Rank) analysis in *Prism 6. A linear* fit model is denoted by a solid black line for each respective correlation plot. *Ex vivo* volumes are indicated by red circles and the respective linear fit is shown by a dashed red line. Six mice with implanted tumors that failed to grow beyond a threshold greater than 700mm^3 after 9 weeks were excluded from this study. Also excluded was a mouse possessing a highly irregular tumor morphology and a mouse who died shortly after the implantation procedure.

Video Production

Video files (not shown) were compiled by loading all images from each 360° dataset into a sequence, equalizing the parameters and scale across all frames using *Living Image* v4.4.17106 (PerkinElmer Inc.). All frames were exported from *Living Image* as TIFF files. Next, images were loaded into *ImageJ* (v2.0.0-rc-15/1.49h) as sequential image files, cropped, and exported as an animated ".gif" file (data not shown).

Results

Multi-Angle BLI Demonstration of Positional Bias

In *figure 2.2A,* a multi-lobular tumor was imaged at 7.5° intervals around a 360° centralized axis. Images are shown at 15° intervals to demonstrate the difference in overall signal intensity at each orientation. Qualitatively, the appearance of signal varies drastically with minor changes in orientation. The differences in morphology of luminescent signal are further demonstrated in *figure 2.2B*. At 90°, the tumor appears to be a single large lobe with a potentially smaller lobe slightly superior to the major lobe. However, at 135° the morphology of the tumor appears as two distinct major lobes, with a small third lobe visible. To quantitate the differences in signal, four

ROIs were arranged in quadrants centered on the tumor region. The resulting flux data for each quadrant and the sum of all quadrants is plotted against the relative degrees of rotation in *figure 2.2C*. Dashed lines correspond to the 90° and 135° images in *figure 2.2B.* Two distinct peaks of signal were observed in the sum of all quadrants, corresponding with each of the two major lobes. The multi-lobular morphology of signal in this tumor resulted in the optimal angle at 135°, where the signal is most evenly dispersed across the quadrants.

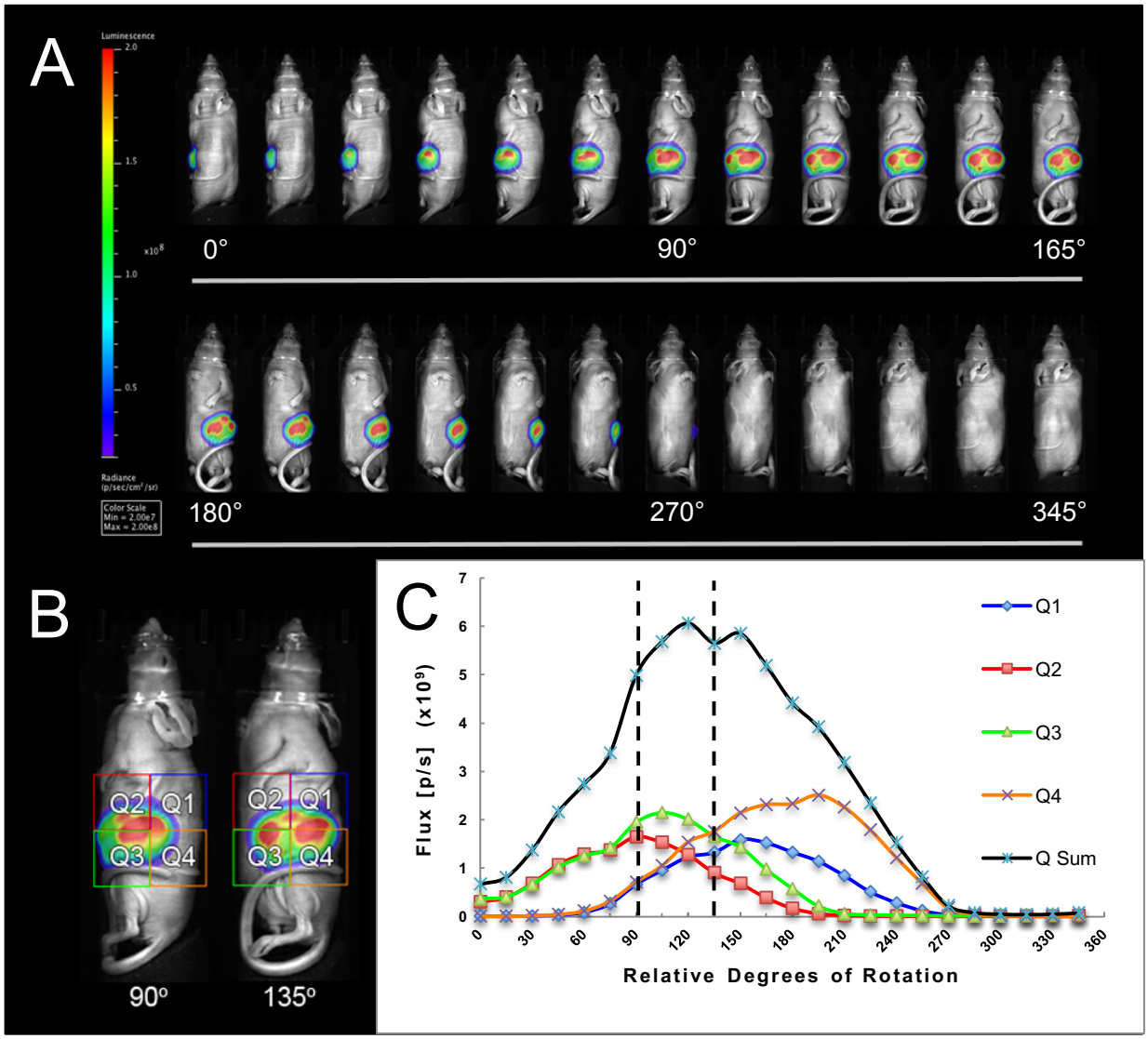

Figure 2.2. Multi-angle BLI of a multi-lobular PC3-Luc subcutaneous tumor in NRC-Nu mouse shown at 15° intervals around 360° (**A**). Two intervals (90° and 135°) are presented with ROI sampling divided into quadrants (**B**) and corresponding signal plotted against the degrees of rotation with corresponding 90° and 135° signal indicated by dashed lines (**C**).

Longitudinal Assessment of Tumor Growth with Multi-Angle BLI

To demonstrate the longitudinal tracking of tumor growth with multi-angle BLI, one mouse is shown in *figure 2.3A* at bi-weekly time points with the optimal imaging angle (peak luminescent flux) shown overlaid on X-ray. MSOT scans were also acquired at corresponding time points. The longitudinal 360° flux curves are shown in *figure 2.3C* with the optimal imaging angle denoted by an asterisk. *Figure 2.3C* shows normalized longitudinal tumor growth of n=7 mice assessed by caliper volumes, MSOT volumes, optimal angle BLI, and 360° area under the curve. Corresponding Pearson correlation values are shown in *Table 2.1*.

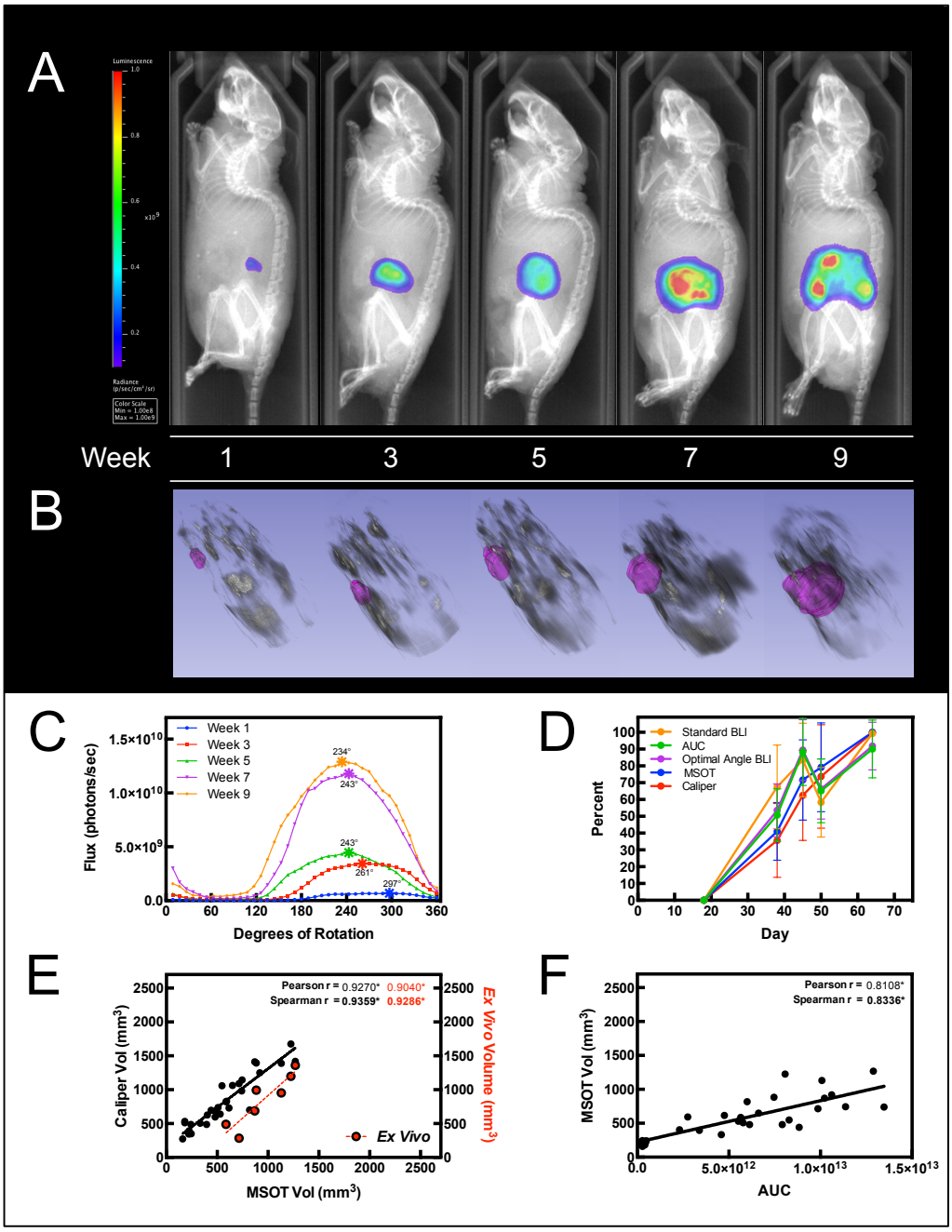

Figure 2.3. Longitudinal imaging of subcutaneous PC3-Luc implanted tumors using 360° BLI and MSOT. (**A**) MiSpinner determined optimal angle of rotation (peak luminescent flux) overlaid on X-ray at bi-weekly time points. (**B**) Longitudinal tumor segmentations superimposed on 3D rendering of MSOT scans with 850 nm background signal. (**C**) Luminescent flux is plotted against the relative degrees of rotation with respective peak angles denoted by (*). (**D**) Normalized longitudinal growth of n=7 PC3-Luc subcutaneous xenograft tumors assessed by MSOT segmentation, physical caliper measurement, standard BLI, MiSpinner determined optimal angle BLI, and AUC. (**E**) Linear fit of MSOT segmented tumor volumes versus caliper volumes (solid black line) and *ex vivo* volumes (dashed red line) of n=7 mice. (**F**) Linear fit of 360° area under the curve (AUC) versus MSOT segmented tumor volumes and *ex vivo* tumor volumes.

Multi-Angle BLI Correlates More Significantly with Tumor Volume than Standard BLI

To assess the utility of multi-angle BLI for longitudinal tumor growth, an expanded study with n=7 mice was implemented. *Figure 3E* demonstrates the linear fit of MSOT determined tumor volumes with caliper determined volumes. *Ex vivo* volumes are represented in red and plotted against MSOT volumes with fit denoted by red dashed line. The results of standard BLI, MiSpinner determined optimal angle BLI, and AUC linear correlations to caliper and MSOT volumes are shown in *table 2.1*. MSOT determined volumes strongly correlated with *ex vivo* volume measurements (Pearson $r = 0.9040$; $p = 0.0052$). As expected, the correlation of caliper volumes with *ex vivo* volumes was poor (Pearson $r = 0.6271$; $p = 0.1318$). AUC correlated with both caliper and MSOT volumes best, but only slightly higher than optimal angle BLI. Standard BLI had the poorest correlation with caliper and MSOT volumes.

	PARAMETRIC CORRELATION (PEARSON R)	
	MSOT Volume	Caliper Volume
AUC (n=30)	0.8108 ($p < 0.0001$)	0.7930 ($p < 0.0001$)
Optimal angle BLI (n=30)	0.8073 ($p < 0.0001$)	0.7938 ($p < 0.0001$)
Standard BLI (n=30)	0.7551 ($p < 0.0001$)	0.7380 ($p < 0.0001$)
MSOT volume (n=30)	n/a	0.9270 ($p < 0.0001$)
Caliper volume (n=30)	0.9270 ($p < 0.0001$)	n/a
Ex vivo (n=7)	0.9040 ($p = 0.0052$)	0.7642 ($p = 0.0455$)

Table 2.1. Pearson correlation of longitudinal caliper volumes and *in silico* volumes from MSOT segmentation with standard BLI, optimal angle BLI using the *MiSpinner*, and AUC in a PC3-Luc subcutaneous tumor model. Endpoint *ex vivo* tumor volumes are shown with respective correlation to MSOT and caliper determined tumor volume.

Discussion

There is a distinct advantage to being able to view the source of an optical signal in an animal from multiple angles. Due to the scattering effects of light in tissue, bioluminescent and fluorescent signal intensity can vary significantly with respect to the positioning of the animal. As we demonstrate in this study, this positional bias can lead to erroneous measures of bioluminescent signal without a means of determining the optimal angle for imaging at a particular point in time, ultimately increasing the number of animals needed to achieve power in a given study.

The concept of automated acquisition of multiple angles of a subject is not novel and is the rationale from the development of imaging modalities such as Fluorescence Molecular Tomography (FMT), which allows for 3D localization of fluorescent reporters in an animal [60]. Diffuse Light Imaging Tomography (DLIT; PerkinElmer, Inc.) is one commercially available method for the IVIS Spectrum series imagers (PerkinElmer, Inc.) which acquires luminescence in a series with a sequence of filter sets which allows for surface topography and determination of luminescent signal depth with absolute intensity in 3D space. However, DLIT is limited to the IVIS Spectrum series instruments and is not possible with the more ubiquitous IVIS Lumina series and other top-mounted camera based imaging systems.

A similar modular add-on for the In Vivo MS FX PRO (Bruker Corp.), the Multimodal Animal Rotation System (MARS) rotates mice for multi-angle optical imaging by placing an animal on a transparent film with motors pulling the film, thereby facilitating rotation of the animal [61, 62]. However, because the MARS is designed for bottom-mounted camera systems, it is not compatible with top-mounted fluorescence reflectance optical imaging systems such as the IVIS Lumina XRMS (PerkinElmer, Inc.). Further, the design of the MARS does not secure the animal

in place during the rotation process and as such, there is considerable movement of the limbs and no defined central axis of rotation.

In this study, we utilized a similar approach to multi-angle BLI using our *MiSpinner* system. Our method uses a cylindrical polystyrene animal holder which fits snugly around the animal and is further stabilized by a foam insert that is wrapped around the base of the tail, resulting in consistent positioning between time points in longitudinal studies. Further, we observed that this animal holder design minimized movement during the rotation process while maintaining a central axis. For the purposes of this study, only one mouse was imaged at a time, however, there is sufficient space within the field of view of the *IVIS Lumina XRMS* for multiple mice to be imaged simultaneously using this method.

The results of this study demonstrate that bioluminescent signal can vary widely with relatively minor changes in orientation of the signal source. Further, our results indicate that the optimal angle for BLI can change unpredictably as tumor growth progresses. In *figure 2.3A*, the progression of tumor growth was assessed by multi-angle BLI shown at bi-weekly time points with the optimal angle of rotation shown for each. Using the skeletal structure for anatomical landmarks, the angle of maximum flux is consistent during the early stages of tumor progression (weeks 1-5). However, once the tumor progressed in size, the angle with peak luminescent signal is noticeably altered. We believe that as the tumor became more burdensome (weeks 7-9) the increased weight caused it to sag, thereby resulting in a change of the orientation with peak bioluminescent signal. By using multi-angle BLI, we were able to quantitatively determine the optimal angle for longitudinal comparisons despite the shift in tumor position. Further, by week 9, we believe the tumor began to develop necrotic regions which altered the luminescent signal

morphology and by using the peak luminescent angle, we were still able to quantitatively determine the optimal angle for BLI for comparison to previous time points.

With an expanded study of 7 mice, we monitored tumor progression longitudinally using standard BLI and 360° multi-angle BLI, with volumes monitored by traditional caliper measurements and segmentation from MSOT scans. We show that MSOT segmented volumes correlated with endpoint *ex vivo* volumes with a high degree of significance (Pearson r = 0.9040; $p = 0.0052$), while caliper volumes correlated poorly in comparison (Pearson r = 0.7642; $p = 0.0455$). This result indicated that MSOT segmented tumor volume provided a more true representation of actual tumor volume and would be more suitable for the purposes of correlating longitudinal measures of BLI. Indeed, our results indicated a significant improvement in correlation of BLI data with MOST segmented volumes than caliper volumes.

While assessing 360° luminescence curves from our datasets, we noticed from our 360° BLI plots that both the height and breadth of signal increased as tumors progressed in size. This observation led us to begin analyzing the area under the curve at each time point with the belief that we may be able to further improve correlations with tumor volume. We found that while the optimal angle BLI correlated more significantly with tumor volumes than standard BLI (Pearson r = 0.8073 and 0.7551 respectively, with $p < 0.0001$ for both), correlations improved further using the AUC (Pearson r = 0.8108, $p < 0.0001$). While the improved correlation of AUC versus optimal angle BLI was marginal, we believe that the AUC measures may be less sensitive to error and may provide a more reliable means for assessment.

With the paradigm of cancer research shifting towards orthotopic and metastatic models, multi-angle BLI may also be a useful tool for localizing metastasis and assessing tumor growth

and regression in preclinical models that better reflect human disease. Future studies will assess the utility of multi-angle BLI using the *MiSpinner* for these purposes.

Using the *MiSpinner* system, we effectively eliminated positional bias associated with standard planar BLI and provided a means for standardizing animal placement for longitudinal studies of preclinical cancer models. Further, we are able to determine the optimal acquisition angle for each time point and show significant improvement in correlation with tumor volume. We believe that multi-angle BLI may be a useful tool for high-throughput assessment of tumor growth and regression in relevant preclinical orthotopic and metastatic models of cancer, particularly for research groups where other imaging modalities are cost-prohibitive.

3. Novel Soil-Derived *Bacillus amyloliquefaciens* Strain AP183 Inhibits *Staphylococcus aureus* Colonization in Cutaneous Wound Model

Introduction

The integument is host to a diverse biome of microorganisms and serves as a physical barrier between host and pathogens [63]. Damage to the integument from injury or other means creates an opportunity for pathogens to colonize the wound site and often precedes systemic infection. Indeed, the point of entry for the common opportunistic pathogen *Staphylococcus aureus* (*S. aureus*) is often through damaged skin and soft tissues, stemming either from injury or surgical procedures [64]. Asymptomatic carriage of *S. aureus* in humans is estimated to be approximately 20 percent, though the pathogen is common to a variety of acute and chronic skin pathologies including impetigo, cellulitis, furuncles, scalded skin syndrome, and mastitis [65, 66]. Cutaneous infections are burdensome in agriculture as well, with bovine mastitis alone boasting an estimated annual cost exceeding $1.7 billion on the dairy industry and *S. aureus* as the causative pathogen in 20% of cases [67]. Colonization of *S. aureus* in wound sites can lead to systemic infection and result in life-threatening conditions such as acute endocarditis, of which *S. aureus* is the leading cause with a mortality rate reported to be as high as 47 percent [68, 69].

The rise of antibiotic resistance among *S. aureus* strains is of particular concern and is the result of antibiotic resistance gene acquisition through mobile genetic elements [70]. More than 80,000 severe infections from methicillin-resistant *Staphylococcus aureus* (MRSA) and over 11,000 deaths were reported in the United States in 2011 alone [22]. The greatest contributing factor to antibiotic resistance is the inappropriate use of antibiotics and their unfounded widespread use for promoting livestock growth [22, 71]. While antibiotics are among the most highly

prescribed drugs in the world, it is estimated that in 50 percent of cases antibiotics are unnecessary or are ineffective as prescribed [22]. While approximately 2 percent of the population are carriers of MRSA, several recent studies have reported a significantly increased risk of carriage and infection from livestock-associated MRSA and multi-drug resistant *Staphylococcus aureus* (MDRSA) strains in swine farmers [72-76]. While studies vary, the carriage of MRSA and MDRSA in swine farmers has been shown to be greater than 10 percent, leading to concerns over food safety and the potential risk of spread to the general population [75, 76]. Mounting concerns have recently led to updated guidance for antibiotic use in livestock by the Food and Drug Administration, including a federal government initiative to eliminate the use of antibiotics in livestock for growth purposes. The rapidly-growing threat of antibiotic resistant pathogens and the impending restrictions on antibiotic use in livestock illustrate the need for innovative strategies for controlling the spread of antibiotic resistant pathogens.

As resistance to clinically-relevant antibiotics rises among many prevalent pathogens, approval of new antibiotics for human use has been sparse in the last few decades [21-23]. However, a renewed focus on developing innovative and effective strategies for combating antibiotic resistant bacteria has recently emerged. In addition to the development of new antibiotics, there is rising interest in the use of biocontrol agents as a means of preventing the colonization of pathogenic bacteria. The use of non-pathogenic bacteria producing natural antimicrobial compounds have been shown to be efficacious for controlling pathogens in horticulture and aquaculture applications [77-79]. *Bacillus spp.*, in particular, have been a fruitful source of novel antimicrobial natural products and may ultimately have widespread biocontrol applications in both agriculture and medicine [79-83]. In particular, *Bacillus amyloliquefaciens* (*B. amyloliquefaciens*), a plant growth-promoting rhizobacterium belonging to the *Bacillus subtilis*

group, are noted for their production of novel bioactive compounds and have been used as biocontrol agents for plant and animal pathogens in agriculture and aquaculture [79, 84-86]. *B. amyloliquefaciens* is not associated with human or animal disease and has demonstrated many beneficial properties including enhancement of immune response to pathogens and restoration of natural flora [87-89]. Although strains of *B. amyloliquefaciens* have been commercialized for use with crops, livestock, and as probiotics for human consumption, they have only recently been examined for potential in clinical application [90, 91]. A study by Geeraerts *et. al.* 2015 recently demonstrated the efficacy of a strain of *B. amyloliquefaciens* as a prophylactic measure for preventing *Clostridium difficile* colonization in a mouse model [92]. However, the use of *B. amyloliquefaciens* to inhibit wound colonization by *S. aureus in vivo* has not been reported to date.

Here, we present the first *in vivo* study demonstrating the inhibition of *S. aureus* in a cutaneous wound model by *B. amyloliquefaciens*. As previously described (see Nasrin, 2015), *B. amyloliquefaciens* subsp. *plantarum* strain AP183 (*B. amyloliquefaciens* AP183) was selected from a screening of 177 *Bacillus spp.* for its potent antimicrobial activity and was characterized by its production of a novel macrodiolide, Bacillusin A, with highly bactericidal activity against MRSA and vancomycin resistant *Enterococcus faecium* (VRE) [93, 94]. Due to the predilection of *S. aureus* for wound colonization, we sought to determine the efficacy of *B. amyloliquefaciens* AP183 for inhibiting the colonization of *S. aureus* in an *in vivo* wound model. Mice were challenged with luciferase-expressing *S. aureus* Xen29 in two wounds (upper back between shoulder blades and lower back) The upper wound served as the treatment group with co-administration of *B. amyloliquefaciens* AP183 while the lower wound served as an internal control. Two mice were selected for controls with no treatment in either wound. At the endpoint, wounds from treated and control groups were resected and used for histological analysis by Gram and

hematoxylin and eosin (H&E) staining, CFU determination of homogenized tissue, and 16S rRNA sequencing of homogenate samples to determine relative abundance of microbial genera present in each wound sample.

Our results indicate that *B. amyloliquefaciens* AP183 was highly effective for preventing *S. aureus* Xen29 colonization at the wound site and 16S rRNA analysis indicates that the presence of *B. amyloliquefaciens* may have preserved natural flora present at the wound site. These results provide evidence of the potential of *B. amyloliquefaciens* strains to serve as potent prophylactic biocontrol agents or adjunctive therapies for cutaneous-involved *S. aureus* infections in animal systems.

Materials and Methods

Microorganisms and Growth Conditions

Commercially available *S. aureus* Xen29 (*PerkinElmer Inc., Waltham, MA*) was used for *in vivo* cutaneous wound challenge studies. *S. aureus* Xen29 from glycerol stocks stored at -80°C were streaked for isolation onto Brain-Heart Infusion (BHI; *Research Products International Corp., Mt. Prospect, IL*) agar plates containing 50 μg/mL of kanamycin monosulfate (*Research Products International Corp., Mt. Prospect, IL*) and incubated inverted for 16 hours at 37°C. Following incubation period, plates were imaged using a LAS-1000 luminescent image analyzer (FUJIFILM Corporation) to confirm bioluminescence. One colony was selected to inoculate a flask containing 50 mL of BHI with 50 μg/mL of kanamycin monosulfate. The flask was incubated at 37°C for 16 hours, shaking at 225 RPM. Bacterial solution was then centrifuged at 2200 x G for 15 minutes at room temperature. The supernatant was discarded and pellet was resuspended in 20 mL of sterile-filtered PBS, followed by centrifugation at 2200 x g for 15 minutes at room

temperature. Supernatant was again discarded and pellet was resuspended in 5 mL of sterile-filtered PBS with 10% glycerol. Serial dilutions of the bacterial suspension were diluted into sterile-filtered PBS with 10% glycerol and optical density was determined at 600 nm. Concentration of bacterial suspension was calculated using the Beer-Lambert Law, wherein the molar absorptivity constant for *S. aureus* was assumed to be 1.44×10^8 CFU/mL. Suspension was adjusted to a final concentration of approximately 1.0×10^8 CFU/mL.

Strains of *B. amyloliquefaciens* spores and metabolites used for *in viv*o challenge were prepared as described in Nasrin, 2015. In brief, one colony of each strain was inoculated into a 20 mL culture tube containing 5.0 mL of trypticase soy broth and incubated on a rotatory shaker at 200 rpm at 30°C for five days. To prepare for injection, *B. amyloliquefaciens* cultured strains were dispensed into 1.0 mL aliquots with 10% glycerol.

In Vivo Cutaneous Wound Model

Experimental protocols were reviewed, approved, and performed under regulatory supervision of Auburn University's Institutional Biosafety Committee (IBC) and Institutional Animal Care and Use Committee (IACUC). For this study, 22 female C57BL/6J mice at 6-8 weeks old were anesthetized by 1-3% isoflurane gas and hair was shaven with electronic clippers and depilated using Veet® (Reckitt Benckiser Group, Berkshire, England). Treatment groups were injected subcutaneously between the shoulder blades with a 20 μL suspension comprised of 10 μL 1.0×10^8 CFU/mL *S. aureus* Xen29 and 10 μL of 1×10^8 CFU/mL *B. amyloliquefaciens* AP183 or AP191 spores with metabolites (total of 1.0×10^6 CFUs of each strain). Internal controls were administered by subcutaneous injection of 1.0×10^6 CFUs of *S. aureus* Xen29 on the lower back. Untreated control mice were given subcutaneous injections of 1.0×10^6 CFUs of *S. aureus* Xen29

between the shoulder blades and the lower back. Further, a group of mice was administered subcutaneous injections of AP183 spores + metabolites $1x10^6$ CFU/mL between the shoulder blades and lower back and another group was injected subcutaneously with metabolites only between the shoulder blades and lower back of each animal. At the end point of the experiment, all mice were sacrificed and wound samples were harvested for histological analysis, and homogenized for CFU determination, and metagenomic analysis.

In Vivo Imaging Procedures

All *in vivo* imaging was performed using an IVIS Lumina XRMS (Caliper Life Sciences). Mice were anesthetized by 1-3% isoflurane gas and placed in the imaging chamber of the IVIS Lumina XRMS. Bioluminescence exposures were 5 minutes with medium binning, *f-2* aperture, and field of view D. All mice were imaged once per day for a period of 7 days. At the endpoint, mice were sacrificed according to IACUC protocol guidelines and wound sites were excised and stored in PBS. Wound samples were split in half, with one half embedded for histological analysis and the other half homogenized for 16S rRNA sequencing and dilutions were plated to determine final CFU/mg of tissue.

Evaluation of AP183 Formulations for In Vivo Administration

To determine the optimal formulation for administration of AP183 to wound sites, three formulations were prepared and tested *in vivo* for inhibition of *S. aureus* proliferation. AP183 spores ($1.0x10^6$ CFUs), supernatant containing AP183 metabolites without spores, and AP183 spores with supernatant ($1.0x10^6$ CFUs) were co-administered with $1.0x10^6$ CFUs *S. aureus* Xen29. Mice (n = 2 per group) were imaged for bioluminescence once a day for 6 days. At the

endpoint, mice were sacrificed by CO_2 asphyxiation and cervical dislocation. Wound tissue was resected, homogenized, and diluted followed by plating on trypticase soy agar (TSA) and incubated for 18 hours at 37 °C. *S. aureus* colonies were counted by bioluminescent imaging to determine CFU counts.

CFU Determination from Wound Homogenates

Mice were euthanized by CO_2 asphyxiation, followed by cervical dislocation. Wounds were resected, with half of the excised wounds homogenized in PBS and serial diluted for spread plating on TSA. Plates were incubated for 18 hours at 37°C and BLI was performed on each plate to allow counting of luminescent colonies and ultimately determine CFUs present in each wound. Samples of wound homogenates were also used for rRNA sequencing to determine relative abundance of microbial genera present in each wound. The other half of each wound was prepared for histological Gram and hematoxlin and eosin (H&E) staining.

Relative Abundance of Microbial Genera in Wound Homogenates by rRNA Sequencing

Following endpoint procedures, wounds for each respective treatment or control group were excised for homogenization and extraction of genomic DNA (see Nasrin, 2015) [93]. To summarize, relative abundance of microbiota present in wound homogenates was determined by extraction of genomic DNA from each wound homogenate using genomic DNA isolation kit (Ultraclean microbial DNA isolation kit, MO BIO). Genomic DNA was extracted according to the manufacturer instructions. Extracted genomic DNA was used as templates for PCR amplification of 16S rRNA genes with bar-coded “universal bacteria” primer sets. Pooled amplicons were sequenced using paired-end reads on an Illumina MiSeq and several thousand 16S rRNA

sequences were generated per sample. The trimmed sequence reads were analyzed using the QIIME pipeline and operational taxonomic units (OTU) were generated at 97% cutoff using BLASTn and compared to the curated database at the ribosomal database project [95].

Tissue Staining and Histological Analysis

Wound tissue was embedded in "clear frozen section compound (VWR International, West Chester, PA) medium and fixed by submersing in a metal container with 2-methylbutane (Alfa Aesar, Haverhill, MA) on dry ice. Sectioning was performed using a Microm HM 525 (Thermo Fisher Scientific Inc.) with a section thickness of 0.6 μM per slice. Alternating slices were stained with either the following Gram staining or H&E staining procedures. Microscopy was performed using a Zeiss Axioskop with Plan-NEOFLUAR objective lenses and Nikon Sight DS-Fi2 digital camera.

Gram staining of slides was performed by submersion in crystal violet (EMD Millipore, Billerica, MA) for 15 seconds, followed by gentle rinsing with tap water, submersion in Gram's Iodine (EMD Millipore, Billerica, MA) for 15 seconds, tap water rinse, submersion in tartrazine (EMD Millipore, Billerica, MA) solution for 15 seconds, and a final tap water rinse. Slides rinsed with 95% alcohol and allowed to dry, then dripped with xylene (EMD Millipore, Billerica, MA) and allowed to dry before a coverslip with Cytoseal™ (Thermo Fisher Scientific Inc.) was placed over each slide.

H&E staining was performed using the following procedure. Slides were submersed in hematoxylin (EMD Millipore, Billerica, MA) and placed on a rocker for 15 minutes, then rinsed in tap water with gentle shaking for 15 minutes. Slides were submersed in 95% alcohol for 30 seconds and submersed into eosin (VWR International, West Chester, PA) for 45 seconds. Slides

were then submerged into 95% alcohol for 1 minute, followed by submersion in 100% alcohol for 1 minute. Slides were then submersed in xylene for 1 minute and allowed to air dry. A coverslip with Cytoseal™ (Thermo Fisher Scientific Inc.) was then placed over each slide.

Results

Inhibition of S. aureus Xen29 Colonization in Wounds Treated with AP183

Preliminary results of *in vivo* challenge demonstrated that direct administration of AP183 spores to wounds significantly inhibited *S. aureus* Xen29 growth as compared to other *B. amyloliquefaciens* strains tested. We observed that while application of AP183 spores alone are capable of reducing *S. aureus* growth, the effectiveness was enhanced by including both the spores and the supernatant containing metabolites expressed by AP183 (*figure 3.1A-B*). Administration of AP183 spores alone had the lowest resulting effect on bioluminescent signal. AP183 supernatant containing secondary metabolites administered alone resulted in a further decrease of bioluminescent signal, while the combination of AP183 spores and supernatant had the greatest effect on decreasing bioluminescent signal from *S. aureus* Xen29.

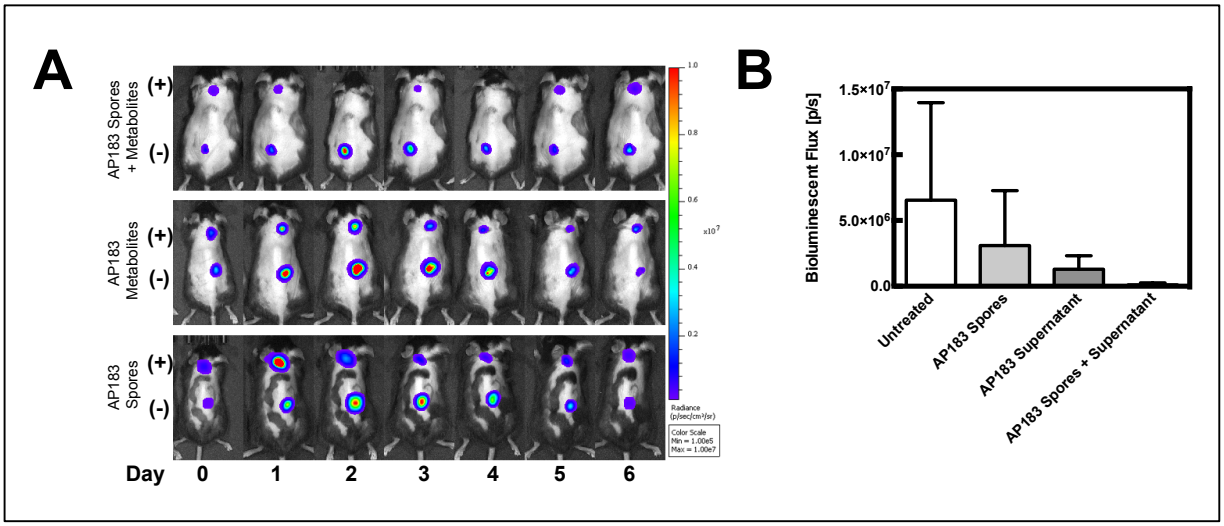

Figure 3.1. *In vivo* evaluation of *B. amyloliquefaciens* AP183 spores, supernatant (metabolites), and spores with supernatant formulations and their respective inhibition of *S. aureus* Xen29 colonization in a cutaneous wound model. (**A**) Longitudinal BLI of n=2 mice per treatment group. Upper wounds were treated with indicated formulation of AP183 **(+)** and lower wounds served as internal controls **(-)**. (**B**) Bioluminescent signal from wounds with each treatment formulation.

An expanded *in vivo* study of n=10 mice demonstrated that wounds treated with AP183 and supernatant (metabolites) resulted in a significant decrease ($P < 0.05$) of bioluminescence signal (*figure 3.2A-B*). Furthermore, we observed a significant reduction ($P < 0.05$) in the number of cultured CFUs in in homogenates corresponding to AP183 and supernatant treated wounds (*figure 3.2C*). Injection sites treated with AP191 spores and supernatant were less consistent, but still resulted in decreased bioluminescent signal overall as compared to control wounds. Bioluminescent signal in untreated control wounds peaked between days 2-3 with a substantial decrease in reported signal by the end of the study. However, one untreated control mouse succumbed to systemic infection before the end of the study, despite a substantial decrease in bioluminescent signal from wound sites. Gram staining indicated the presence of Gram positive cocci in the aorta of this mouse, providing evidence of systemic spread of the pathogen to distance sites (not shown).

Histological Analysis

Histological Gram staining revealed an abundance of Gram-positive cocci on sections of excised control wounds as compared to wounds treated with AP183 spores and metabolites (*figure 3.3A-B*). However, Gram-positive cocci were also observed in treated wounds. H&E stained sections of excised tissue appear necrotic and inflamed in contrast to AP183 treated wounds (*figure 3.3C-D*).

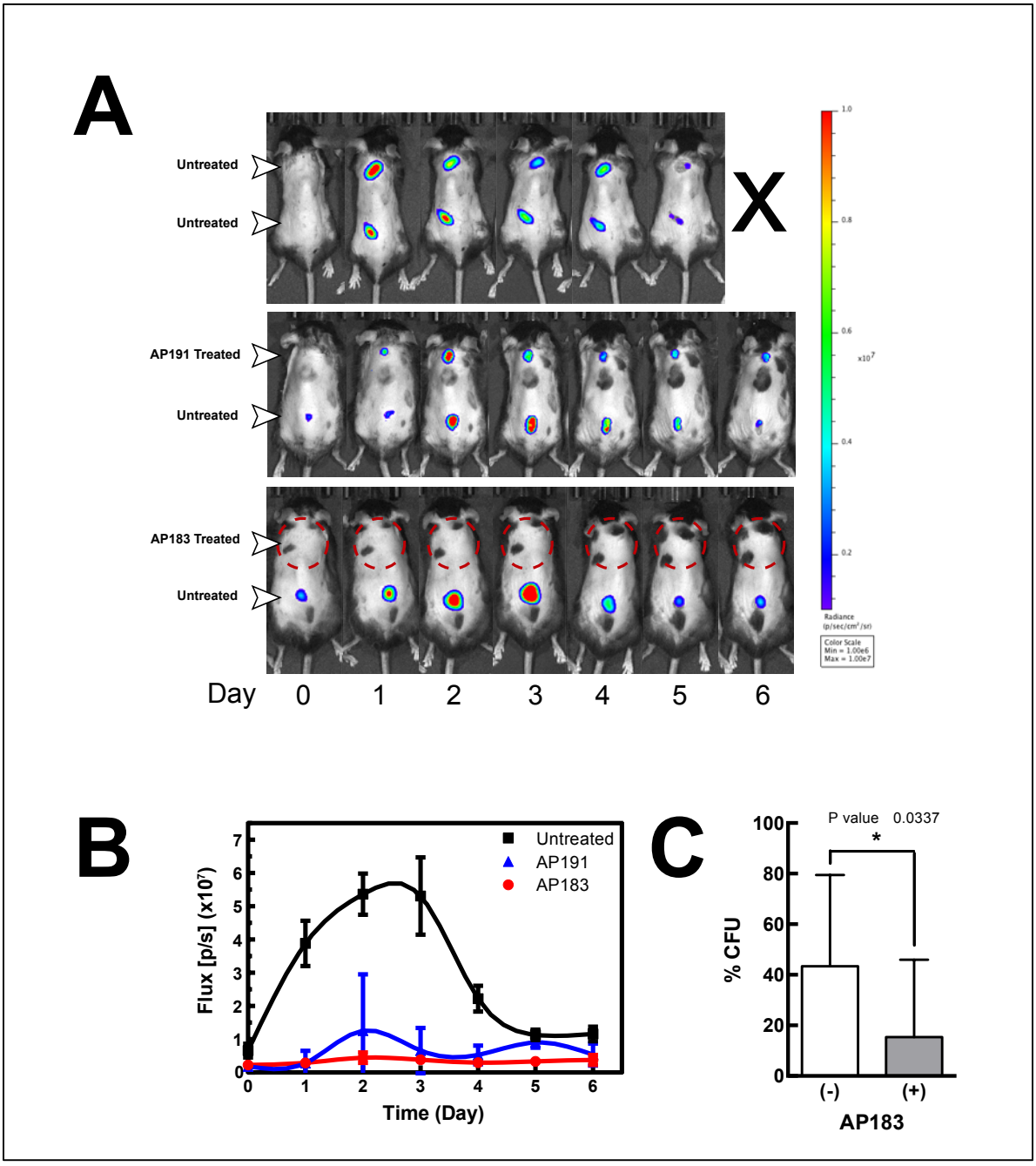

Figure 3.2. *In vivo* evaluation of *B. amyloliquefaciens* strains AP183 and AP191 inhibition of *S. aureus* Xen29 in a cutaneous wound model. Mice were given subcutaneous injections of $1x10^6$ CFU/mL of *S. aureus* Xen29 between the shoulder blades and on the lower back. (**A**) Upper panel, untreated mouse that succumbed to systemic infection 5 days after initial cutaneous wound challenge. Center panel, mouse treated with *B. amyloliquefaciens* AP191 on upper wound. Lower panel, mouse treated with AP183 on the upper wound and untreated in the lower wound. (**B**) Bioluminescent flux (photons/second) of *S. aureus* Xen29 in AP183/AP191 treated wounds and untreated controls over time. (**C**) Percent CFU determined for AP183 treated and untreated wounds from excised homogenates plated on TSA.

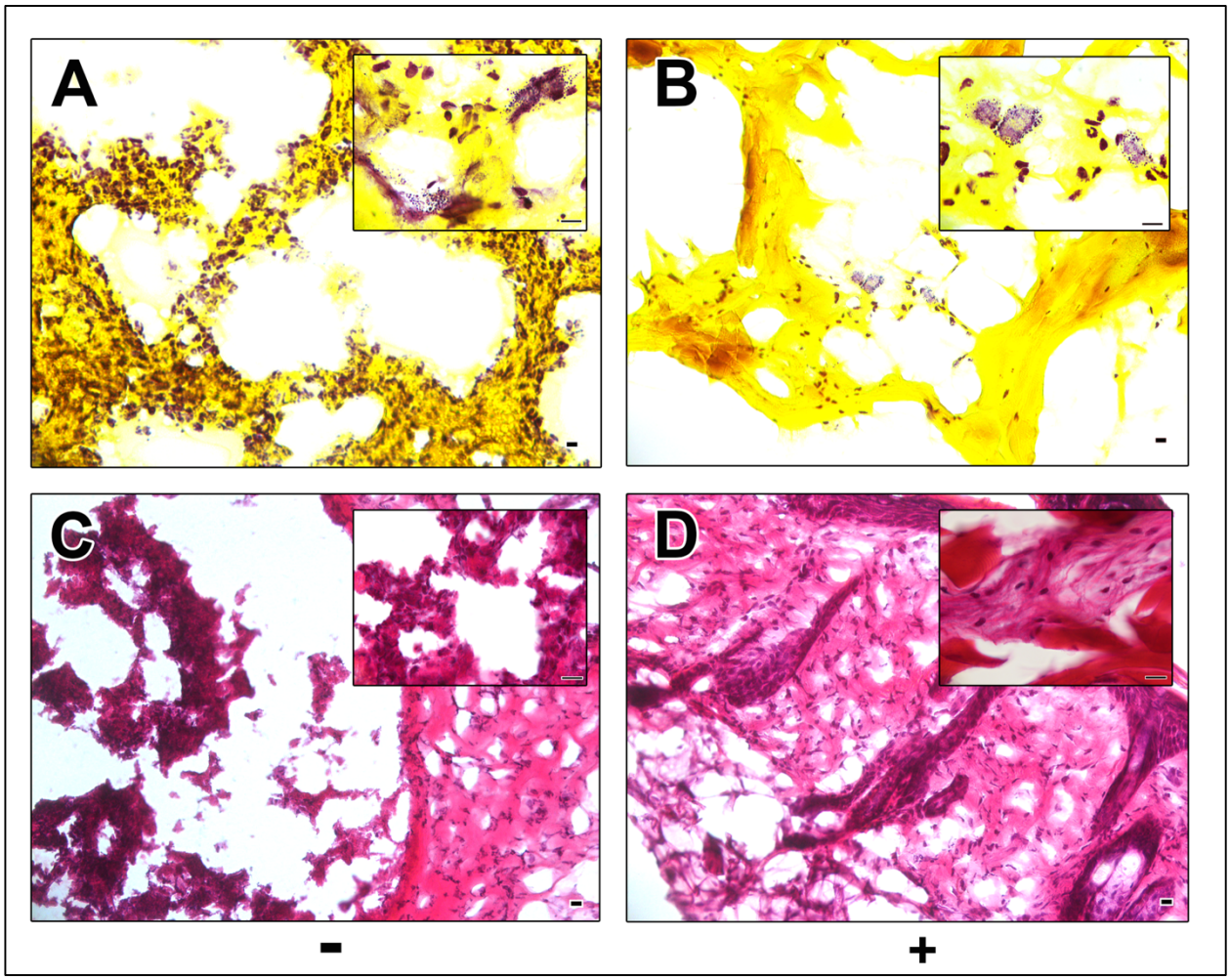

Figure 3.3. Histological analysis of control and AP183 treated wounds. Gram (**A**-**B**) and H&E (**C**-**D**) stained sections of excised wounds infected with *S. aureus* Xen29 in the presence **(+)** and absence **(-)** of AP183 co-administration. Clusters of Gram positive cocci were observed in higher frequency in untreated wounds than those treated with *B. amyloliquefaciens* AP183. Scale indicates 100 µM.

Microbial Diversity Analysis of the Mouse Skin

In addition to evaluating the inhibitory effect of AP183 on *S. aureus* proliferation in infected wounds *in vivo* by BLI and *ex vivo* culture-dependent and histological methods, we sought to analyze the relative abundance of microbiota present in wounds through culture-independent means. Therefore, we analyzed extracted 16S rRNA from wound homogenate samples and sequenced each to determine the percent relative abundance of microbial genera present in each homogenate sample. In *figure 3.4*, we present the top ten most abundant genera present in each sample, with the remaining pooled as a percentage labeled "other." Because this method cannot discern viable cells from dead based solely on DNA present in the samples, not surprisingly there is a large percentage of *Staphylococcal spp.* represented in all wounds which were infected with *S. aureus* Xen29. Whether or not those cells are viable cannot be determined. However, our results indicate that wounds treated with AP183 have approximately 25-35% less relative abundance of *Staphylococcal spp.* as compared to untreated controls. Interestingly, *Bacillus spp.* are the third most abundant genera in AP183 treated wounds (7.00%) behind *Enterobacter spp.* (9.04%) and *Staphylococcal spp.* (62.58%). Most abundantly present in naïve mouse skin samples were *Phyllobacterium spp.* (46.74%), another plant-root associated bacterium that we suspect may be present in high concentrations on mouse bedding or food pellets [96].

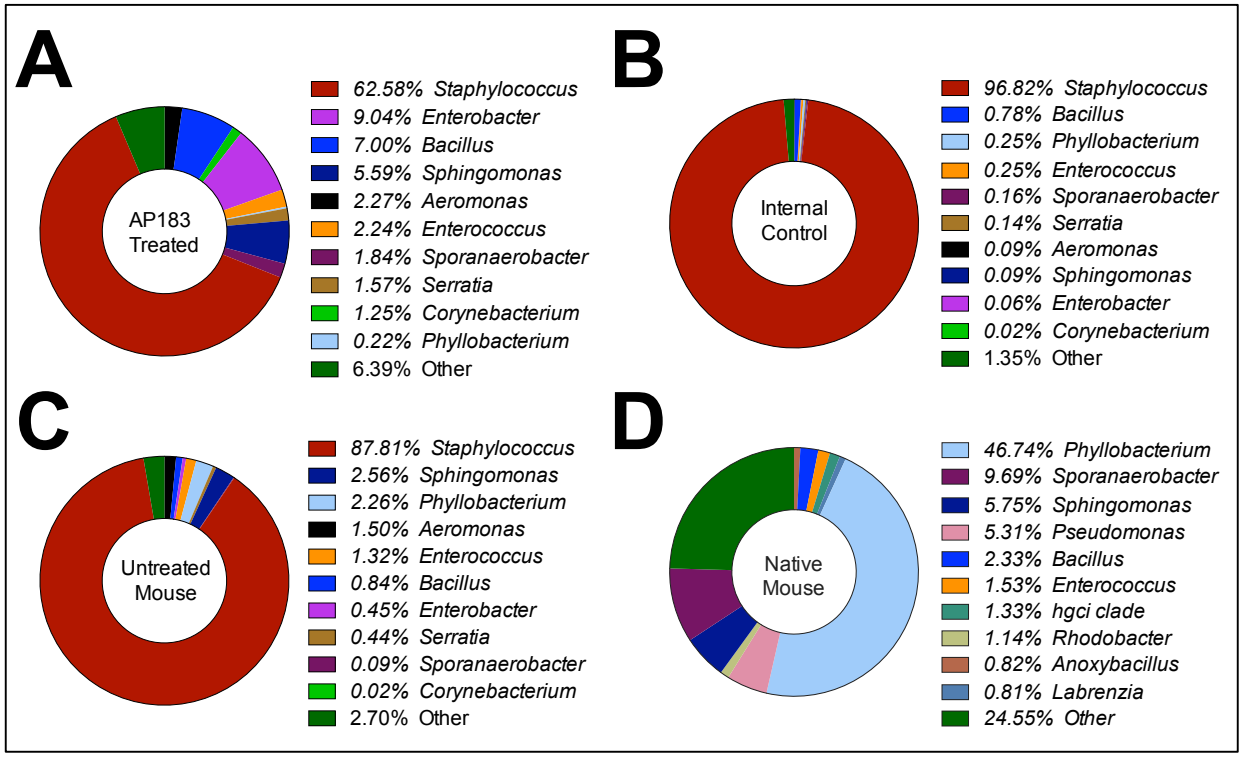

Figure 3.4. Percent relative abundance of microbial genera from 16S rRNA gene sequence ribotypes from homogenates of (**A**) AP183 treated wounds, (**B**) internal *S. aureus* Xen29 control wounds, (**C**) wounds from untreated control mice, (**D**) skin sample from a native (naïve) mouse. Wounds treated with *B. amyloliquefaciens* AP183 resulted in a 25-35% decrease in relative abundance of *Staphylococcal* genera.

Discussion

Skin and soft tissues are the most common sites of *S. aureus* infection, although *S. aureus* can cause life-threatening systemic infection, stemming from cutaneous infected sites. More than 75% of MRSA-related diseases are skin-involved infection and prophylactic measures to deter *S. aureus* colonization on the skin could ultimately reduce the incidence of systemic infection [97]. The primary objective of this study was to evaluate the efficacy of probiotic candidate organisms for inhibiting cutaneous *S. aureus* colonization and maintain/restore beneficial skin microbiota. The key considerations used for evaluating candidate probiotic organisms were safety, efficacy, and commercial potential (i.e. shelf-life). For these reasons, our efforts have focused on identifying endospore-forming members of the genus *Bacillus* that have efficacy in preventing *S. aureus* infections, without any known potential for pathogenicity. With consideration to commercial potential, spore-forming strains were preferred because of their potential for long-term stable storage without the loss of function. These criteria narrowed our search to a select few strains from our library and ultimately led to the discovery of *B. amyloliquefaciens* AP183, due to its non-pathogenic nature and potent production of bioactive compounds inhibiting MRSA and VRE as previously determined *in vitro* [94]. The annotation of the genome sequence of the AP183 strain revealed the absence of predicted virulence factor encoding genes in this genome which supports the safety of this strain for topical application. However, further assessments of AP183 should be conducted for safety, including studies to assess any potential for cytotoxicity of AP183 secondary metabolites (e.g., bacillusin A).

Preliminary screening of 177 *Bacillus* strains was performed to assess their respective degrees of *S. aureus* inhibition *in vitro*, as well as early *in vivo* studies with a mouse wound model (see Nasrin, 2015 for a more detailed description of these results) [93]. These preliminary studies

revealed that *B. amyloliquefaciens* strain AP183 was the most effective strain for inhibiting *S. aureus* growth and would be the most promising candidate for future investigation. We believe the antibacterial activity of AP183 is due primarily to the production of secondary metabolites, in particular a novel antibiotic compound, bacillusin A, which was shown to exhibit strong *in vitro* bactericidal activity against MRSA and VRE in previously published studies [94]. While bacillusin A was found to be a potent inhibitor of several relevant pathogens, it was determined to be chemically unstable in organic solvents and prone to photoisomerization as indicated by LC-MS analysis [94]. The photoisomerization and chemical instability in organic solvents ultimately resulted in a low isolation yield of the compound, thereby making it unlikely that purified bacillusin A would be a viable candidate for use as an oral or injectable antibiotic in the clinical setting. However, the biochemical instability of this compound might be advantageous for topical treatment of infected wounds where rapid elimination of antibiotic residues may be preferred. For instance, prophylactic topical application on dressings for severe burn wounds, wherein exposed tissues are readily infected by *S. aureus* and other pathogens, often resulting in patient mortality [98].

In *figure 3.4,* we evaluated the relative abundance of microbial genera in naïve mouse skin, wounds infected with *S. aureus* Xen29, and infected wounds treated with co-administration of *B. amyloliquefaciens* AP183 with results indicating that treatment with AP183 and supernatant significantly reduced the relative abundance of *S. aureus* ($p = 0.0198$) between treated and control wounds, while also appearing to increase the relative abundance of other skin-associated bacterial genera. It is worth noting that this method is entirely DNA-dependent and as such does not discriminate between metabolically active or inactive cells. Therefore, the required PCR step will

inherently bias the results in favor of the most prevalent DNA present in the sample, whether or not the cell was metabolically active at the point of extraction.

Bioluminescent signal intensity was consistently observed to decrease in control wounds beginning around day 4 of infection. However, both culture-dependent and culture-independent methods confirmed a high prevalence of *S. aureus* in wound homogenates. This decrease in bioluminescent signal may be due to many factors, but histological analysis suggests that dissemination to distance sites from systemic infection may have resulted in some cases. Gram stained sections of a heart of one control mouse (not shown) that succumbed to systemic infection revealed clusters of Gram positive cocci in the aortic region of the heart. This was an unexpected result, but supports the ability of *S. aureus* to disseminate from a cutaneous wound and establish life-threatening systemic infections at distance sites.

One key limitation of AP183 observed from this study is that *Bacillus* spores alone may not be sufficient to inhibit the establishment of *S. aureus*, but its efficacy is improved in the presence of AP183 metabolites present in the supernatant of germinated cells. *S. aureus*, like many other pathogens, are fast-growing (i.e., r-selected) bacteria that can outcompete other slow-growing microbes for carbon sources. For this reason, we selected fast-growing *Bacillus* spp. that can better compete for the limited carbon substrates in cutaneous environment. However, the inhibition of *S. aureus* proliferation in the wound by *B. amyloliquefaciens* AP183 spores was enhanced by co-administration of supernatant containing secondary metabolites, indicating that these metabolites may aid in germination of AP183 spores in the early stages following administration.

The results of this study indicate that *B. amyloliquefaciens* AP183 and its metabolites may serve as potent biocontrol agents with potential broad application in agriculture and medicine. In

the short term, AP183 in probiotic formulation may benefit agricultural applications such as treatment and prevention of chronic bovine mastitis and cutaneous colonization of livestock swine. If successful, applications in these areas alone may have a substantial impact on the economic burden of *Staphylococcal* incidence in agriculture, and by extension, may ultimately reduce the carriage-rate of livestock-associated *S. aureus* strains that have been isolated from human infection (such as ST398) in livestock workers as well. Given the alarming rise of antibiotic resistant pathogens and current climate of stifled antibiotic development, biocontrol strategies with probiotic organisms such as AP183 may soon find relevance in human medicine as well.

Contributions

Andrew Brannen and Shamima Nasrin contributed equally to this project and performed all *in vivo* procedures and imaging. Shamima Nasrin contributed to preliminary *in vitro* studies leading up to this research and performed all CFU plating and analysis metagenomic. Andrew Brannen performed all analysis of *in vivo* imaging data and performed statistical calculations. Andrew Brannen excised tissue samples and embedded tissues for histological staining. Molly Wright performed sectioning and staining of histological slides. Andrew Brannen analyzed and acquired images of stained histological slides. This research was performed under the guidance and supervision of Mark Liles, Ph.D. (Associate Professor, Auburn University Department of Biological Sciences) and Peter Panizzi (Associate Professor, Auburn University Department of Drug Discovery and Development).

4. Species-Specific Prothrombin Activation by Staphylocoagulase from *Staphylococcus aureus* RF122 of Bovine Origin

Introduction

Staphylococcus aureus (*S. aureus*) is a ubiquitous opportunistic pathogen with a variety of clinical manifestations in multiple host-species including human, bovine, ovine, porcine, and poultry [11, 99-102]. *S. aureus* infection can progress into severe life-threatening diseases such as bacteremia, osteomyelitis, endocarditis, and pulmonary infections [9, 22, 68, 101, 103-109]. Much of *S. aureus* virulence stems from its ability to clot blood and clump (agglutinate) in host circulation [110, 111]. Procoagulant virulence factors expressed by *S. aureus,* namely staphylocoagulase (SC) and von Willebrand factor binding protein (vWbp), activate host prothrombin (ProT), catalyzing the conversion of soluble fibrinogen (Fbg) into insoluble fibrin [112, 113]. ProT activation by SC and vWbp circumvents the physiological mechanisms involved in coagulation and results in localized clot formation, which mediates *S. aureus* attachment within the host and provides a physical barrier to prevent opsonization of the pathogen by phagocytic cells [8, 109].

To maintain hemostasis, physiological activation of ProT into α-thrombin is a highly regulated process mediated by a series of proteolytic pathways (either intrinsic or extrinsic) converging on the activation of factor X (factor Xa) [114]. Factor Xa, in complex with factor Va on a phospholipid (PL) surface, initiates proteolytic cleavage at Arg^{271} and Arg^{320} and results in the formation of α-thrombin [115]. Active site formation specifically, however, has been shown to be mediated through a mechanism wherein proteolytic cleavage occurs at Arg^{15}-Ile^{16} followed by insertion of the Ile^{16} peptide into an activation cleft (termed "Ile^{16} cleft") and formation of a salt

bridge with Asp^{194} [116]. This mechanism results in a stabilization of the active site on α-thrombin, readying it for catalysis of Fbg.

S. aureus coagulases mimic this process and hijack the host system. Activation of ProT by SC occurs non-proteolytically through insertion of its NH_2-terminal peptide SC into the Ile^{16} activation cleft of ProT, forming a salt bridge with Asp^{194} and ultimately resulting in a similar conformational change and formation of the active site [8, 112, 117]. The NH_2-terminus of SC is highly conserved (Ile^1-Val^2-Thr^3-Lys^4-Asp^5-Tyr^6-Ser^7) and mimics the endogenous peptide that is inserted into the Ile^{16} activation cleft. It has been determined through kinetic study of SC^{1-325} mutants that Ile^1-Val^2 are critically important for SC activation of ProT, with SC^{3-325} resulting in a 98% decrease in activity [8].

Biochemically, SC and vWbp bind circulating ProT within a given host, forming an equal molar complex of zymogen to activator [118, 119]. Activation of ProT is considered the second step, whereby the complex is initially formed and then the N-terminal region on the activator inserts into the zymogen activation pocket to stabilize the active conformation ProT•SC* or ProT•vWbp*, respectively. Coincidentally, there is formation of a new Fbg substrate-binding site on the zymogen•activator complex as a result of blockage of the canonical Fbg-binding site (i.e. exosite I) by domain 2 of the bacterial activator [8, 113, 120]. Once formed, the zymogen•activator complex is primed to catalyze the conversion of Fbg to fibrin. SC and vWbp are members of a family of virulence factors called zymogen activator and adhesion proteins (ZAAPs) [8, 112]. The COOH-terminal regions are fundamentally different among these ZAAPs and lack any significant homology. This diversity is thought to anchor these proteolytic complexes to host adhesions proteins such as Fbg, fibronectin, and potentially von Willebrand factor [40, 121-123].

The recent advent of next-generation DNA sequencing technology has significantly advanced our understanding of the complexities of pathogen adaptations to particular host organisms. Whole-genome sequencing of *S. aureus* isolates has been particularly useful for tracing the lineage of such pathogens and their acquisition of mobile genetic elements (MGEs) [70]. Sequencing of *S. aureus* genomes from different host origins have also allowed for extensive study of proteomic homology among these strains. Despite sharing up to 37% proteomic identity among certain strains, both SC and vWbp are expressed differentially from separate pathogenicity islands (genomic regions) by all *S. aureus* genomes sequenced to date [124]. Next-generation sequencing has not only allowed for direct comparisons of proteomic homology among *S. aureus* isolates, but also the overall arrangement of genes in a whole genome. These factors may be instrumental in furthering our understanding of the evolutionary adaptations of *Staphylococcal* ZAAPs to particular host zymogens among genomes that have been sequenced.

Animal studies have produced conflicting results as to whether or not SC is a virulence factor for *S. aureus* diseases, with some studies reporting that SC is not involved in the initial attachment stages of endocarditis, and others demonstrating reduced virulence of SC-deficient mutants in mouse models of mastitis, pulmonary infections, and endocarditis [103, 104, 109, 124-128]. Certain *S. aureus* strains can activate the clotting system of certain animal hosts more efficiently than other host species [129, 130]. This unique *Staphylococcal* ability is potentially a result of intrinsic differences in the structure of ProT or Fbg molecules among different species. For instance, some studies have shown that murine thrombin lacks the Na+ binding site in the activation cleft of human thrombin, yet retains high catalytic activity [131]. The lack of this Na+ binding site would result in an inability of microbial ZAAPs to target and bind this site. However, a microbe with an adaptation in a particular virulence factor to account for the lack of this Na+

binding site would have a competitive advantage over pathogens without this adaptation. It has been shown that this Na+ binding site is present on the $SC^{Tager104}$(1-325)•Bovine ProT complex [132].

For the purposes of this study, we define the species-specificity as a function of microbial virulence factor adaptations for specific host species, which confers a competitive advantage over other pathogenic strains. It is *our opinion* that these molecular adaptations for pathogen-host interactions may explain the species-specific ProT activation that has been observed among strains of *S. aureus* and respective host species. Here, we investigate the species-specific clotting efficiencies of *S. aureus* isolates from multiple host species through proteomic analysis, kinetic assays of ProT activation by SC, and whole-plasma clotting assays of SC. Our results indicate that the species-specific clotting efficiency is not the result of differing affinities of SCs for particular host ProT, but rather differences in Fbg recognition by the activator•zymogen complex.

Materials and Methods

Reagents, Proteins, Bacterial Strains, and Plasma

Human and bovine ProT and thrombin were purchased from Haemtech Inc. (Haemtech Technologies Inc. Essex Junction, VT). Purity was verified by SDS-gel electrophoresis and molar concentrations were determined by use of a spectrophotometer and the following molar absorption coefficients ($(mg/ml)^{-1}cm^{-1}$) and molecular weights [133, 134]: ProT, 1.47, 71,600; Fbg, 1.54, 340,000; SC^{RF122}-(1-320), 1.33, 37,742 (theoretical); and $SC^{Tager104}$-(1-325), 1.00, 38,000). Extinction coefficients were calculated from the aromatic amino acid composition of the respective proteins [135]. Oregon Green-FPR-prothrombin ([OG]FPR-ProT) was provided by Dr. Paul Bock and was prepared, as has been previously published, wherein 5- (and 6)-iodoacetamido-2',7'-

difluorofluorescein (OG) iodoacetamide was coupled to a thiol group containing inhibitor bound to human ProT [120]. *S. aureus* Newman mutants were previously published and obtained from Olaf Schneewind, University of Chicago, Chicago, IL. Mutations were made through allelic exchange resulting in selective knockout of *coa*, *vwb*, or both *coa* and *vwb* genes in these strains [136]. Human, bovine, and rabbit plasma was purchased from Innovative Research, Novi, MI.

Proteomic Analysis of S. aureus Strains

All sequences were downloaded from GenBank® through the National Center for Biotechnology Information (https://www.ncbi.nlm.nih.gov/genbank). Strains were selected for blast matrix proteomic analysis based on the availability of whole-genome sequence, clinical relevance, and host diversity. CMG-Biotools virtual machine (graciously provided by Dr. David Ussery, Technical University of Denmark, Kgs. Lyngby, Denmark) was used to download genomic sequences from GenBank® with the "*getgbk*" function and converted to FASTA formatted files using "*saco_convert*" function [137]. FASTA files were then submitted to "*prodigalrunner*" algorithm to process open reading frames and create FASTA files of predicted proteins. The blast matrix was then created using the "*makebmdest*" and "*blastmatrix*" algorithms in CMG-Biotools and exported as a post-script file. Statistical significance was determined using unpaired student's t-test with Welch's correction in Prism 6 (GraphPad Software Inc.). Results are shown in *figure 4.1*, with strains listed in *table 4.1*.

NH_2-terminal protein sequence of the crystallized SC (from *S. aureus* Tager 104 (human origin, SwissProt entry Q846V4, [8, 70]), Newman (human origin; [9], and RF122 (bovine origin) were compared using CLUSTALW [11]. Strictly conserved residues and conservative substitutions are denoted by red and gray highlights, respectively. Residues of respective SCs that

contact the activation cleft are indicated by closed triangles and exosite I by open triangles, shown in *figure 4.2* [8].

Recombinant NH_2-terminal Staphylocoagulase Domains 1 and 2 from Tager 104 ($SC^{Tager104}$-(1-325)) and RF122 (SC^{RF122}-(1-320)) and Their Fusion Protein Precursors

$SC^{Tager104}$-(1-325) and tobacco etch virus protease (TEVp) were expressed, purified, and characterized as described previously [120]. Briefly, SC^{RF122}-(1-320) was produced as a NH_2-terminal His_6-tagged fusion protein His_6-tag (*bold*) with a TEVp cleavage site (*underlined*) encoded before the SC^{RF122}-(1-320) protein, specifically encoded was Met-**His_6**-Ser-Ser-Gly-Leu-Val-Pro-Trp-Asn-Glu-Asn-Leu-Tyr-Phe-Gln-$^{SC}Ile^{1}$... $^{SC}Gln^{320}$ denoted as His_6-[TEV site]-SC^{RF122}-(1-320), which was expressed in *Escherichia coli* strain Rossetta2(DE3)pLysS for purification using the nickel (Ni^{2+}) affinity of the His_6-tag. From an overnight culture, cells were diluted in fresh Luria broth (100-fold) and were grown to an optical density of 0.4-0.6 at 600 nm prior to induction by addition of 500 μM isopropyl-beta-*D*-thiogalactopyranoside. Cells were incubated following induction for 4 hours and lysed by sonication on ice in a metal beaker with constant monitoring of temperature ensuring temperatures never exceeded 15 ºC. His_6-[TEV site]-SC^{RF122}-(1-320) was purified from the insoluble fraction obtained after centrifugation to clarify the cell lysate. His_6-[TEV site]-SC^{RF122}-(1-320) was recovered from the insoluble fraction by use of the mild chaotropic salt sodium thiol cyanate (NaSCN) and refolding by dilution (4-fold) into Ni^{2+}-iminodiacetic acid-Sepharose chromatography equilibration buffer. Generation of the critical NH_2-terminal Ile^{1} of SC^{RF122}-(1-320) was accomplished by overnight dialysis with TEVp containing an intrinsic COOH-terminal His_6-tag [138].

Bovine and Rabbit Plasma Clotting Assays

S. aureus Newman wild-type (+/+) and mutants with allelic replacement deletions for vWbp (+/-), SC (-/+), and (-/-) were inoculated into 50 mL brain heart infusion broth (BHI; RPI, Mount Prospect, IL) and incubated overnight shaking at 225 rpm at 37°C. Cells were pelleted by centrifugation at 2200 x g for 15 minutes at 4°C and supernatant was collected for each Newman strain. 10 µL of overnight cultures from each Newman strain was pipetted into glass tubes containing 300 µL of either bovine plasma or rabbit plasma. Contents of each tube were mixed by pipetting, and incubated upright at 37°C for 12 hours. Following incubation, tubes were laid on their side and assessed for the distance traveled by the plasma (*figure 4.3A-B*).

Growth Curve and Kinetic Analysis of S. aureus Secretome

S. aureus Newman wild-type (WT) and deletion mutants for vWbp (ΔvWbp), SC (ΔSC), vWbp and SC (ΔSCΔvWbp) were each cultured overnight in 50 mL of BHI broth (RPI, Mount Prospect, IL), shaking at 225 rpm at 37°C. Four Fernbach flasks with 1L of BHI broth were inoculated with 10 mL of overnight culture for each respective Newman mutant. Each Fernbach was incubated in a shaker at 225 rpm, 37°C. Samples of 1.0 mL were taken from each flask every 20 minutes, OD_{600} nm was assessed using a Shimadzu UV-2101PC spectrophotometer (Shimadzu Corp. Kyoto, Japan) and PEG 20,000-coated 1.5 mL polystyrene cuvettes (Sarstedt, Nümbrecht, Germany). Samples were then immediately centrifuged at 2200 x g for 5 minutes, followed by transfer of supernatant to cryotubes (Corning, Corning, NY), and flash-frozen in liquid nitrogen. Each supernatant sample was later thawed and assessed for ProT activation activity using the chromogenic Fbg analogue H-*D*-Phe-Pip-Arg-*p*NA for substrate turnover assessment. For each supernatant sample, 50 µL of supernatant was incubated with 2.4 nM human ProT in 194 µL of

assay buffer (50 mM HEPES, 125 mM NaCl, 5 mM $CaCl_2$, 1.0 mg/mL bovine serum albumin (EMD Chemical Inc., Darmstadt, Germany) pH 7.4) for 10 minutes at room temperature in a 1.5 mL polyethylene glycol (PEG) 20,000-coated polystyrene cuvette. Following incubation, an excess of H-*D*-Phe-Pip-Arg-*p*NA at a final concentration of 67.1 μM was added, quickly mixed by pipetting, and immediately placed in a Thermo Evolution 300 spectrophotometer (Thermo Fisher Scientific, Waltham, MA) and analyzed for a change in absorbance at 405 nm, indicated by release of the *p*NA group on the substrate complex H-*D*-Phe-Pip-Arg-*p*NA. The rate at mAbs/min was recorded for each supernatant sample and plotted against the respective time point of sample acquisition (*figure 4.3C*).

Kinetic Progress Curves of Chromogenic Substrate

Kinetic parameters for hydrolysis of chromogenic substrates by α-thrombin and SC^{RF122}-(1-320)•(pro)thrombin were determined using a Thermo Evolution 300 spectrophotometer. Absorbance increases were monitored at 405 nm in 50 mM HEPES, 110 mM NaCl, 5 mM $CaCl_2$, 1 mg/ml bovine serum albumin, and 0.1 mg/ml soybean trypsin inhibitor at 25 ºC, using PEG 20,000-coated cuvettes. Kinetic parameters k_{cat}, $K_{m,}$ and when applicable, K_i, for H-*D*-Phe-Pip-Arg-*p*NA were determined for substrates with low K_m by simultaneous fits of the integrated Michaelis-Menten equation to the full reaction progress curves for the conversion of substrate at the following concentration ranges: 1, 5, 10, 20, and 50 μM. Mouse or bovine ProT concentrations ranged from 2, 1.5, 1, 0.75, 0.5, and 0.25 nM for each substrate with 10 nM SC^{RF122}. For bovine ProT activation by either $SC^{Tager104}$-(1-325) or SC^{RF122}-(1-320) with H-*D*-Phe-Pip-Arg-*p*NA, kinetic parameters were determined by fitting the Michaelis-Menten equation to initial rates acquired over substrate concentrations. In all assays, SC^{RF122}-(1-320) and (pro)thrombin were pre-

incubated for approximately 20 min, with reactions initiated by the addition of substrate, as previously described [120]. Results are shown in *figure 4.4 and 4.5*, with determined kinetic constants listed in *table 4.2.*

OG-FPR-ProT Kinetic Binding to SC^{RF122} and Native Bovine ProT Through Competitive Binding Assay

The fluorometer used for this study was a PTI QuantaMaster 80 (Horiba Ltd., Kyoto, Japan) with acrylic cuvettes coated with PEG 20,000. For titrations of probe concentration, serial additions of [OG]FPR-ProT were made to cuvettes and measurements were corrected for background and probe dilutions. Changes in fluorescence were measured as a function of total SC^{RF122}-(1-320) concentration, expressed as $(F_{obs}-F_o)/F_o=/F-F_o)$, and were fit using the quadratic binding equation to determine the maximum fluorescence change $((F_{max}-F_o)/F_o=\Delta/_{max}/F_o)$, dissociation constant (K_D), and stoichiometric factor (n). Nonlinear least squares fitting was performed with SCIENTIST software (MicroMath, Saint Louis, MO). Titrations of [OG]FPR-ProT were performed at 0.5, 2, and 20 nM with SC^{RF122} to determine kinetic parameters. Competitive binding assays were performed with titrations of native bovine ProT from 0-1.6 μM in saturating conditions of [OG]FPR-ProT at 2 and 200 nM concentrations of SC^{RF122}. Results are shown in *figures 4.7* and *4.4,* with determined kinetic constants listed in *table 4.2*.

Fibrometer Clotting Assays of Whole Bovine and Human Plasma

Whole plasma clotting assays were performed at 37 °C with a BBL Fibrosystem fibrometer. Relative clotting activity was evaluated by comparison using an α-thrombin standard from the slopes of clotting time versus the reciprocal of the enzyme concentration, as previously

described [120, 139]. For each assay, 200 μL of either bovine or human plasma was mixed with respective preformed SC•ProT complex at varying concentrations and Q.S. to a total volume of 300 μL with reaction buffer (20 mM HEPES, 150 mM NaCl, 10 mM CaCl, 10 mg/mL PEG8000, pH 7.4). The timer was started immediately following addition of respective preformed SC•ProT complex and automatically stopped when a clot was detected. Results are shown in *figure 4.9A-B*.

Bovine ProT Purification from Whole Plasma using SC^{RF122}-(1-320-His_6) Bound to Nickel Column

Approximately 15 mg of SC^{RF122}-(1-320) was purified as previously described, leaving the His_6 tag intact, and loaded onto a HisTrap™ FF 5 mL nickel affinity column. 25 mL of bovine plasma was prepared with 100 μM PMSF by dialysis in 100 mL of equilibration buffer (50 mM HEPES, 400 mM NaCl, 40 mM imidazole, 1 mg/mL PEG 8000, pH 7.4) with constant stirring at 4°C with 3 changes. Following dialysis, sample was run through the SC^{RF122}-(1-320-His_6) loaded column using an ÄKTA™ Pure fast protein liquid chromatography (FPLC; GE Life Sciences) system and eluted on a block gradient using elution buffer (50 mM HEPES, 125 mM NaCl, 1 M imidazole, 1 mg/mL PEG 8000, pH 7.4). Fractions were collected and samples were analyzed by SDS-PAGE.

Results

Proteomic Homology of S. aureus Isolates

Blast matrix results of selected human and ruminant isolates of *S. aureus* are shown in *figure 4.1*. Human *S. aureus* isolates (n = 6) averaged 80.83% homology among predicted proteins with a standard deviation of 5.57% while ruminant isolates (n = 4) averaged 81.90% homology and a lower standard deviation of 1.48%. Comparisons of homology among human and ruminant

isolates independently (human x human; ruminant x ruminant) did not yield a degree of significant difference. However, analysis of strains grouped by host isolate resulted in a significant difference ($p = 0.0170$) in the average of protein homology among all ruminant isolates tested and the average homology of all bovine and human isolates combined. (*figure 4.1 – inset*). The list of strains used for this analysis are detailed in *table 4.1*.

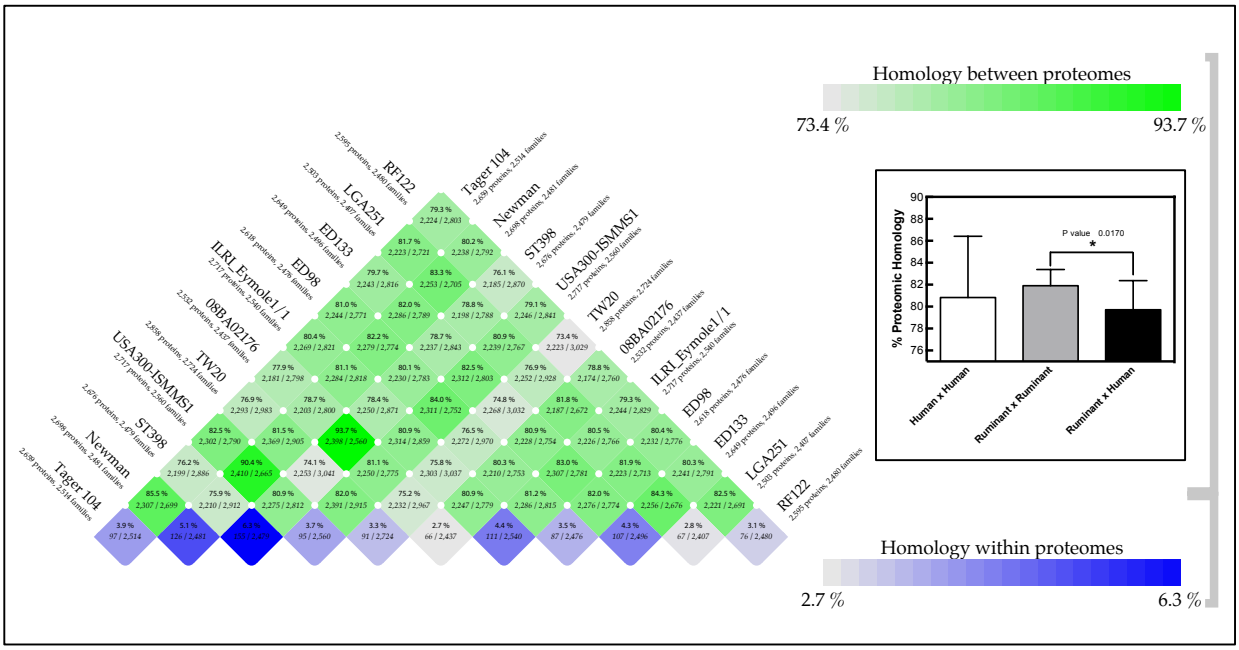

Figure 4.1. Proteomic homology of *S. aureus* strains of ruminant (RF122, LGA251, ED133), poultry (ED98), camel (ILRI_Eymole1/1), and human (08BA02176, TW20, USA300-ISMMS1, ST398, Newman, Tager 104) origins. Strains were selected based on availability of whole-genome sequence, clinical relevance, and host diversity. Strains 08BA02176 and ST398 are LA-MRSA human isolates, representing strains known to infect multiple host species. **Inset**: Comparison of proteomic homology between strains grouped by host species. Statistical analysis was performed by student t test with $\alpha = 0.05$. Analysis of strains grouped by host isolate resulted in a significant difference ($p = 0.0170$) in the average of protein homology among all ruminant isolates tested and the average homology of all bovine and human isolates combined.

Isolate	Host	Infection	ST	Notes	Accession	Refs
08BA02176	Human	Wound	398	LA-MRSA	NC_007622	[140]
ED133	Ovine	Mastitis	133	Ruminant (sheep)	NC_017337	[100]
ED98	Poultry	Skeletal infection	5	Poultry (chicken)	NC_013450	[102]
ILRI_Eymole1/1	Camel	Nasal swab	30	Human clonal complex isolate	NZ_LN626917	[141]
LGA251	Bovine	Mastitis	425	*mecA*-negative MRSA	NC_017349	[142]
Newman	Human	Osteomyelitis	254	Well-characterized isolate	NC_009641	[9]
RF122	Bovine	Mastitis	151	Common bovine mastitis isolate	NC_007622	[11, 143]
ST398	Human	Endocarditis	398	LA-MRSA	NC_017333	[101]
Tager 104	Human	Impetigo	49	Early-branching hospital-acquired strain	NZ_CP012409	[70, 144]
TW20	Human	Bacteremia	239	Multi-resistant	NC_017331	[105]
USA300-ISMMS1	Human	Bacteremia	8	MRSA	NZ_CP007176	[106]

Table 4.1. *S. aureus* strains used for blast matrix proteomic analysis.

Proteomic Alignment of $SC^{Tager104}$, SC^{Newman}, and SC^{RF122}

Alignments of N-terminal sequences of crystalized $SC^{Tager104}$, SC^{Newman}, and SC^{RF122} are shown in *Figure 4.2*. The first 7 residues (Ile^1-Val^2-Thr^3-Lys^4-Asp^5-Tyr^6-Ser^7) of $SC^{Tager104}$, SC^{Newman}, and SC^{RF122} are strictly conserved. Strict conservation or conservative substitutions of residues that interact with the 148-loop and exosite I were largely consistent among all three SCs evaluated. This result indicates that there are few major substitutions which may contribute to the species-specificity of *S. aureus* isolates of human or bovine origin.

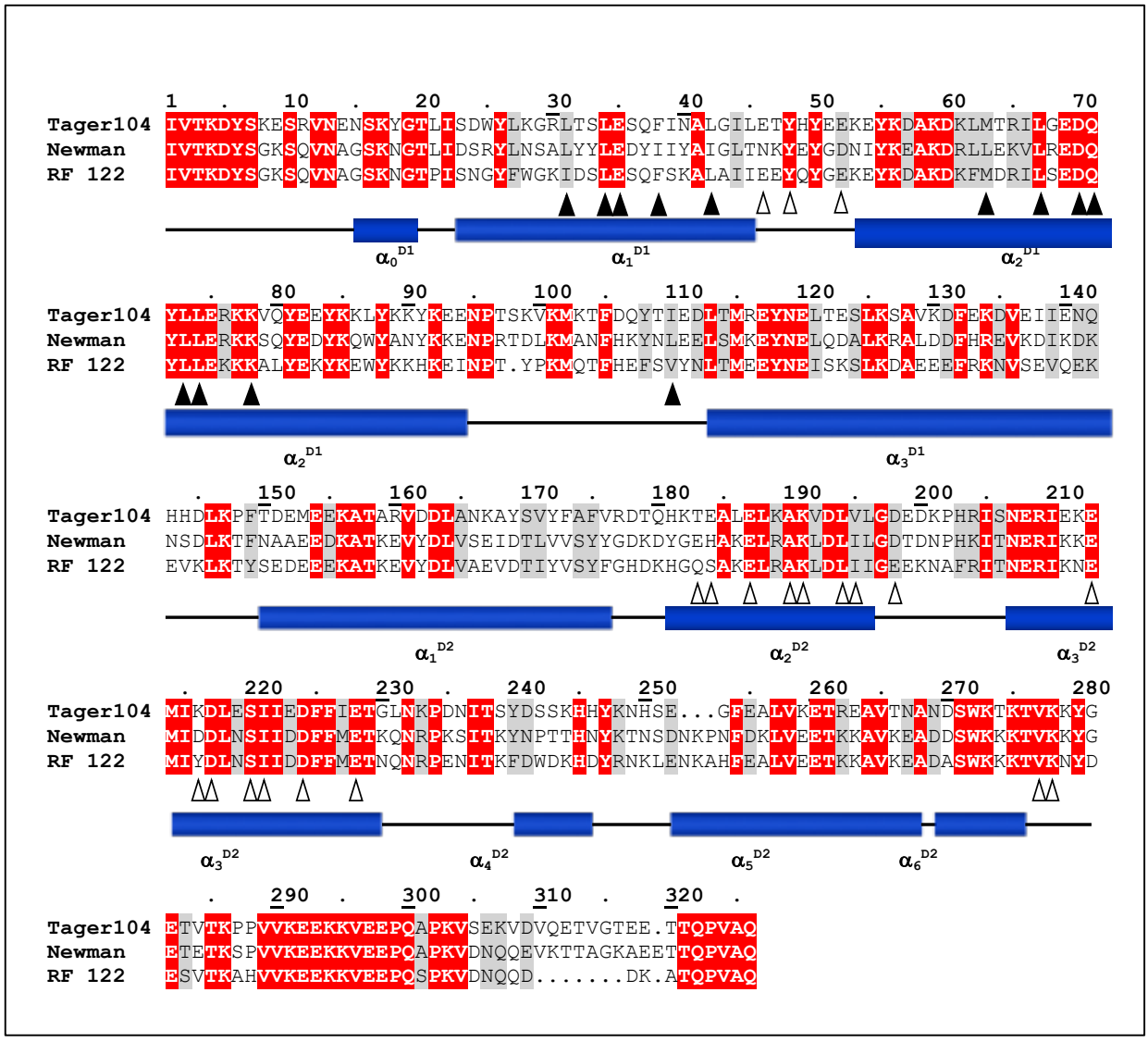

Figure 4.2. CLUSTALW proteomic alignment of $SC^{Tager104}$, SC^{Newman}, and SC^{RF122}. N-terminal protein sequence of the crystallized SC (from *S. aureus* Tager 104 (SwissProt entry Q846V4, [8]), Newman (human origin; [9], and RF122 (bovine origin; [11]). Strictly conserved residues (red highlight) and conservative substitutions (gray highlight). SC residues that contact the 148-loop (▲) or exosite I (△) are indicated.

Assessment of Procoagulant Function of S. aureus ProT Activators

To assess the relative contributions of SC and vWbp to the overall procoagulant activity of *S. aureus* strains, supernatants from overnight cultures of *S. aureus* Newman wild-type (WT) and deletion mutants for SC (ΔSC), vWbp (ΔvWbp), and ΔSCΔvWbp were added to tubes containing bovine and rabbit whole plasma. Tubes were incubated for 12 hours upright then laid horizontal to assess degree of coagulation based on distance traveled by plasma contents (*figure 4.3A-B*). We observed that the distance traveled by both human and rabbit plasma incubated with ΔvWbp mutant supernatant was comparable to WT, although the clot formed by ΔvWbp supernatants appeared more rigid than WT. However, plasma coagulation by ΔSC supernatants was comparable to ΔSCΔvWbp supernatants.

Further assessment of human ProT activation by each mutant was performed by analyzing turnover of chromogenic Fbg-analogue substrate H-*D*-Phe-Pip-Arg-*p*NA hydrolysis measured by spectrophotometer by supernatant samples of each mutant in culture taken at 20 minute intervals spanning a 12-hour growth curve (*figure 4.3C*). Interestingly, ΔvWbp mutant supernatants had the highest overall procoagulant activity, outperforming WT supernatants. ΔSC mutants showed considerably lower activity than ΔvWbp and WT, only slightly higher than ΔSCΔvWbp mutant supernatants.

To determine whether the observed effect was a result of differences in secretory or membrane-bound expression of SC and vWbp, whole cell lysates of Newman WT, ΔvWbp, and ΔSC were assessed for procoagulant activity of human ProT by hydrolysis of chromogenic Fbg-analogue substrate (*figure 4.3D*). ΔvWbp mutant lysates had a slightly lower rate of substrate hydrolysis than WT, while ΔSC lysates showed considerably lower rates of hydrolysis than WT and ΔvWbp lysates. Collectively, these results indicate that SC is the major contributor to the

procoagulant activity of *S. aureus* and that redundant expression of both ProT activators, SC and vWbp, may actually reduce the overall procoagulant activity of *S. aureus.*

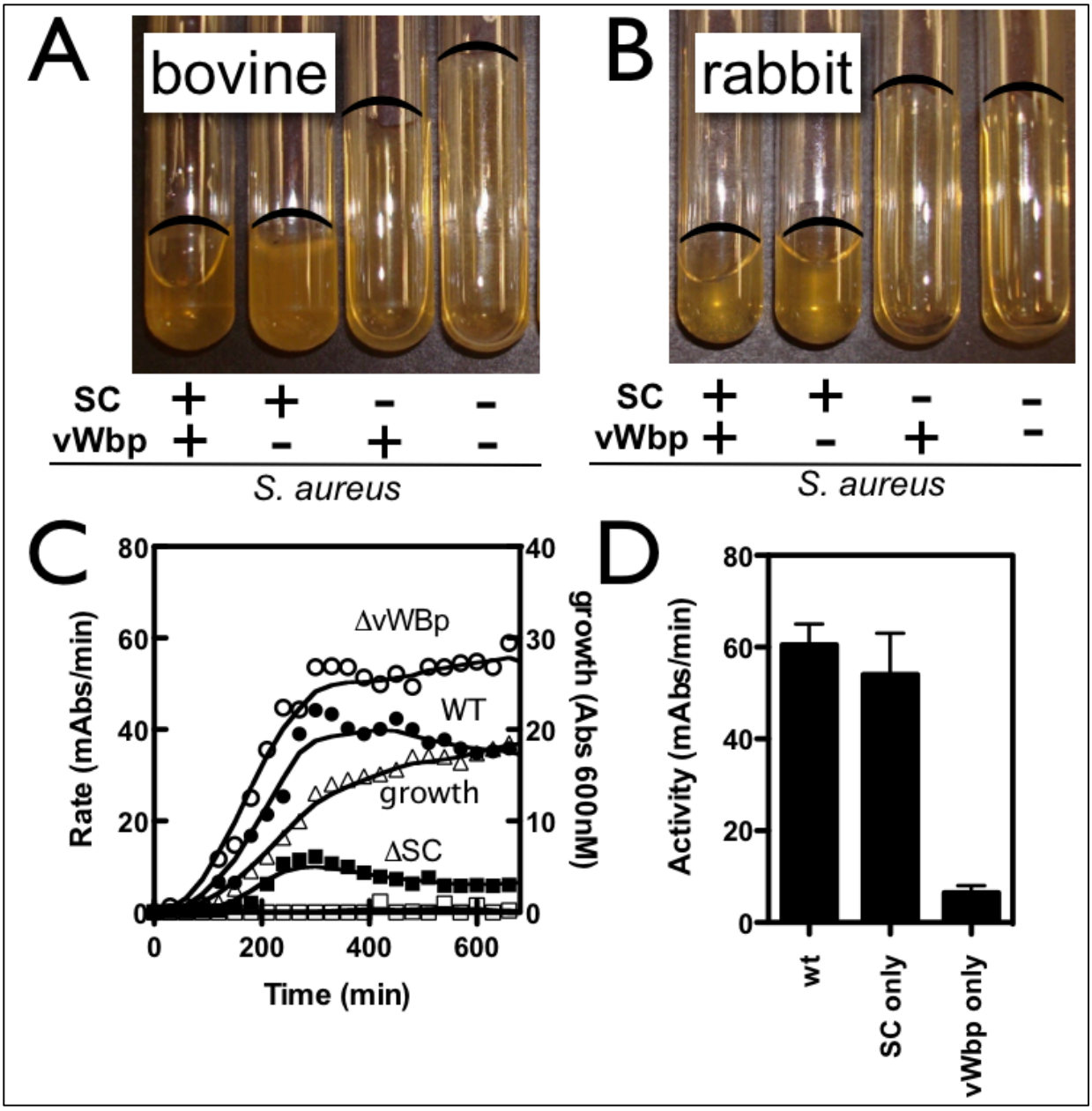

Figure 4.3. (**A**) and (**B**), Plasma clotting after addition of supernatants from overnight cultures of indicated *S. aureus* Newman mutant strains after 12 hours for bovine and rabbit plasma, respectively. (**C**), Growth curve assessment of overall prothrombin activation function of *S. aureus* Newman (WT) and *S. aureus* strains deficient in staphylocoagulase (ΔSC), vWbp (ΔvWBp) or both (ΔSCΔvWBp; □) deficient strain mutants. (**D**), Lysate activity (mAbs/min) of *S. aureus* Newman (WT), ΔSC, and ΔSCΔvWBp for catalysis of chromogenic human Fbg analogue, H-*D*-Phe-Pip-Arg-*p*NA.

Kinetic Analysis of SC^{RF122} Activation of Human and Bovine ProT

Kinetic constants determined from all assays are listed in *table 4.2*. The catalytic efficiency (K_{cat}/K_m) of SC^{RF122} for bovine ProT was shown to be slightly higher (80 $\mu M^{-1}s^{-1}(10^{-3})$) compared to that of $SC^{Tager104}$ (10 $\mu M^{-1}s^{-1}(10^{-3})$) (*figure 4.4; table 4.2*). However, the catalytic efficiencies of both $SC^{Tager104}$•BProT and SC^{RF122}•BProT were considerably lower than that of bovine thrombin or mouse ProT. The K_m of SC^{RF122} for human ProT was found to be 3.5 ± 0.3 μM, which was not significantly different than that of $SC^{Tager104}$ (1.2 ± 0.1 μM). However, the catalytic efficiency of $SC^{Tager104}$ to human ProT was approximately double that of SC^{RF122} (58,000 $\mu M^{-1}s^{-1}(10^{-3})$) compared to (23,500 $\mu M^{-1}s^{-1}(10^{-3})$).

The dissociation constants (Kd) for SC^{RF122} for human ProT, mouse ProT, and bovine ProT were determined to be 1.1 ± 0.2 nM, 2.7 ± 0.9 nM, and 9.9 ± 4.2 nM, respectively (*figure 4.6*). Contrastingly, determined Kd for $SC^{Tager104}$ to human ProT, mouse ProT, and bovine ProT were determined to be 2.5 ± 0.5 nM, 2.4 ± 0.6 nM, and 0.9 ± 0.6 nM, respectively. Human ProT constants were determined with 1 nM of enzyme, however due to the decreased catalytic efficiencies from activation by SC^{RF122} and $SC^{Tager104}$, it was necessary to increase the ProT concentrations of mouse ProT to 10 nM and 50 nM for bovine ProT.

Fluorescence titrations and competitive binding assays using [OG]FPR-ProT determined the kinetic profile of SC^{RF122} with native bovine ProT (*figures 4.7 and 4.8*). The determined K_m of SC^{RF122} to bovine ProT was 110 ± 30 μM, similar to the previously reported K_m of $SC^{Tager104}$ to bovine ProT (140 ± 50 μM)**.** These results indicate that there is little difference in affinity among SCs of RF122 and Tager 104 for bovine ProT.

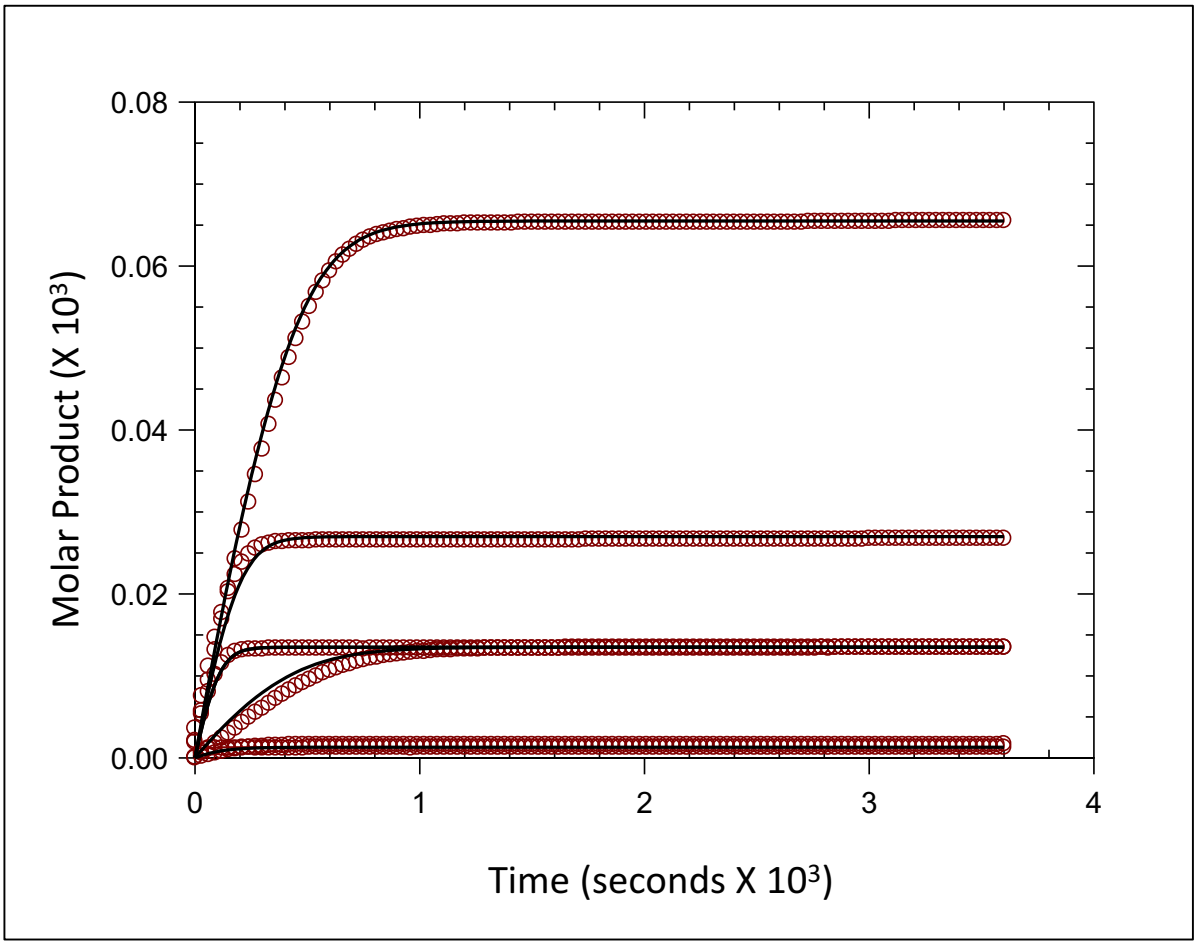

Figure 4.4. Progress-curve analysis of the SC^{RF122}•HProT complex hydrolysis of chromogenic Fbg analogue H-*D*-Phe-Pip-Arg-*p*NA. Lines through the data represent simultaneous fits of the integrated Michaelis-Menten equation to the observed data (○). Results are shown in *Table 4.2*.

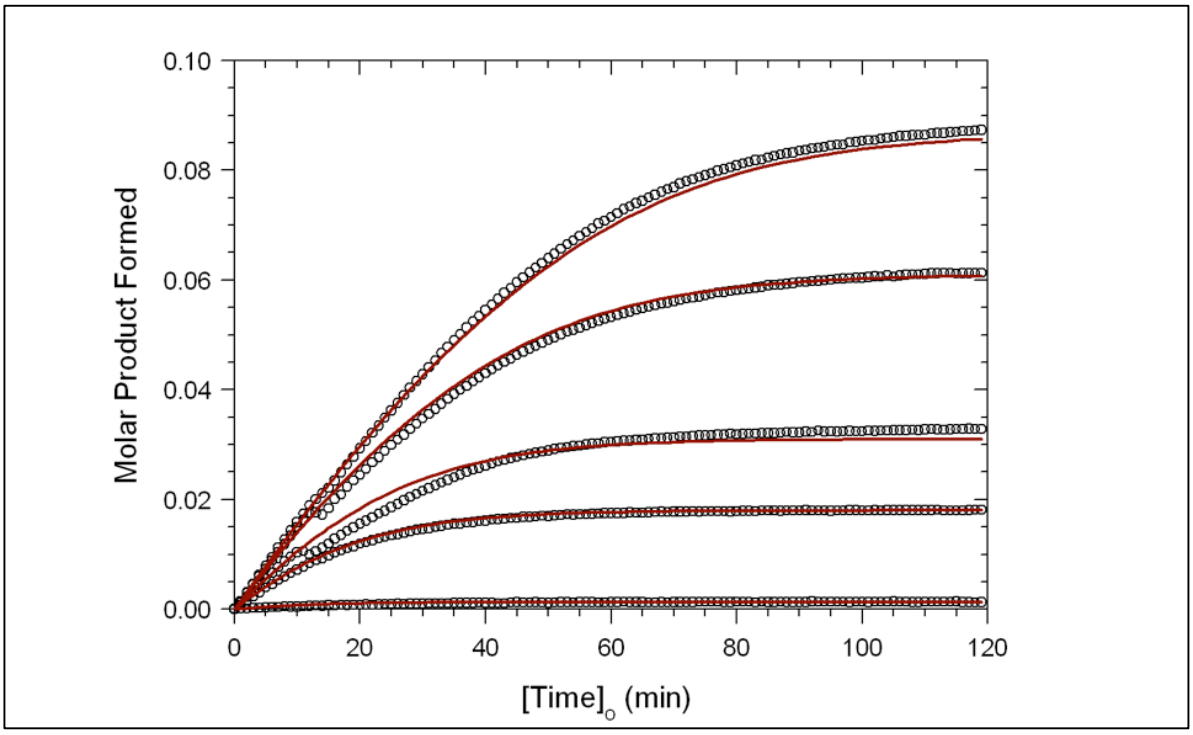

Figure 4.5. Progress-curve analysis of the SC^{RF122}•MProT complex hydrolysis of chromogenic Fbg analogue H-*D*-Phe-Pip-Arg-*p*NA. Lines through the data represent simultaneous fits of the integrated Michaelis-Menten equation to the observed data (○). Parameters are shown in *Table 4.2*.

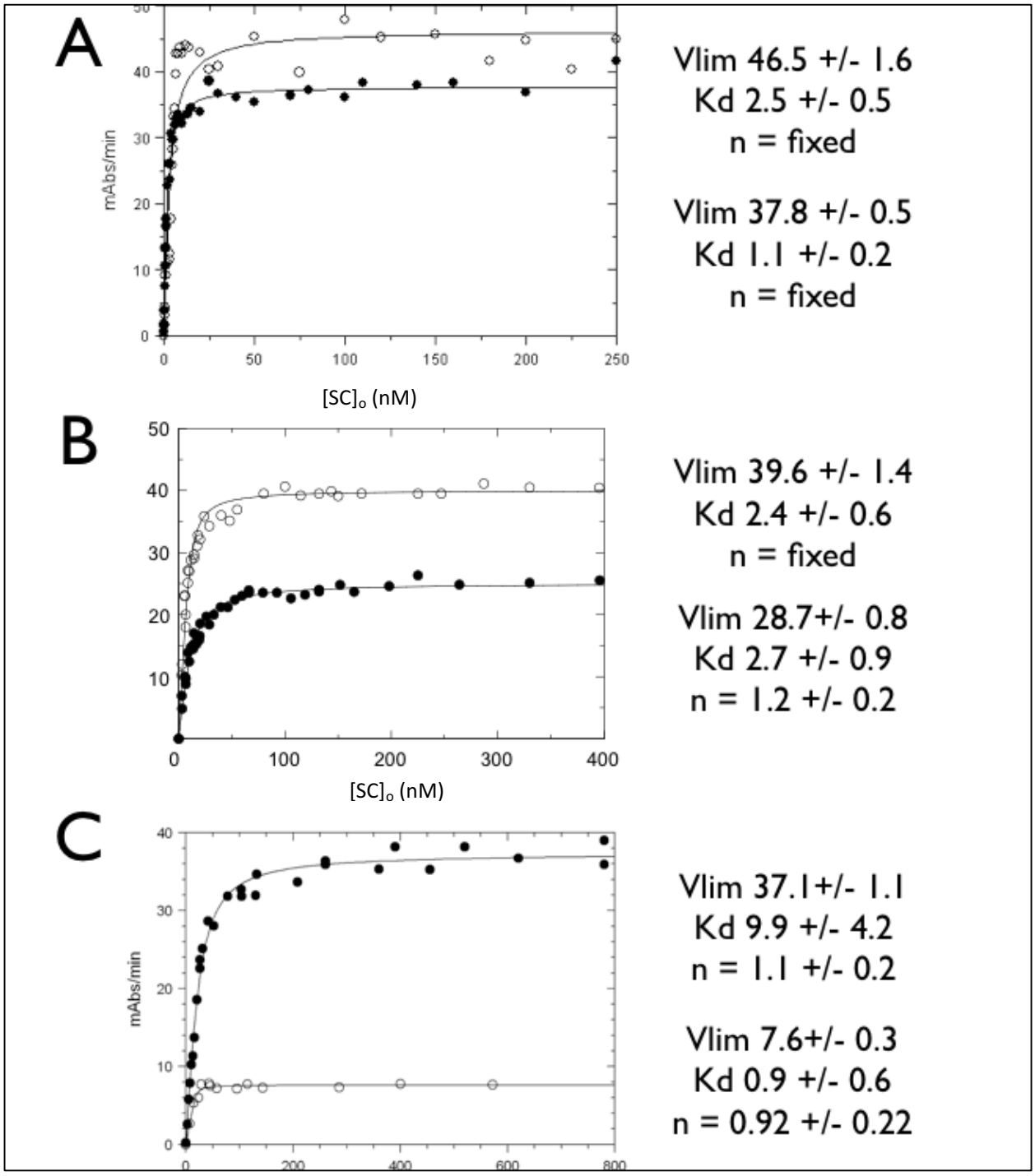

Figure 4.6. Activation of (**A**) Human ProT (1 nM), (**B**) mouse ProT (10 nM), and (**C**) bovine ProT (50 nM) by SC^{RF122} (●) and $SC^{Tager104}$ (○) through Δ absorbance measurements at 405 nm of H-*D*-Phe-Pip-Arg-*p*NA hydrolysis.

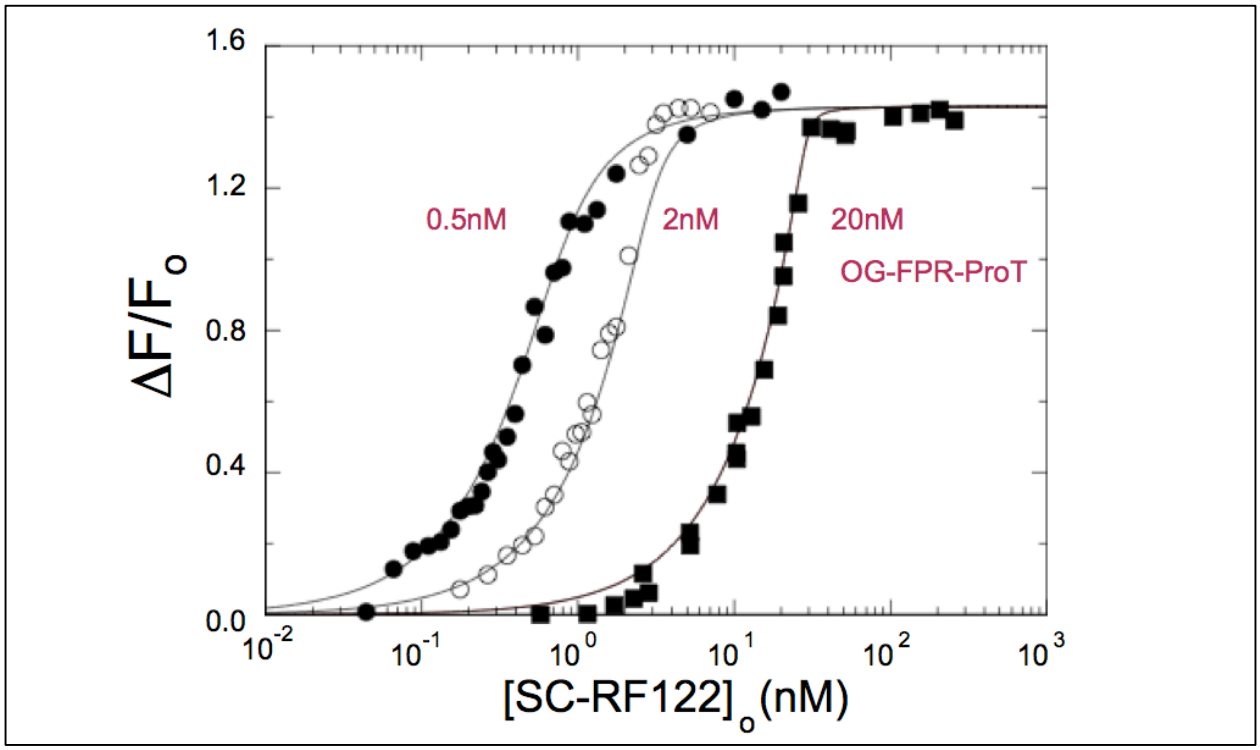

Figure 4.7. Fluorescence titrations of human [OG]FPR-ProT with SC^{RF122}-(1-320). The fractional change in fluorescence ($\Delta F/F_o$) plotted against the total concentration of SC^{RF122}-(1-320) ($[SC^{RF122}\text{-}(1\text{-}320)]_o$). (A), Titrations of 0.5 nM (●), 2 nM (○), and 20 nM (■) [OG]FPR-ProT. The lines represent the simultaneous fit of the data by the quadratic binding equation with the parameters given in the text. Results are shown in *Table 4.2*.

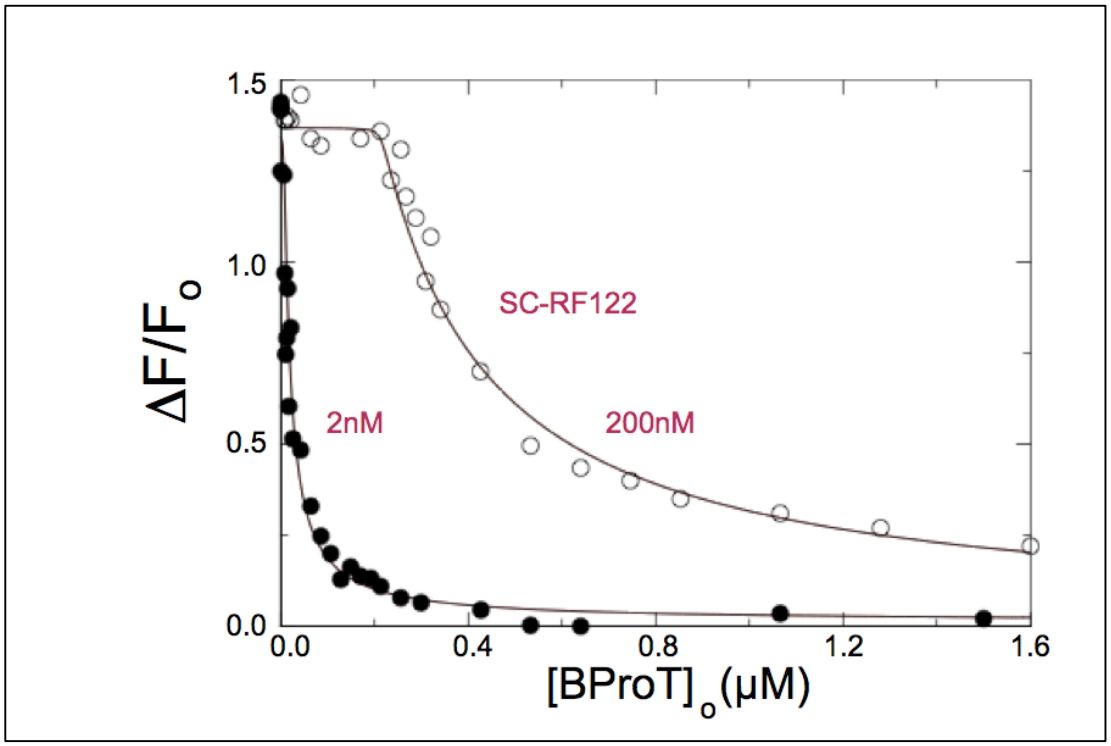

Figure 4.8. Competitive binding of SC^{RF122}-(1-320) to native bovine ProT and [OG]FPR-ProT. The fractional change in fluorescence ($\Delta F/F_o$) plotted against the total concentration of native Bovine ProT (*BProT*) at 2 (●), and 200 (○) nM SC^{RF122}-(1-320). The lines represent the fit by the cubic equation with the parameters given in the text. Results are shown in *Table 4.2*.

Enzyme	k_{cat}	K_m	k_{cat}/K_m	K_i
	(s^{-1})	(μM)	$(\mu M^{-1}s^{-1}x10^{-3})$	(μM)
Human thrombin	77 ± 1	2.5 ± 0.2	31000	11.5 ± 0.2
$SC^{Tager104}$•HProT	72.2 ± 0.1	1.2 ± 0.1	58000	6.2 ± 0.1
SC^{RF122}•HProT	82 ± 1	3.5 ± 0.3	23500	12.2 ± 1.3
Mouse thrombin	26 ± 1	1.46 ± 0.3	18000	7.5 ± 1.1
$SC^{Tager104}$•MProT	26 ± 1	14.2 ± 0.1	1800	163 ± 80
SC^{RF122}•MProT	14 ± 1	22 ± 1	640	102 ± 81
Bovine thrombin	94 ± 2	3 ± 1	35000	32 ± 2
$SC^{Tager104}$•BProT	1.4 ± 0.1	140 ± 50	10	
SC^{RF122}•BProT	9.1 ± 0.3	110 ± 30	80	

Table 4.2. Comparison of affinity and catalytic efficiency of $SC^{Tager104}$ and SC^{RF122} on activation of human, mouse and bovine ProT. Michaelis-Menten kinetic parameters determined for hydrolysis of H-*D*-Phe-Pip-Arg-*p*NA by the indicated enzyme species are listed. Kinetic parameters previously determined are listed for comparison.

Clotting Assay Demonstrates Species-Specific Clotting Efficiency Between SC^{RF122} and $SC^{Tager104}$ in Bovine and Human Plasma

Human or bovine plasma was incubated with preformed SC^{RF122}•ProT or $SC^{Tager\ 104}$•ProT complexes and clotting times were assessed using a fibrometer. Clotting times are plotted against the inverse concentration of enzyme complex used ($1/[E]_o$) for either SC^{RF122}-(1-320) and $SC^{Tager104}$ (*figure 4.9*). $SC^{Tager104}$ was more efficient at clotting human plasma by 2-fold versus SC^{RF122}. However, SC^{RF122} was more efficient at clotting bovine plasma by 12-fold against $SC^{Tager104}$. This result demonstrates the highly efficient species-specific clotting of SC^{RF122} in bovine plasma and supports the observation of species-specific clotting reported in the literature.

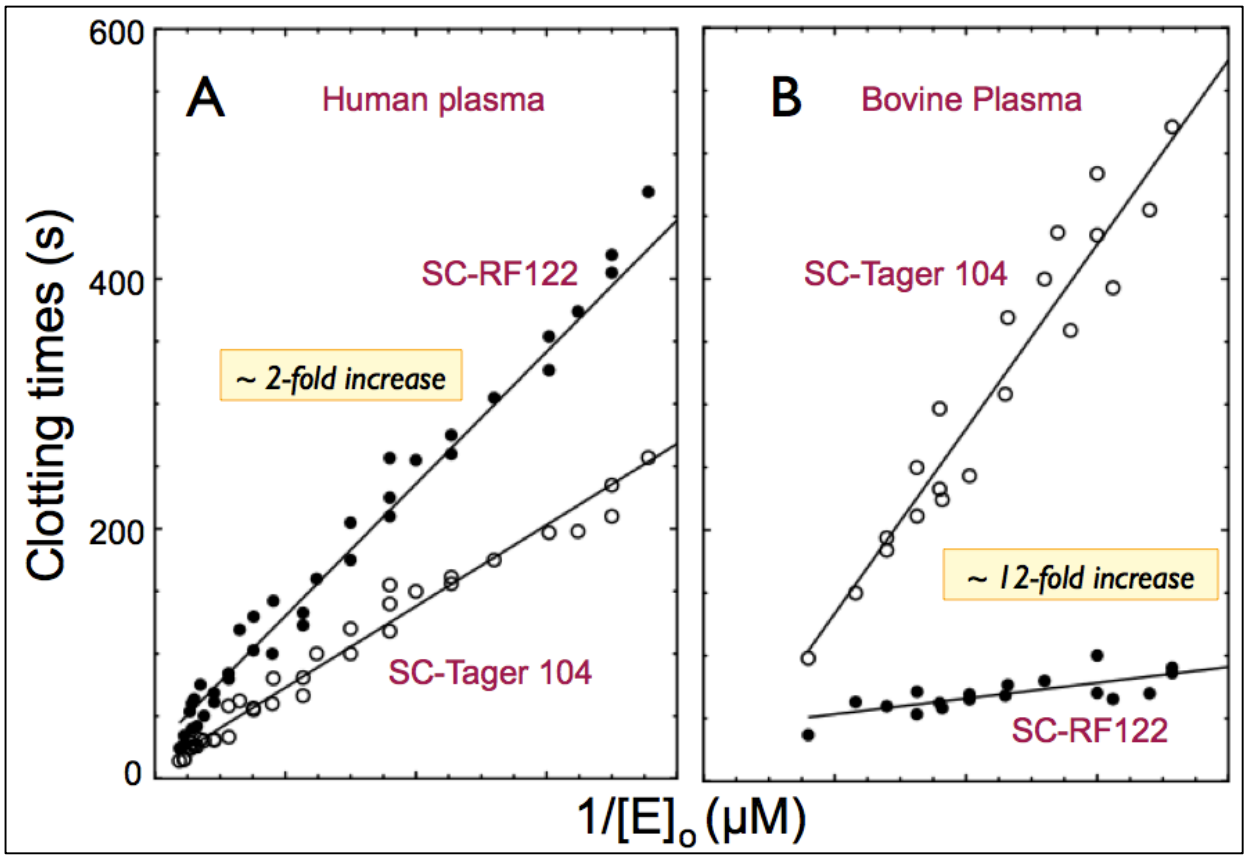

Figure 4.9. Comparison of clotting times by SC^{RF122}-(1-320)•ProT or $SC^{Tager104}$-(1-325)•ProT complexes in whole human or bovine plasma using a fibrometer. Human (**A**) or bovine (**B**) plasma was incubated with preformed SC^{RF122}•ProT or $SC^{Tager104}$•ProT complexes. Clotting times are plotted against the inverse concentration of enzyme complex used ($1/[E]_o$) for either SC^{RF122}-(1-320) (●) and $SC^{Tager104}$ (○).

Bovine ProT Purification from Whole Plasma using SC^{RF122}-(1-320-His_6) Bound to Nickel Column

Early fractions collected (fractions 2 and 3) resolved proteins in the molecular weight range of bovine ProT (~70 kD), SC^{RF122}-(1-320-His_6) (~40 kD), and fibrinogen (~340 kD), as denoted in *figure 4.10.* Another unidentified band at approximately 120 kD was also observed in these fractions. This results indicates that SC^{RF122}-(1-320-His_6) can not only bind bovine ProT from whole plasma, but Fbg may also be bound to the SC^{RF122}-(1-320-His_6)•BProT complex.

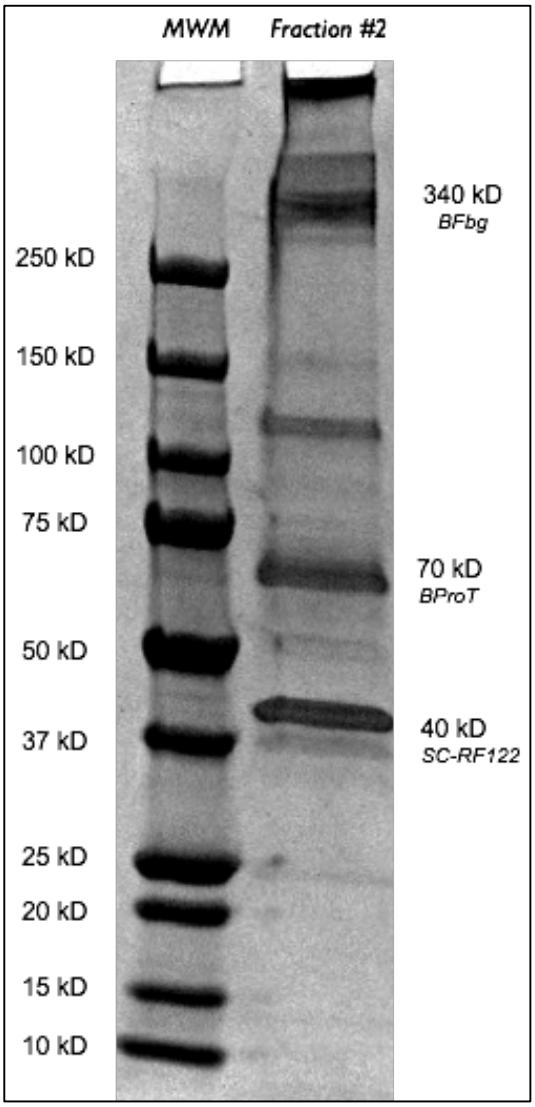

Figure 4.10. Fraction of whole bovine plasma elution over nickel column preloaded with SC^{RF122}-(1-320-His_6). Whole bovine plasma was run through the column and elution fractions were collected for SDS-PAGE.

Discussion

S. aureus is a heterogeneous pathogen which affects multiple species of humans and animals. Fibrin generation resulting from activation of ProT by SC and vWbp provides a physical barrier between the microbe and host immune cells and, ultimately, prevents immune clearance of the infection by direct evasion of endocytosis [40, 109]. There is evidence of species-specific clotting preference of *S. aureus* strains that suggest adaptations of procoagulant factors to suit particular host species zymogens. Despite recent advances in the understanding of SC and vWbp, their redundant function *in vivo* is less well understood. Questions also remain in regards to the necessity for this species-specific clot formation driven in host plasma between various species. In this study, we sought to specifically address one fundamental gap through a multi-faceted approach, employing biochemical, biophysical, and bioinformatics techniques.

A blast matrix of 11 *S. aureus* isolates from human, ruminant, and poultry origin was performed to determine protein homology both within and between isolates from each host origin. The results of the blast matrix did not reveal any obvious differences in protein homology among all of the strains tested. However, further analysis showed a significant difference ($p = 0.0170$) in the average of protein homology among all ruminant isolates tested and the average homology of all bovine and human isolates combined. Proteomic alignments of $SC^{Tager104}$-(1-325), SC^{Newman}-(1-325), and SC^{RF122}-(1-325) showed very high conservation among NH_2-terminal residues and residues which came into contact with the 148-loop or exosite-I. The alignment did not reveal any striking differences that would suggest specific adaptations for ProT of different origins.

Fluorescence titrations of SC^{RF122} with [OG]FPR-ProT and competitive binding assays with native bovine ProT showed no significant difference in affinity from that of $SC^{Tager104}$ to either human or bovine ProT. However, using a novel whole-plasma clotting assay, SC^{RF122} was found

to clot whole bovine plasma at a 12-fold higher efficiency than $SC^{Tager104}$ of human origin. Conversely, $SC^{Tager104}$ was only 2-fold more efficient at clotting human plasma than SC^{RF122}. It is important to note that the catalytic efficiency of the chromogenic Fbg-analogue hydrolysis by $SC^{Tager104}$•BProT and SC^{RF122}•BProT was significantly lower than that of other strains. We believe this unexpected result may be due to differences in the catalytic Fbg binding site of BProT, for which the H-*D*-Phe-Pip-Arg-*p*NA chromogenic Fbg-analogue may not be best suited.

Taken together, these results provide strong evidence that the species-specific zymogen activation by SC is not the result of affinity for a given host ProT, but rather the result of differences in the catalytic Fbg binding site in the zymogen•activator complex for various host species ProT. This research will lead to a better understanding of the mechanism behind species-specific preferences of host zymogen activation by bacterial ZAAPs. We believe that this improved understanding will facilitate the better design of drugs targeting infections in a given host, such as human and livestock-associated infections.

5. Conclusions and Future Directions

Future Directions for the MiSpinner

X-ray Computed Tomography using the MiSpinner

The IVIS Lumina XRMS imaging platform on which the MiSpinner was developed has an integrated cone-beam X-ray component intended to provide anatomical landmarks for overlaid bioluminescent and fluorescent signal. By acquiring planar X-ray 360° around an animal, we can create a pseudo-3-dimensional skeletal structure of an animal. Through collaborations with Dr. Stan Reeves and his student Huanyi Zhou in the Department of Electrical and Computer Engineering at Auburn University, we have been able to take this a step further with computed tomography reconstructions of these 360° planar X-ray images into a true 3-dimensional representation of an animal. While the quality and resolution of these reconstructions is not on the level of a proper micro-CT, this technology provides exceptional information for a fraction of the cost of a micro-CT system. *Figure 5.1* shows a reconstruction of a mouse fixed in agar (post-mortem) from preliminary testing of algorithms developed by Dr. Reeves and Huanyi. This was an exciting result for our first trial-run of this project and we are continuing to develop this technology to improve the quality and speed of reconstructions for future acquisitions. The next natural step is to attempt the reconstruction of 360° X-ray of a live mouse which will further prove the utility of this exciting technology. Another potential future direction for this technology may include bioluminescent and fluorescent tomography from 360° datasets overlaid on CT reconstructions. This would greatly improve the impact of studies involving bioluminescent and fluorescent reporters with a relatively low investment of additional capital, as the MiSpinner is an inexpensive modular add-on for the ubiquitous IVIS Lumina platform of preclinical imaging systems

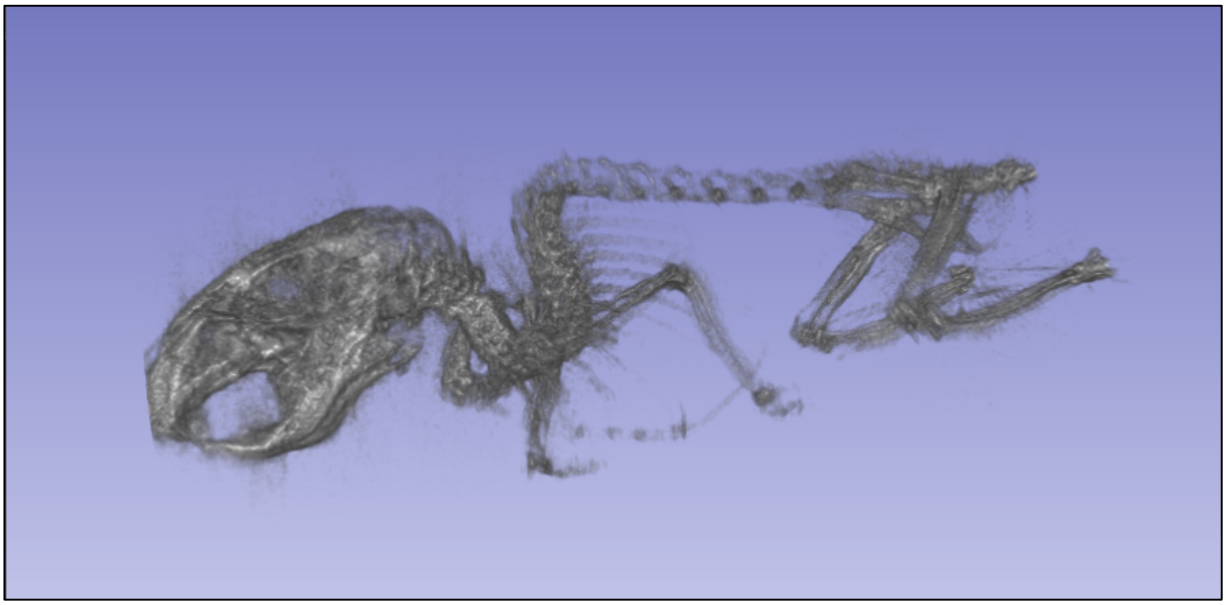

Figure 5.1. Computed tomography of fixed mouse from 360° planar X-ray acquired using the MiSpinner and IVIS Lumina XRMS.

Localization of Cancer Metastasis and Systemic Infection using the MiSpinner

One particularly useful application for multi-angle optical imaging using the MiSpinner may lie in localizing metastatic cancer cells or bacterial pathogens whose fate may not be easily determined by planar imaging alone. Typically to locate sites of cancer metastasis or bacterial infection in distance sites, researchers must manually flip animals around and acquire multiple angles in order to find the location of these cells. Even with acquiring multiple angles, it is difficult to determine the optimal angle for imaging these sites, or if all sites of interest have been localized. Incorporation of the MiSpinner into this process would provide a semi-automated and standardized method for acquiring comprehensive image data and should provide researchers with more reproducible data, particularly for longitudinal studies. The Panizzi lab has already begun to use the MiSpinner to localize sites of systemic *S. aureus* infection *in vivo* (*figure 5.2*). With the paradigm of cancer research shifting toward orthotopic and metastatic models, this technology could provide researchers with a means to produce reliable and reproducible data using these models without investing in more expensive imaging modalities, while retaining the high-throughput and ease of use that optical imaging modalities offer.

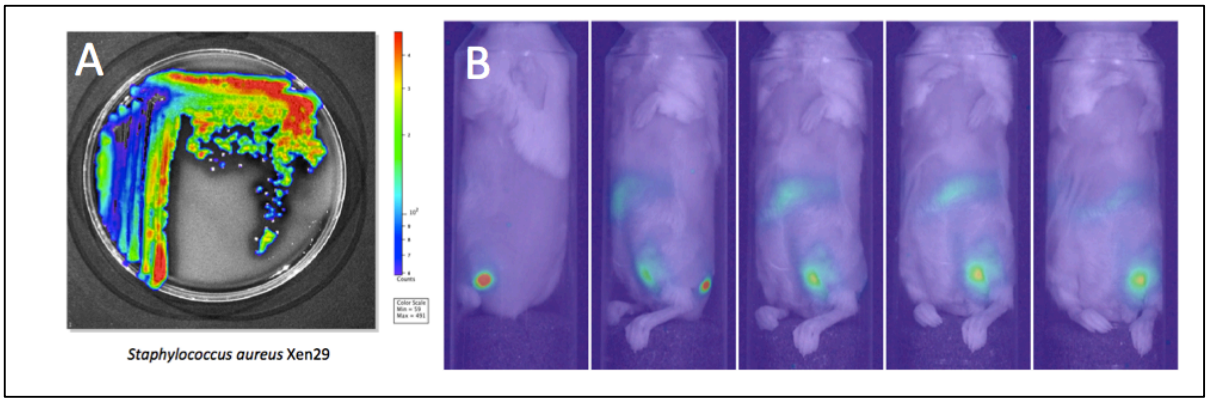

Figure 5.2. (**A-B**) Multi-angle BLI of a mouse injected with a bolus of *S. aureus* Xen29 using the MiSpinner. Using this method, we were easily able to identify distance sites of infection by Xen29 through segmental BLI. Figure adapted from poster presented at NanoBio Summit 2016 by authors Morgan Brazelle, Alec Wesolowski, Andrew Brannen, and Peter Panizzi entitled "*Multispectral Opto-Acoustic Tomography and Segmental 360-Degree Bioluminescent Imaging Both Show Potential for the Dynamic Study of Bacterial Infections*."

Future Directions and Applications for *B. amyloliquefaciens* AP183

The success of *B. amyloliquefaciens* AP183 in our cutaneous wound model has brought to mind several potential applications in both human medicine and agriculture. As mentioned in Chapter 3, there is an alarming rise in the carriage of LA-MRSA strains (e.g. ST398) among those who work with livestock, particularly with swine. However, this comes at a time when the use of antibiotics for livestock is becoming more tightly regulated due to the link between gross misuse of antibiotic drugs for livestock growth purposes and the rise of antibiotic resistant pathogens such as MRSA. This presents a unique challenge and a potential opportunity for innovative biocontrol strategies to be implemented in agricultural settings in lieu of antibiotic therapy. Another underappreciated agricultural burden is that of bovine mastitis in cows for milk production. The annual economic burden of bovine mastitis is estimated to be $1.7-2 billion dollars, with *S. aureus* as the major causative pathogen in approximately 20% of cases [67]. AP183 may be a promising biocontrol agent for each of these applications due to its potent inhibition of *S. aureus* and short half-life of the antibiotic metabolite bacillusin A. Although, further investigation of the safety and efficacy of AP183 is needed before use in animals that are intended for food production.

There is an inherent need for innovative strategies to combat antibiotic resistant pathogens in humans as well and there may be potential for the use of AP183 as a preemptive or adjunct biocontrol therapy. One potential application that we have discussed is the application of lyophilized AP183 spores to bandages to prevent colonization of pathogens, as well as maintenance of commensal microbial residents of the skin. This strategy may be beneficial to prevent infection in minor cuts and scrapes as a replacement for or adjunct to topical antibiotics such as polysporins. However, this strategy may also have potential in such cases as severe burns, wherein infection is readily established and is not easily treated. AP183 may be an ideal biocontrol

agent for application to burn dressings to prevent the establishment of infection from opportunistic pathogens such as *S. aureus* and, again, the short half-life of bioactive bacillusin A secreted from AP183 may also be advantageous in this setting.

Discussion and Future Directions for Species-Specific Clotting Project

In Chapter 4, we demonstrated that there is not a striking difference in proteomic homology between *S. aureus* strains of ruminant and human origin and that there is not a significant difference in affinity of the zymogen activator SC for human and bovine ProT. Despite these results, we demonstrated a 12-fold increase in clotting efficiency by SC^{RF122} over $SC^{Tager104}$ in whole bovine plasma. Taken together, these results indicate that the species-specific preference for clotting that has been reported in the literature is the result of differences in the catalytic Fbg binding site resulting from activation of ProT by staphylocoagulases of different *S. aureus* strains. During this study, we noticed that supernatants from RF122 had lower activity than human isolate strains such as Tager 104. We hypothesized that this difference may be the result of increased membrane expression of SC in RF122 strain compared to Tager 104. To test this hypothesis, we incubated log-phase and overnight strains of *S. aureus* RF122 and Tager 104 with [OG]FPR-ProT and used flow cytometry to analyze binding of probe to the cell surface. Coagulase-negative *Staphylococcus epidermidis* Xen43 was used as a control. One colony of each strain was picked from BHI plates and incubated at 37°C, shaking at 225 RPM in 50 mL of BHI broth overnight (16 hours). 50 mL of each culture was used to inoculate fresh BHI medium and incubated at 37°C shaking at 225 RPM and removed from incubation once OD_{600} nm reached approximately 0.5 (mid-log phase). Cultures from overnight (stationary phase) and mid-log phase growth were pelleted by centrifugation at 10,000 x g for 3 minutes. Pellets were resuspended in 1 mL of sterile

filtered 0.85% NaCl, then pelleted by centrifugation at 10,000 x g for 3 minutes. Pellets were resuspended with 1 mL of 0.85% NaCl again and OD_{600} nm was determined for each by a spectrophotometer. 10 µL of each sample was incubated with 4 µL of [OG]FPR-ProT, 1.5 µL of 3.34 mM propidium iodide and 1.5 µL of SYTO 9 (Live/Dead® BacLight™ kit from Invitrogen™), and 973 µL of 0.85% NaCl to a final volume of 1 mL in 3 mL polypropylene tubes. Samples were incubated for 45 minutes at room temperature in the absence of light. An Accuri C6 (BD Biosciences) was used to analyzed each sample. The preliminary results are shown in *figure 5.3*.

Our results show surface bound [OG]FPR-ProT is approximately 3-fold higher in log-phase RF122 than Tager 104. This indicates that during log-phase growth, RF122 expression of SC may be more highly surface bound than secretory. We hypothesize that surface expression of SC by RF122 may be beneficial to the pathogen for attachment in the mammary during bovine mastitis infection. Further work is needed to confirm this hypothesis, but this early result provides a promising direction for the future of this research.

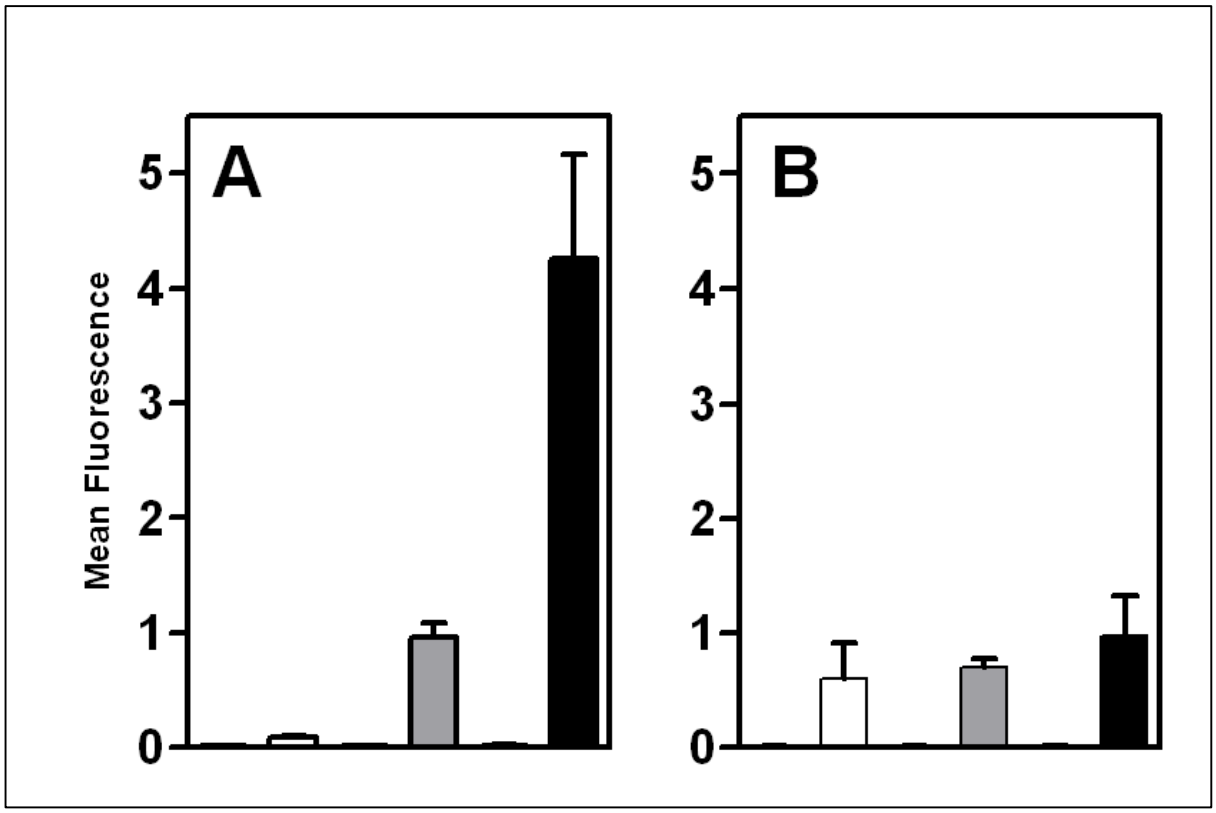

Figure 5.3. Flow cytometry analysis of [AF660]FPR-ProT binding among log and stationary phase *Staphylococcal* cell walls. Mean fluorescence of *S. epidermidis* (white), *S. aureus* Tager 104 (grey), and *S. aureus* RF122 (black) from log growth phase (**A**) and stationary phase (**B**).

Concluding Remarks

This dissertation is the compilation of three distinct projects involving the invention of a molecular imaging device, the evaluation of a novel probiotic, and the investigation of molecular adaptations by *S. aureus* strains that allow for species-specific preferential activation of host zymogens. While these may seem entirely unrelated on the surface, these projects may likely cross paths in their respective future directions. We demonstrated in Chapter 2 that incorporation of the multi-angle bioluminescent imaging using the MiSpinner improves longitudinal tracking of tumor growth. While this study involved the use of a cancer model, this technology will certainly be useful for localizing sites of systemic infection using bioluminescent or fluorescent bacteria. We are currently looking into the application of AP183 for the treatment and prevention of *S. aureus*-causative bovine mastitis and other applications for biocontrol of pathogenic bacteria. There are numerous possibilities for new directions of each of these projects and I look forward to seeing the progress that will be made for each in the future.

S1. Supplementary Chapter - Published Second-Author Paper:

Complete Genome of *Staphylococcus aureus* Tager 104 Provides Evidence of Its Relation to Modern Systemic Hospital-Acquired Strains

Richard W. Davis IV[1] (davisri@auburn.edu), **Andrew D. Brannen[1]** (adb0009@auburn.edu), Mohammad J. Hossain[2] (mjh0007@auburn.edu), Scott Monsma[3] (smonsma@lucigen.com), Paul E. Bock[4] (paul.bock@vanderbilt.edu), Matthias Nahrendorf[5](mnahrendorf@mgh.harvard.edu), David Mead[3] (dmead@lucigen.com), Michael Lodes[3] (mlodes@lucigen.com), Mark R. Liles[2] (lilesma@auburn.edu), Peter Panizzi (panizzi@auburn.edu)[1,6]

[1]Department of Drug Discovery and Development, Harrison School of Pharmacy, 4306 Walker Building, Auburn University, Auburn, AL 36849
[2]Department of Biological Sciences, 101 Rouse Life Science Building, Auburn University, Auburn, AL 36849
[3]Lucigen Corporation, 2905 Parmenter St, Middleton, WI 53562
[4]Department of Pathology, Microbiology, and Immunology, Vanderbilt University Medical Center, Nashville, TN 37232, USA
[5]Center for Systems Biology, Massachusetts General Hospital and Harvard Medical School, Simches Research Building, 185 Cambridge St., Boston, MA 02114, USA

RUNNING TITLE: TAGER104 GENOME AND ANALYSIS

[6]Address correspondence to: Dr. Peter Panizzi, Department of Drug Discovery and Development, Auburn University, 3211-J Walker Building, Auburn, AL 36849, Tel: 334-844-7941, Fax: 334-844-8331, E-mail: panizzi@auburn.edu.

Abstract

Background: *Staphylococcus aureus* (*S. aureus*) infections range in severity due to expression of certain virulence factors encoded on mobile genetic elements (MGE). As such, characterization of these MGE, as well as single nucleotide polymorphisms is of high clinical and microbiological importance. To understand the evolution of these dangerous pathogens, it is paramount to define reference strains that may predate MGE acquisition. One such candidate is *S. aureus* Tager 104, a previously uncharacterized strain isolated from a patient with impetigo in 1947.

Results: We show here that *S. aureus* Tager 104 can survive in the bloodstream and infect naïve organs. We also demonstrate a procedure to construct and validate the assembly of *S. aureus* genomes, using Tager 104 as a proof-of-concept. In so doing, we bridged confounding gap regions that limited our initial attempts to close this 2.82 Mb genome, through integration of data from Illumina Nextera paired-end, PacBio RS, and Lucigen NxSeq mate-pair libraries. Furthermore, we provide independent confirmation of our segmental arrangement of the Tager 104 genome by the sole use of Lucigen NxSeq libraries filled by paired-end MiSeq reads and alignment with SPAdes software. Genomic analysis of Tager 104 revealed limited MGE, and a νSaβ island configuration that is reminiscent of other hospital acquired *S. aureus* genomes.

Conclusions: Tager 104 represents an early-branching ancestor of certain hospital-acquired strains. Combined with its earlier isolation date and limited content of MGE, Tager 104 can serve as a viable reference for future comparative genome studies.

Introduction

The prevalence of methicillin-resistance in *Staphylococcus aureus* (*S. aureus*) is a global threat as noted by the Centers for Disease Control and Prevention 2013 Threat Report [145]. *S. aureus* strains are heterogeneous, and therefore can cause a wide range of localized infections, such as impetigo and cellulitis, to more serious systemic infections, such as bacterial endocarditis and sepsis. In particular, *S. aureus* is the leading cause of bacterial endocarditis, a disease with mortality rates as high as 25-47%, even in the presence of antibiotic therapy [146]. This wide range of infections, as well as the growing number of pathogens with diverse antibiotic resistance profiles, is due to the acquisition of mobile genetic elements (MGEs) that grant heterogeneity to *S. aureus* strains. The best described of these MGEs is the Staphylococcal Cassette Chromosome *mec* (SCCmec) operon, which encodes the *mecA* gene and confers methicillin resistance [147]. However, many other MGEs can confer adaptive advantages during infection, such as enterotoxins [148], leukocidins (most prominently the Panton-Valentine leukocidin, *pvl*, encoded by the *lukF-PV* and *lukS-PV* genes) [147, 148], staphylokinase (*sak*) [149], and the toxic shock syndrome toxin-1 [150]. Therefore, there is an urgent need to better understand the evolutionary adaptations commonly associated with acquisition of MGE that contribute to (i) the prevalence of nosocomial infections, (ii) the rapid spread of community-acquired strains, (iii) development and expansion of novel resistance mechanisms, and (iv) natural host selection and propagation pathways.

To juxtapose recent next-generation sequencing efforts with pathogenic potential, it is necessary to have several well-characterized reference strains to use as landmarks to interpret MGE findings. This is currently lacking in the field, as the most popular strains (i.e. methicillin-sensitive *S. aureus* (MSSA) Newman [9], methicillin-resistant *S. aureus* (MRSA) USA300 [151], and vancomycin-resistant *S. aureus* (VRSA) Mu50 [148, 152]) are complicated by horizontal gene

transfer of MGE and inclusion of various prophages that were gained to most likely provide some sort of survival advantage. As such, it is prudent to define strains with a balance between limited MGE presence and potent pathogenic potential.

Here we describe one such strain, which we term *S. aureus* Tager 104. Tager 104 was originally isolated at the New Haven Hospital (New Haven, Connecticut) by Morris Tager *et al*. in 1947 from a patient with a cutaneous infection caused by a hemolytic bacteria [153, 154]. As a comparison, the first strain of methicillin-resistant *S. aureus* was isolated in 1961 [147]. Morris Tager and co-workers subsequently demonstrated that *S. aureus* Tager 104 induced clotting through expression of secreted factors [155], developed staphylocoagulase purification protocols [156], and initiated preliminary characterization of staphylocoagulase function in contrast to normal physiologic clotting [157, 158]. Currently, staphylocoagulase from *S. aureus* Tager 104 is arguably the most well characterized prothrombin activator studied to date, as it was the original source used to solve the staphylocoagulase (1-325) fragment crystal structure in complex with both thrombin and its immediate precursor, prethrombin 2 [8]. This recombinant N-terminal fragment of staphylocoagulase from Tager 104 binds with high affinity (K_D 17-72 pM) to the human prothrombin zymogen [159], which was also used to characterize fibrinogen recognition by the prothrombin-staphylocoagulase complex and to determine that two prothrombin-staphylocoagulase complexes bind to a single substrate fibrinogen molecule to mediate cleavage [118]. With the wealth of biochemical insight that has been generated from Tager 104 virulence factors, the genomic characterization has merit from both clinical and evolutionary perspectives.

Materials and Methods

Ethics Statement

For this study, 12 C57BL/6 mice were purchased from The Jackson Laboratories (Bar Harbor, ME). Mice were housed at the either Auburn University College of Veterinary Medicine or Massachusetts General Hospital with *ad libitum* access to alfalfa-free chow and water. All procedures were designed in accordance with the Guide for the Care and Use of Laboratory Animals of the National Institutes of Health and approved by the Institutional Animal Care and Use Committee of Auburn University for this sepsis model under protocol 2014-2427. *S. aureus* strain Tager 104 was obtained as a depersonalized human isolate from an outside source and therefore no ethics approval was required for its use in this study.

Mouse Model of Systemic Infection

For this experiment, 12 female C57BL/6 were anesthetized with 1-3% isoflurane mixed with medical grade oxygen using a vaporizer. *S. aureus* Tager 104 was grown overnight at 37ºC in 50 mL of brain-heart infusion (BHI) broth in a 125 mL Erlenmeyer flask. Cells were twice washed with 40 mL of filter-sterilized phosphate buffered saline (PBS) supplemented with 10% glycerol. Cells were pelleted by centrifugation at 10,000 x *g* for 10 min and the cell pellet was re-suspended in a final volume of 10 mL of PBS with 10% glycerol. A sample from this inoculum stock was diluted 1:100 in PBS with 10% glycerol in a cuvette for determination of cell density by measuring the absorbance at an optical density (O.D.) at 600 nm using a Beckman Coulter DU800 spectrophotometer. These freshly prepared inoculums were used to inject into these 12 female C57BL/6 mice by tail-vein with 5×10^8 colony forming units (CFU). After 24 hours, the animals were euthanized.

Histology

Organs were harvested, stored in 4% paraformaldehyde, and embedded in optimal cutting temperature (OCT) medium by immersing in 4-methylbutane in a metal canister within a dry-ice bath. Slices (10 microns in width) were made using a Thermo HM550 Cryostat set at -19°C, and fixed to poly-L-lysine coated slides. Slides were then stained using standard Gram and hematoxylin and eosin (H&E) staining protocols. Slides were viewed at 100 or 400 times total magnification on a Zeiss Axioskop 40 microscope, and images were taken using a Nikon DS-Fi1 camera head and DS-L3 control unit.

Lucigen NxSeq Library Construction

Genomic DNAs were prepared by E.Z.N.A. Bacterial D.N.A. kit (Omega Bio-tek, Norcross, GA). All genomic DNA preparations were evaluated for approximate size and integrity by Pulsed Field Gel Electrophoresis with a BioRad CHEF-DR III instrument. Fragment Libraries were constructed with a NxSeq DNA Sample Prep Kit (Lucigen). Briefly, genomic DNAs were sheared to approximately 500 to 700 bp with a Covaris instrument and fragment size was confirmed by agarose gel electrophoresis. Five hundred ng sheared DNA was mixed with 2X buffer and a cocktail of end repair and tailing enzymes and then incubated at 25 °C for 20 min and then 72 °C for 25 min. Illumina sequencing adaptors and ligase were then added and the tubes were incubated at 25 °C for 30 min prior to size selection with Agencourt AMPure XP beads (Beckman Coulter). Fragment libraries were then quantified with a 2100 Bioanalyzer (Agilent Technologies), sequenced on a MiSeq Sequencer (Illumina) and 2 x 250 paired end reads were exported for analysis.

Mate Pair Libraries

Insert preparation, size selection and library construction followed the NxSeq® 8 kb Long Mate Pair Library Kit. Briefly, 8 kb mate pair library insert was sheared to approximately 10 kb with either a Megaruptor (Diagenode Inc., Denville, NJ) or a g-TUBE (Covaris, Woburn, MA). Sheared DNA was bead-cleaned and then size-selected with Agencourt AMPure XP beads. After size selection and quantification with a Qubit 2.0 Fluorometer (ThermoFisher), 400 ng of insert was ligated to a coupler at a concentration of 1 ng/μL for 16 hrs at 16 °C. Unligated DNA was removed by digestion with exonucleases and the circularized DNA was purified with Agencourt AMPure XP beads. Purified DNA was then digested with endonucleases (ThermoFisher) to remove DNA between the two ditags, and the ditag-ligated coupler was purified by biotin capture with MyOne C1 streptavidin magnetic beads (ThermoFisher). The purified ditag-ligated coupler was then G-tailed and ligated to a C-Tailed Junction Code adaptor. After bead cleaning to remove unligated adaptor, the Junction Code adapted DNA was re-circularized at low concentration, cleaned with Agencourt AMPure XP beads and then amplified with Accura HF Hot Start Master Mix (Lucigen) and indexed primers.

Construction of 20 kb mate pair libraries followed the NxSeq® 20 kb Long Mate Pair Library Kit protocol. Briefly, 15 μg of high molecular weight genomic DNA was sheared to 20 kb with a g-TUBE at 4500 rpm, end repaired, A-tailed and ligated to adaptors prior to precipitation and resuspension in 10 mM Tris. Adapted insert was gel-isolated either with a BluePippin instrument (Sage Science) or by separation on a 0.3% SeaKem Gold agarose (Lonza) followed by electroelution with an EluTrap device (Whatman). Gel-isolated insert was then quantified by Qubit and 1 μg of insert was ligated to a coupler at a concentration of 1.25 ng/μL for 16 hrs at 4

°C. Unligated DNA was removed by digestion with exonucleases and the circularized DNA was purified by alcohol precipitation. The 20 kb protocol continues with endonuclease digestion as described above for the 8 kb mate pair protocol. Mate pair libraries were quantified with a 2100 Bioanalyzer, sequenced on a MiSeq Sequencer (Illumina) and 2 x 250 paired end reads were exported for subsequent filtering and trimming.

True mate pairs were filtered by analysis and trimming of Chimera Code coupler sequences using the Chimera-Clean5 Python script (Lucigen); junctions between left and right di-tags were identified by presence of the Junction Code linker and di-tags extracted using the JunctionSplit9 Python script (Lucigen).

Tager 104 Genome Construction

Genomic DNA was extracted from Tager 104 using E.Z.N.A. Bacterial D.N.A. kit (Omega Bio-tek, Norcross, GA), and constructed into a bar-coded library using the Nextera DNA sample preparation kit (Illumina, San Diego, CA). Sequencing was performed using an Illumina MiSeq sequencer for 2 × 150 paired end reads and trimmed sequence reads were assembled *de novo* using CLC Bio v. 4.6.1, as described previously [144]. To scaffold these contigs, a sub-library of Tager 104 was constructed for PacBio SMRT sequencing. Two sequencing reactions were performed, and CLC bio contigs were scaffolded using Celera Assembler pipeline on the SMRT analysis 1.3 suite [144].

To overcome the innate difficulty in genome closure in this initial construction, PacBio reads were instead assembled *de novo* using SMRT Analysis v. 2.0 Hierarchical Genome Assembly Process (HGAP) algorithm [160], which produced 8 contigs. To close the genome, two Lucigen NxSeq 20 kb mate-pair libraries were constructed and sequenced on an Illumina HiSeq

system. PacBio HGAP scaffolds and Lucigen NxSeq paired-end reads from the mate-pair library were provided to SSAKE-based scaffolding of Pre-Assembled Contigs after Extension (SSPACE) [161] for assembly *de novo* to create the closed draft genome. Gap regions in this genome were closed using a combination of the GapFiller algorithm (as part of the SSPACE suite) and Basic Local Alignment Search Tool (BLAST) search against the initial CLC contigs for those which bridge gap regions. This complete, circular genome was submitted to the Rapid Annotation using Subsystem Technology (RAST) server [162-164].

To confirm the construction of Tager 104 using an independent method, new libraries were constructed using the Nextera DNA kit and sequenced using Illumina MiSeq 2 × 250 reactions. These results were combined using the St. Petersburg genome assembler (SPAdes) algorithm [165] for genome closure.

Construction Validation and Analysis

To test the contribution of repeats to the shortcomings in genome assembly, long repeats (> 500 bp) were identified using Nucmer mapping of the Tager 104 genome to itself [166] and selecting for regions with unique locations and proper size. In addition, interspersed repeats and RNA sequences were identified using the RepeatMasker algorithm (www.repeatmasker.org). The coordinates of unique repeats were recorded and provided to Circos version 0.64 (www.circos.ca).

To determine the contribution of Illumina MiSeq contigs (constructed using CLC), PacBio RS sequencing reads, and scaffolds constructed from the combination of the two, results from each assembly were mapped to the Tager 104 genome using Nucmer. The locations of each unique mapping were provided to Circos for visualization.

MLST Analysis

To compare the lineage of Tager 104 to other clinical *S. aureus* strains, we employed multi-locus sequence typing (MLST). FASTA-formatted genomic sequences of completed *S. aureus* genomes were obtained from the RefSeq database on GenBank and uploaded to CLC Workbench. The identity of the seven housekeeping genes (carbamate kinase, *arc;* shikimate dehydrogenase, *aro*; glycerol kinase, *glp*; guanylate kinase, *gmk*; phosphate acetyltransferase, *pta*; triosephosphate isomerase, *tpi*; acetyl coenzyme A acetyltransferase, *yqi*) were determined *in silico* using the MLST module (http://www.clcbio.com/clc-plugin/mlst/). The sequence type of Tager 104 was determined previously to be ST49, as outlined elsewhere [144].

Proteomic Analysis of Tager 104 Genome

To perform whole-genome comparisons of Tager 104 to reference *S. aureus* strains, a CMG-Biotools virtual machine was graciously provided by Dr. David Ussery [137]. One reference genome was selected from each ST group represented in MLST analysis. Each genome sequence was downloaded from GenBank using the getgbk (*i.e.*, content) function, and converted into FASTA files using saco_convert. These files were then submitted to the prodigalrunner algorithm to process the open reading frames and create a protein FASTA file. The makebmdest and blastmatrix algorithms were then utilized to construct BLAST matrices using one representative from each ST.

Whole-Genome Phylogenetic Analysis

The Tager 104 genome and the GenBank reference sequence genomes were obtained from RAST and GenBank, respectively. Genomes were submitted to alignment by the Mauve algorithm

using default parameters [167]. Orthologs were extracted from the resulting .xmfa file using stripSubsetLCBs (http://gel.ahabs.wisc.edu/mauve/snapshots/2012/2012-06-07/linux-x64) with the minimum locally colinear blocks length set to 500 bp and the number of genomes set to 75. The result was then converted to FASTA format using the xmfa2fasta.pl script, and the FASTA-formatted alignment was then converted to phylip format using the fasta2phylip.pl script (both parts of the BioPerl package) (www.bioperl.org). To construct the phylogenetic tree, a maximum-likelihood tree was constructed using the RAxML program on the Cyberinfrastructure for Phylogenetic Research (CIPRES) Science Gateway using default settings (www.phylo.org/portal2/home.action), and the image was constructed using FigTree (tree.bio.ed.ac.uk/software/figtree).

MGE-encoded Gene Determinations

The list of MGE-encoded predicted virulence factors was determined based on previous studies by our lab and others, and reviewed elsewhere [147]. The RAST server was first searched for the presence of each protein-encoding gene (PEG). In cases where no annotated PEG was detected, the UniProt server (www.uniprot.org) was used to obtain DNA sequences for BLAST analysis. The genetic location of these elements was recorded and provided to Circos for graphic representation.

To compare genomes of the Tager clade, we utilized the BLAST Ring Image Generator (BRIG) algorithm (http://brig.sourceforge.net/) with default parameters [168].

Genomic islands were determined using the IslandViewer 3 algorithm, available online at http://www.pathogenomics.sfu.ca/islandviewer. Islands were identified based on their genetic content, as reported by the IslandViewer output and BLAST analysis.

For the νSaβ genomic island, genomic profiles were constructed using the RAST server. After determination of the profile, open reading frames were recolored based on their family or function.

Antibiotic Susceptibility Testing

S. aureus Tager 104 was streaked for a lawn on trypticase soy agar (TSA) plates containing 5% sheep blood (BD Biosciences). E-test strips for erythromycin (ER), linezolid (LZ), oxacillin (OX), and vancomycin (VA) (bioMérieux, Inc.) were then placed onto the surface of the agar using sterile forceps. All resistance tests were performed under conditions that were naïve for the *S. aureus* Tager 104 strain to not complicate interpretation by inducing vancomycin-resistance. Bacteria were incubated at 37^{o}C for 17 hours and plates were imaged using an IVIS Lumina XR system. In addition, overnight cultures of *S. aureus* Tager 104 were added at a 1:200 ratio to wells containing BHI broth and serial diluted concentrations of vancomycin. The 96-well plate was incubated for 17 hours in an incubator and the O.D.$_{600nm}$ was determined using a Thermo Scientific VarioSkan plate reader. Data was subsequently plotted using Graph Pad Prism v4.03.

Results

S. aureus Tager 104 Abscess Formation in Naïve Tissue

Histology indicates that *S. aureus* Tager 104 is able to colonize all tissue with variable coverage at this time point as indicated by Gram staining (*figure S.1*). Bacteria were detected in the alveoli cells of the lung and glomerulus of the kidney. This supports the previous hypothesis that Tager 104 is capable of systemic spread. Given our previous studies [69, 169], we now know that Tager 104 can cause both endocarditis and establish abscesses in naïve tissue. We sought to

better characterize this Tager 104 at a genomic level to consider all potential virulence determinants prior to comparative virulence studies with other *S. aureus* strains.

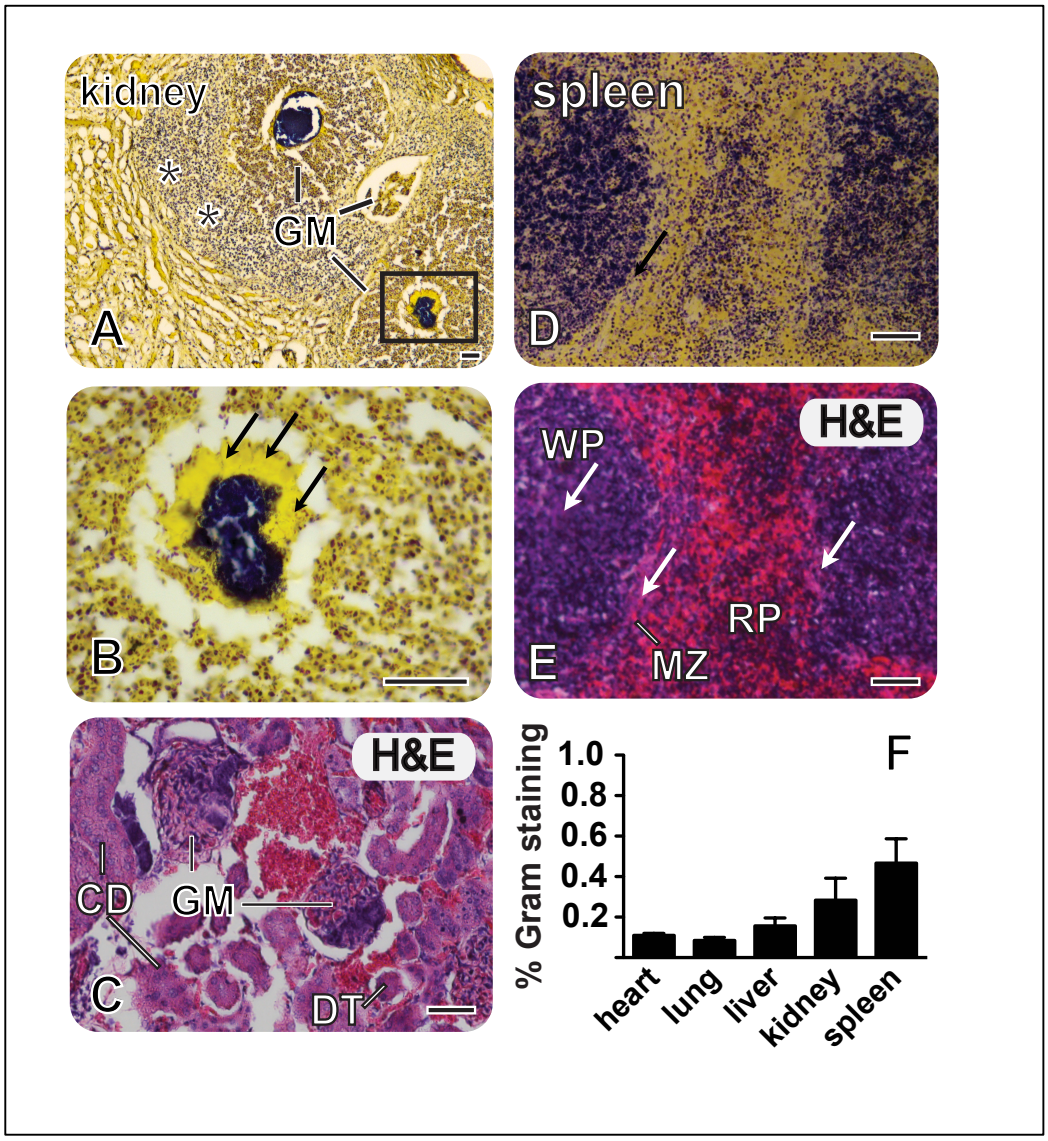

Figure S.1. *S. aureus* Tager 104 Bacteremia Leading to Multi-organ Septic Foci. **a** Gram staining of C57BL/6 kidney 8 days after injection of 5 × 108 CFU *S. aureus* Tager 104. **b** Higher magnification (400× total) of the indicated by the box in panel **a**. Arrows indicate the protective fibrin layer that allows the bacteria to thrive in the glomerulus (GM) without the threat of clearance by phagocytic immune cells (see area immediately surrounding infected GM shown in Panel **a**). **c** Adjacent section of the same kidney stained with Hematoxylin and Eosin (H&E); please note the GM is at a slightly earlier stage of the disease. Kidney architecture including the collecting ducts (CD), the distal tubule (DT), and blood cells (red). **d** Gram staining shows bacteria (purple) in all organs examined; splenic abscesses also show thickening of the marginal zone and increased fibrin deposition (arrows). **e** Adjacent section stained for H&E showing the splenic architecture including the white pulp (WP) region, marginal zone (MZ) and red pulp (RP) region.

Construction of S. aureus Tager 104 Genome

To close the *S. aureus* Tager 104 genome, three different sequencing technologies were used: Illumina Miseq 2 × 150 bp reactions, PacBio RS 90-minute movies, and Lucigen NxSeq 20 kb mate-pair libraries. In all approaches, scaffolds were constructed using one of either Illumina MiSeq or PacBio RS, or a combination of the two (hybrid assembly).

We first sought to close the hybrid assembly scaffolds previously produced for Tager 104 [144]. Therefore, these scaffolds were submitted to the SSPACE algorithm with the Lucigen NxSeq mate pair sequences. This approach successfully closed the genome, producing the 2.8 Mb *S. aureus* genome. However, this approach left six large gaps in the assembly, which would have required significant manual closure.

Therefore, we instead tested the ability of PacBio RS sequencing reactions in combination with NxSeq mate-pair libraries. Scaffolds were produced using the Hierarchical Genome Assembly Process (HGAP) assembly algorithm on the PacBio SMRT Analysis suite (v 2.0) [160]. This algorithm produced 8 scaffolds from raw sequencing data, with an N50 value of 1,028,373 bp. These scaffolds were then closed using de-duplicated NxSeq reads using SSPACE. When possible, small gaps were filled by aligning CLC-constructed Illumina contigs to the genome using a BLAST search. The result was a closed 2.82 Mbp genome (*figure S.2A*).

To independently confirm our scaffolding of the putative 2.82 Mbp genome, Illumina MiSeq 2 x 250 libraries were constructed and sequenced using Illumina 2 × 250 sequencing reactions, and the resulting contigs were scaffolded using Lucigen NxSeq reactions. The resulting closed genome was identical to that produced by the hybrid HGAP-SSPACE assembly pipeline (*figure S.2B*).

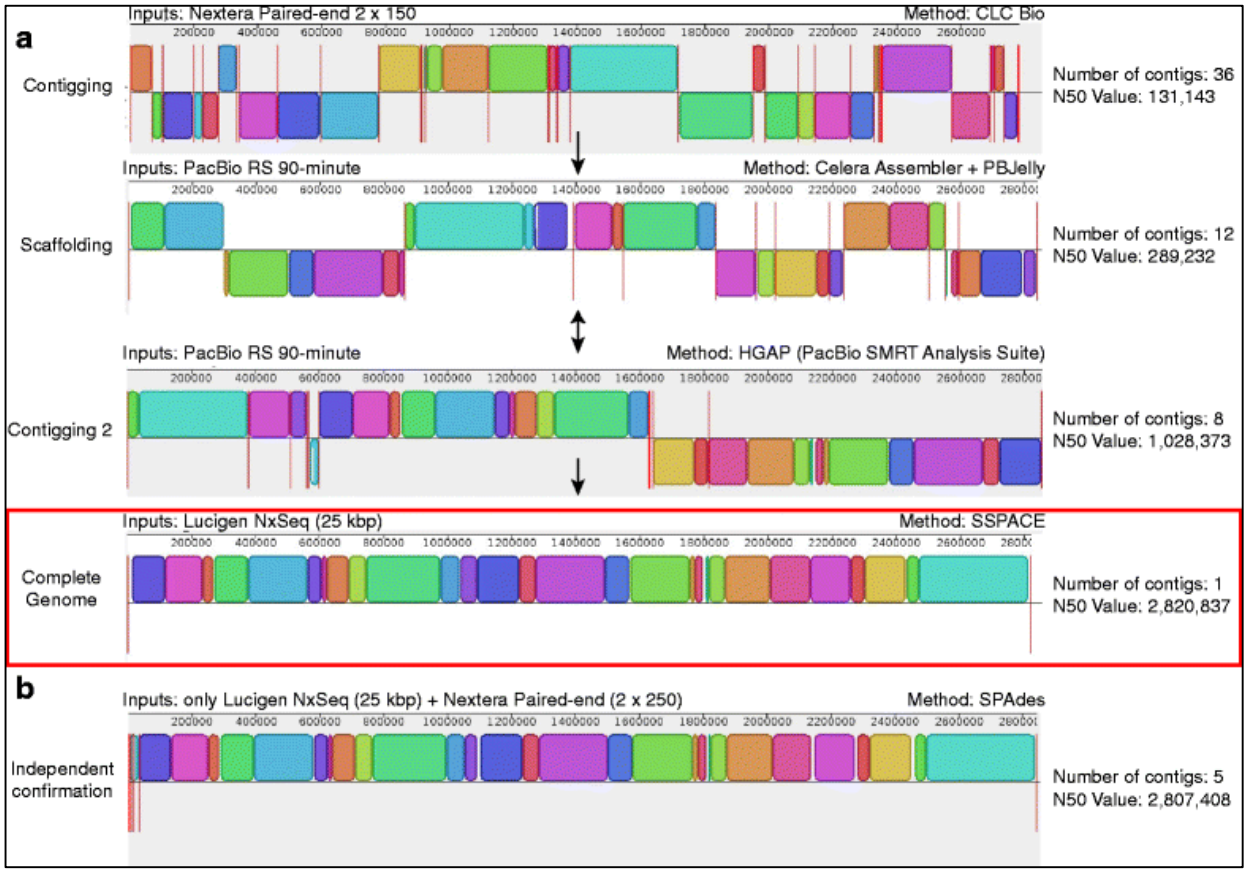

Figure S.2. Construction of the Tager 104 Genome. **a** The Tager 104 genome was constructed using indicated methods, with each step incorporating new genomic data (Inputs). First, Tager 104 paired-end reads from Illumina MiSeq sequencing were submitted to CLC Bio (Contigging). Resulting contigs were scaffolded using reads from PacBio RS sequencing (Scaffolding). Due to the inability to further close scaffolds, PacBio RS data alone was instead contigged using HGAP assembly (Contigging 2). The eight remaining contigs were then closed using Lucigen NxSeq mate-pair libraries with the SSPACE algorithm. Single-headed arrows represent events where resulting data from the previous step was submitted to algorithms in the subsequent step (Method). Steps in which results were interchangeable are indicated by two-headed arrows. The assembly is described in more detail in "Methods." **b** In order to confirm the completed genome, Lucigen NxSeq libraries were submitted with separate 2 × 250 paired-end reads in an independent SPAdes construction devoid of previous read data from panel A. Results were identical to the finished genome.

Repeat Regions Created Difficulty in Automated Closure

To determine the shortcomings of individual methods on the closing of the Tager 104 genome, as a model for future *S. aureus* genome assembly, each contig or scaffold was mapped to the final genome using Nucmer and visualized using Circos (*figure S.3*). In addition, repeats were determined by mapping the Tager genome to itself and selecting for matches with unique locations and a size > 500 bp. Interspersed repeats and RNA sequences were determined using the RepeatMasker algorithm. Based on the analysis, Illumina MiSeq 2 × 150 reads did not properly bridge areas of the genome that were rich in repeats. More specifically, repeats > 500 bp (*figure S.3*, Region 1) and RNA repeats (*figure S.3*, Region 2) caused the greatest issues in construction, as visualized. In addition, PacBio RS coverage was low across these areas. Therefore, information provided by the Lucigen NxSeq sequencing reactions was essential for the proper untangling and assignment of these genomic regions.

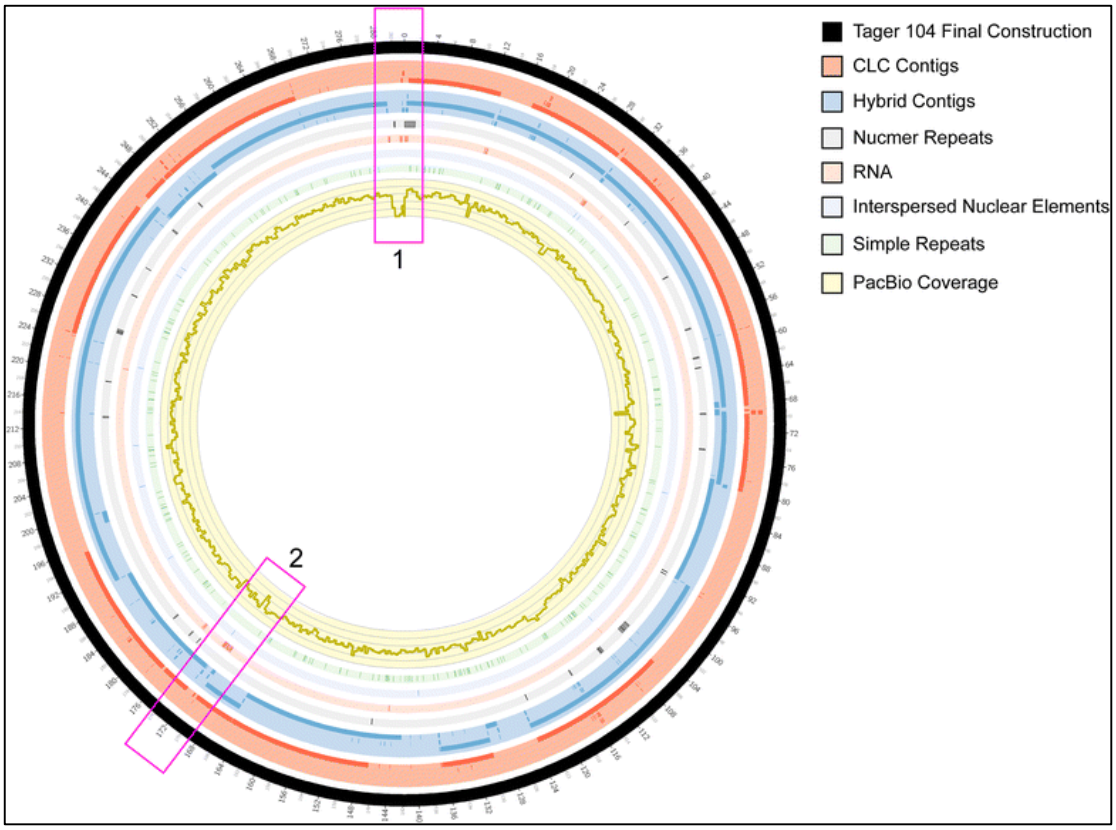

Figure S.3. Graphical Depiction of Tager 104 Assembly. The Tager 104 genome was scaffolded using three separate technologies: contigs from MiSeq reactions (red tiling), PacBio RS reads (yellow histogram), and scaffolds produced from the hybrid assembly of both (blue tiling). However, assembly of the Tager 104 genome using these technologies were found insufficient alone, due to the presence of repeat regions. More specifically, long repeats (>500 bp) create errors in de Bruijn graph untangling (gray tiling). In addition, the exact placement of short repeats, such as interspersed nuclear elements (light blue tiling), RNA sequences (light red tiling) and simple repeats (light green tiling) create errors in construction. Areas rich in repeats and low in sequencing coverage (Regions 1 and 2) reveal difficulties in genomic construction. These difficulties were overcome by providing the construction algorithms with 20 kbp mate-pair information, provided by Lucigen NxSeq libraries.

Proteomic Analysis of S. aureus Reference Sequences

Delineation of the *S. aureus* strains is typically achieved using the MLST analysis. Briefly, the analysis utilizes sequence heterogeneity among seven housekeeping genes to provide a higher resolution phylogenetic analysis. Reference genomes were obtained from the GenBank RefSeq database (*Table S.I*). MLST and *spa* typing of *S. aureus* Tager 104 previously revealed it to be ST49, the predicted founder of clonal complex 49 (CC49) [144]. CC49 was also shown to contain ST138, ST1693, ST1937, and ST2273 based on eBurst analysis (data not shown) [170].

To determine the similarities of protein content in completed sequences of *S. aureus*, each genome was called for open reading frames using the prodigalrunner algorithm and compared using the blastmatrix algorithm on CMG-Biotools version 2.2. The results shown in *figure S.4* indicate that the Tager 104 proteome is most closely related to Newman, a strain isolated in 1952 from a human patient and which has been well characterized for its coagulase activity. Similarity in these genomes supports the previously observed similarity in endocarditis models [69]. Following this strain, Tager 104 was > 84% similar to the nosocomial MRSA strain 04-02981, community-acquired MRSA strain SA268, and the human pleural isolate DSM 20231. The greatest proteomic differences were seen for strain ST398, a typically ovine-associated strain isolated from a human case of endocarditis, which was also the second-largest proteomic divergence observed [101].

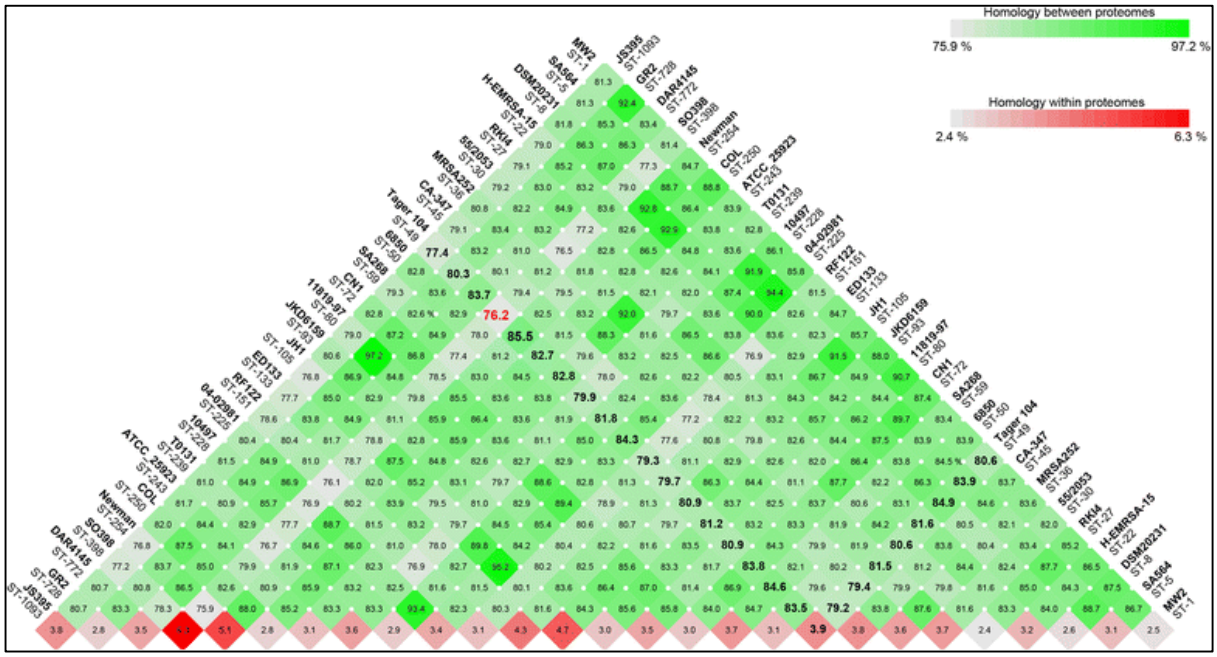

Figure S.4. Proteomic Analysis of *S. aureus* Genomes. One *S. aureus* reference sequence GenBank files from each ST group of the completed genomes as of Oct. 2015 were downloaded from the NCBI server and genes were called using the prodigalrunner algorithm on a CMG-Biotools system. The names of the strains are listed with corresponding ST numbers below. Most relevant here, the comparisons to our Tager 104 genome are shown in bold with the highest protein similarity (blue) and lowest similarity also shown. Percent paralogs within a given genome are shown at the base of the blast matrix and correspond to the red heat map.

Tager 104 is an ancestor to clinical isolates

To determine the lineage of *S. aureus* reference strains in relation to Tager 104, genomes were submitted to Mauve alignment and conserved segments were stripped and concatenated for each genome for phylogenetic analysis by RAxML. This alignment and phylogeny used only core genomic regions present in all 75 *S. aureus* strains available as of Oct. 1st 2015.

The resulting tree (*figure S.5* and *supplemental figure S.I*) shows Tager 104 to be the earliest branching member of a clade containing strain 6840, M013, SA40, SA268, SA957, ED133, and RF122. Strain 6840 was isolated from a skin abscess at the University of Wisconsin in 1987, and was shown to progress from the abscess to systemic complications, such as systemic abscesses and septic arthritis. This supports Tager 104 as a reference sequence for systemically-penetrating bacteria [171]. As a positive control, 2 separate genome dataset corresponding to COL and NRS100 were also used and there is indication that these strains are the same or closely related. The results of our analysis are consistent with this hypothesis.

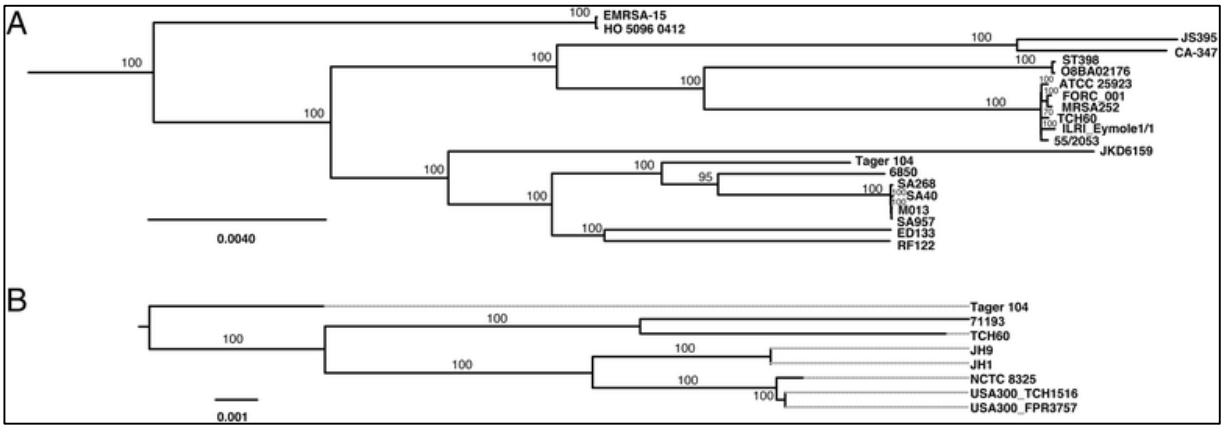

Figure S.5. Whole-Genome Phylogenetic Analysis of *S. aureus* Reference Strains. Proximal branches nearest Tager 104 are shown for the phylogenetic analysis of all S. aureus reference strains whose genome were available by Oct. 2015 (**a**) or isolates from the United States (**b**) based on Mauve alignment and RAxML analysis. For a complete tree of all strains, please refer to Additional file 2: Figure S.I. Bootstrap values represent the result of 100 trials.

Tager 104 Contains a Limited Set of MGE-encoded Virulence Factors Targeted at Host Immunity

As Tager 104 was able to survive in septic murine models, and due to its phylogenetic placement as an ancestral *S. aureus* lineage, we investigated the genomic content of MGE-encoded virulence factors that have been previously identified and characterized [147]. The results demonstrate a limited set of encoded factors in the Tager 104 genome that are predicted to be necessary for bacterial survival during bacteremia (*figure S.6A*). In addition, BRIG analysis revealed similar genomic regions between strains of the Tager clade (*figure S.6B*).

Tager 104 is predicted to encode a νSaα-encoded Staphylococcal super-antigen-like SSL, as well as νSaβ-encoded leukotoxin D and E (*lukD* and *lukE*, respectively). These factors are known to inhibit elements of innate immunity [172]. The νSaβ-island was also shown to contain the hyaluronate lyase gene (*hysA*), which degrades hyaluronic acid found in host extracellular matrix.

The Tager 104 genome also indicates early exposure to phage-carried virulence factors. Tager 104 contained the Staphylococcal inhibitor of complement (*scn*), which targets innate immunity by inhibiting phagocytosis by neutrophils. Tager 104 was shown to contain the *hlb*-interrupting phage described in the genomes of modern clinical strains, such as N315, Mu50, MW2, NCTC8325, MSSA476, MRSA252, USA300, JH1, JH9, and Newman [9], and was defined here as φTGR1. Interestingly, Tager 104 also contains the PVL cassette (*lukF-PV* and *lukS-PV*), a phage-transferred pore-forming leukocyte toxin linked to necrotic infections. Tager 104 only contains one enterotoxin, determined by BLAST analysis as an exact match to the phage-transferred enterotoxin P [147]. PVL-positive *S. aureus* strains are certainly in the minority of the totality of *S. aureus* genomes sequenced to date, but some notable strains include ST1 strains

(MW2 and USA400), ST8 strains (NCTC 8325, TW20, USA300, and USA500), and ST239 (TW20).

In addition, Tager 104 was determined to contain one unknown prophage and four unknown genomic islands, indicated as φTGR2 and TGR1 through TGR4, respectively. The contents of these islands were limited to hypothetical and/or phage proteins (*table S.II*).

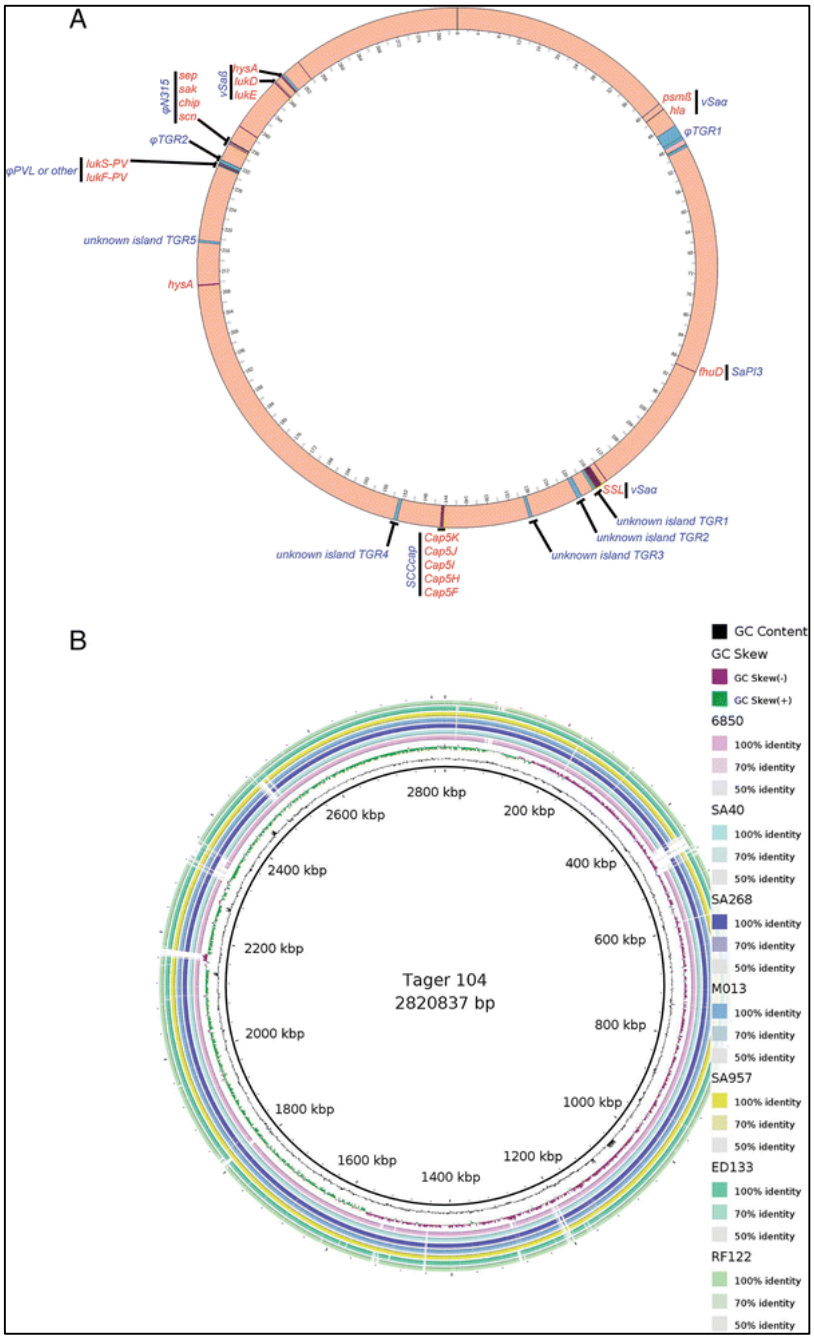

Figure S.6. Mobile Genetic Element-Encoded Virulence in *S. aureus* Tager 104. (**A)** Mobile genetic element (MGE)-encoded genes relevant for virulence in *S. aureus* were selected based on prior knowledge of *S. aureus* genomics. Those elements detected by BLAST analysis in the Tager 104 genome are indicated by locus (red bands) as well as gene name (red labels), and the genomic island responsible for carrying these elements are grouped (black bar) and indicated beside the gene name (blue label). In addition, islands were detected using the IslandViewer 3 software, and are indicated by locus (blue bands) and given identifiers (blue label) based on gene identities and BLAST result. (**B)** Blast ring analysis of loci from strains in the Tager 104 clade. Tager 104 GC content and GC skew are represented on the innermost ring, with percent identity reported for genomes in the Tager 104 clade reported on the outermost rings as indicated.

Tager 104 Shows Intermediate Clinical Adaptations

One group of pathogenicity islands that are non-phage and non-SCC genomic islands are termed νSa islands, and typically contain a combination of virulence factors and either an intact or remnant recombinase [9]. Two such islands, termed νSAα and νSAβ, were previously found to be allelic, and are therefore typed and used in conjunction with sequence type analysis for determination of strain radiation. Comparison between the profiles of the νSAβ genomic island for one community-acquired MRSA (CA-MRSA) strain (COL), three hospital-acquired MRSA (HA-MRSA) strains (MRSA252, Mu3, JH1), and two ruminant host MSSA strains (S0385, RF122), as well as Tager 104 demonstrated that *S. aureus* Tager 104 has lost the majority of the *bsa* locus, with the exception of *bsaG* (*figure S.7*). However, *S. aureus* Tager 104 has not acquired enterotoxin genes seen in other strains adapted for the hospital setting (HA-MRSA). The loss of this *bsa* locus, coupled with the gain of enterotoxins has been previously hypothesized to indicate a shift from the environmental niche to one of hospital acquisition [173]. Therefore, *S. aureus* Tager 104 may represent an intermediate strain for the selection of this νSAβ profile in the hospital setting.

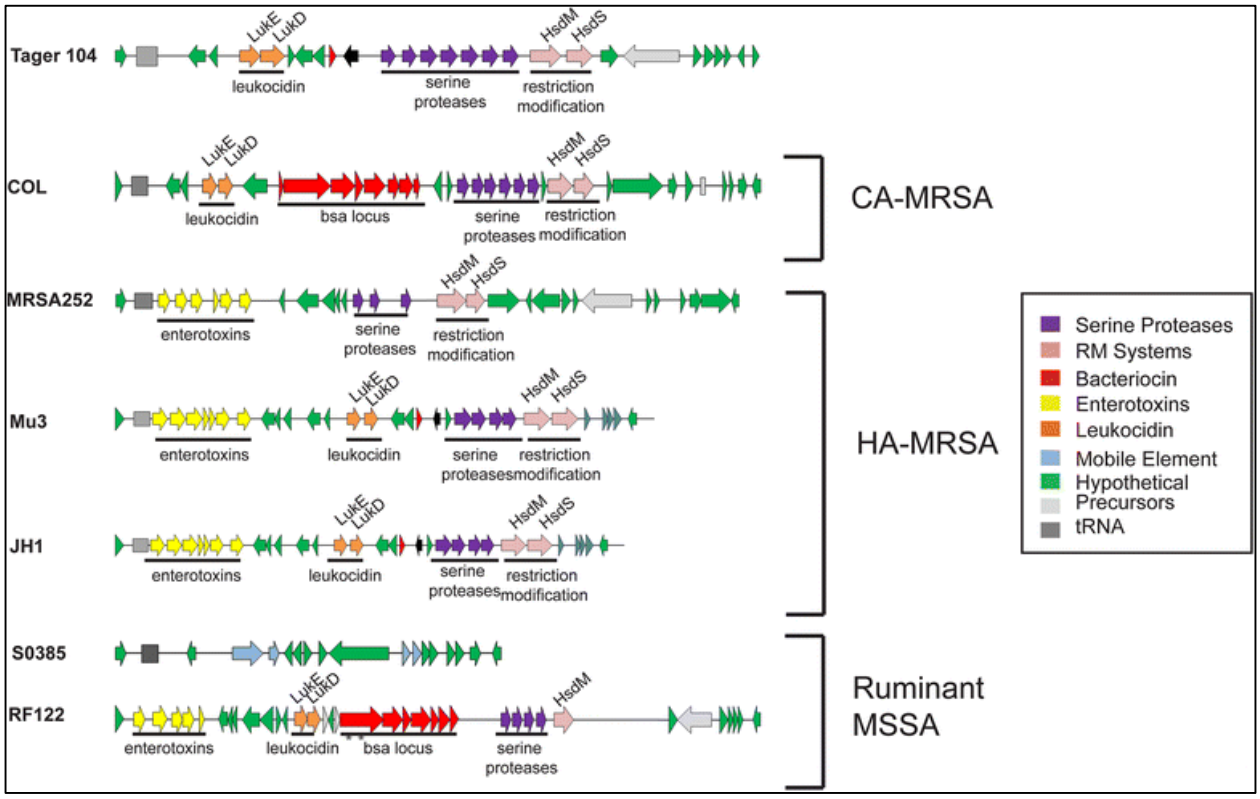

Figure S.7. Tager 104 νSaβ Genomic Island Shows Intermediate Clinical Adaptation. Representatives from each subtype of the νSaβ locus were selected and compared using the RAST server. Current strains of community acquired MRSA (CA-MRSA) contain the bsa locus (red arrows), which encodes a bacterial antibiotic. In contrast, hospital-acquired MRSA (HA-MRSA) have lost the bsa locus and instead gained enterotoxins (yellow arrows), an adaptation which has been previously associated with a selection for hospital settings. Results indicate Tager 104 has lost the bsa locus, but lacks the enterotoxin cluster (yellow) that has also been associated with this shift. In contrast, ruminant-host MSSA shows a wide range of these genotypes

S. aureus Tager 104 Antibiotic Resistance Profile

To determine the potential of Tager 104 for the future study of acquired antibiotic resistance, known MGE-transferred resistance cassettes [147] were searched against the completed genome using BLAST. No resistance elements were detected (data not shown).

Minimum inhibitory concentrations (MIC) for *S. aureus* Tager 104 were determined by challenging with E-test strips for linezolid, vancomycin, erythromycin, and oxacillin. MICs for antibiotics were determined by E-test strip analysis and *S. aureus* Tager 104 demonstrated resistance to LZ at 1 μg/mL, VA at 2-3 μg/mL, ER at 0.064 μg/mL, and OX at 0.019 μg/mL (*figure S.8*). The vancomycin-intermediate susceptibility phenotype of *S. aureus* Tager 104 was confirmed by a solution-based test in a 96-well format; results confirm the MIC to be about 3 μg/mL. *S. aureus* Tager 104 colonies on brain-heart agar plates are well-formed with the absence of satellite projections that would denote the presence of small colony variants and an overall white color, which is unlike other vancomycin-intermediate strains described previously [174].

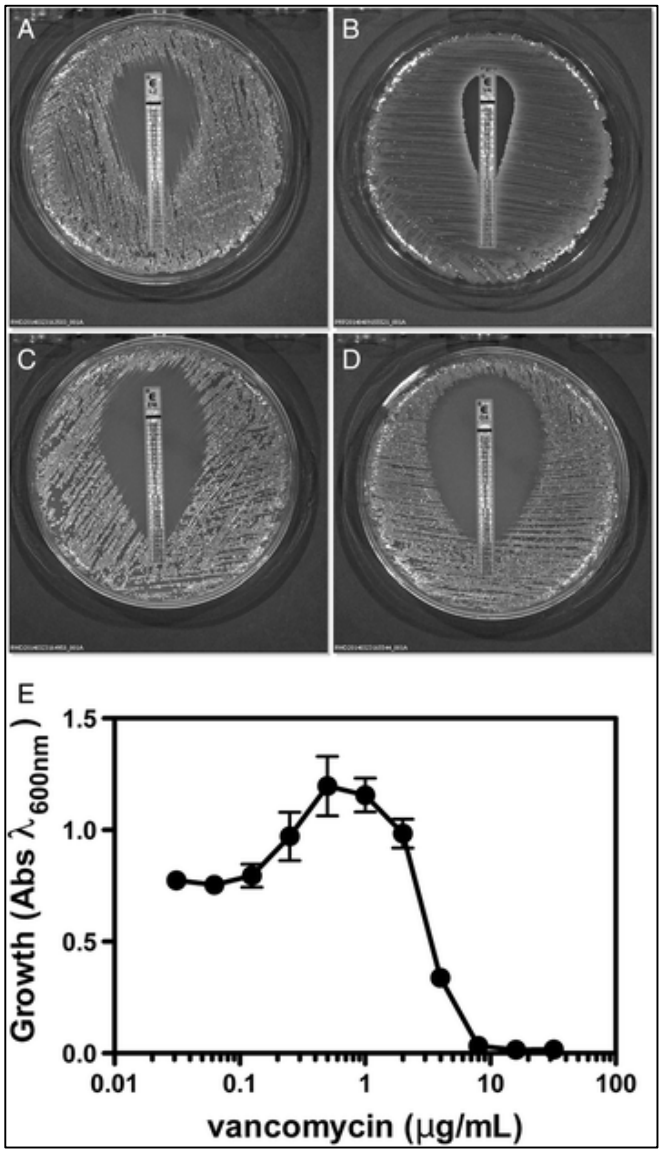

Figure S.8. *S. aureus* Tager 104 Susceptibility to Antibiotic Therapy Demonstrates Predation of Resistance Development. **a**–**d** Antibiotic susceptibility testing on sheep blood agar (SBA) plates demonstrated S. aureus Tager 104 is susceptible to linezolid (**a**), vancomycin (**b**), erythromycin (**c**), and oxacillin (**d**) when challenged with E-test strips. Minimum Inhibitory concentrations shown are: linezolid, 1 μg/mL; vancomycin, 2–3 μg/mL; erythromycin, 0.064 μg/mL; and oxacillin, 0.019 μg/mL. **e** The effects of vancomycin concentrations on Tager 104 growth were confirmed in solution in 96-well plates and indicate a vancomycin intermediate susceptibility phenotype. This experiment is a combination of 8 replicates and was performed as described in "Methods".

Discussion

S. aureus infections range in presentation from localized skin infections to more life-threatening osteomyelitis, endocarditis and sepsis. With the advent of next-generation sequencing, analysis is now possible for individual genomes across the spectrum of infections. These data revealed that certain *S. aureus* strains exhibit considerable changes in their gene make-up thus, reflecting selective pressure to infect a certain host preferentially [11]. The acquisition of MGE and smaller changes in genes known as nucleotide polymorphisms together confer the apparent selective advantages needed for these strains to survive in a given host. The capacity for lateral gene transfer in *S. aureus* strains fuels this potential for rapid adaptation. For example, *S. aureus* Newman, isolated in 1952, has been shown to contain four prophages (φNM1–φNM4) and one additional νSa island, νSa4 [9]. The lack of these prophages was associated with decreased abscess formation in organs. However, a strain such as MW2 lack these prophages, but was isolated from a patient with abscesses of the brain, heart, liver, and kidneys, leading to death [175], [148]. Therefore, the required machinery for a particular infection is highly model-specific, and we suggest that reference strains should be limited in scope to those which suffice for a particular infection model.

Our previous results [176], suggested that *S. aureus* Tager 104 is a potent strain for the formation of bacterial endocarditis, a serious complication of bacteremia. This may not be surprising considering Tager 104 was originally isolated and maintained for decades, due in no small part for its potent ability to form stable clots in human, rabbit, and sheep blood [177]. This clotting phenotype has been attributed to the coordinated effort of two non-proteolytic activators of prothrombin, namely staphylocoagulase [8] and von Willebrand factor binding protein [112, 113]. Both of these factors activate prothrombin by forming a reversible complex that cleaves their

substrate fibrinogen to provide the fibrin barrier, similar to those seen here in the focal abscesses in multiple organs, including the kidney and spleen, that were formed by simple induction of the infection by diffuse bacteremia (*figure S.1*). Because of these observations, and the early date of its isolation, we sought to outline Tager 104 as a reference strain for the systemic infection niche. We therefore determined the phylogenetic relationship of Tager 104 for future evolutionary and correlation studies compared to other *S. aureus* strains.

Our goal in genome sequencing was to find the simplest and most inexpensive combination of technologies to complete the Tager 104 genome so that it may be used as a reference for future *S. aureus* genomic comparisons. We began with Illumina MiSeq 2 × 150 paired-end libraries, constructed using a Nextera kit. To close the genome, literature suggested that the use of PacBio RS technology would enable bridging across complex regions using longer reads [178]. PacBio reads were corrected using Illumina MiSeq paired-end reads, and scaffolded to create the final genomic construction. The result from this "hybrid assembly" was twelve scaffolds, which have been previously described [144]. However, no combination of algorithms or manual assembly were able to close the genome. New advancements in PacBio construction, ushered by the release of the newer HGAP assembly algorithm, led us instead to reconstruct the genome using raw PacBio data alone, producing 8 scaffolds of varied sizes, which similarly did not result in a complete genome and bridging these contigs manually proved problematic. We therefore decided to approach the closing of the genome using greater distances between the paired reads, to provide additional information to the construction algorithms. Two Lucigen 20 kb mate-pair libraries were sufficient to close the Tager 104 genome from this HGAP-assembled data. Furthermore, Illumina 2 x 250 paired-end libraries were constructed, sequenced, and assembled *de novo*. Upon addition of the Lucigen mate-pair libraries, the final genome was produced. Therefore, the aforementioned

Lucigen mate-pair library could be used to independently assemble the Tager 104 MiSeq 2 × 250 bp reads. This provides a proof of principle to guide a streamlined protocol for assembly.

To interpret this *S. aureus* Tager 104 genomic dataset in the auspices of the systemic niche, it will need to have the following characteristics: (1) it will be a clinical sample, (2) be an early branching member of the *S. aureus* phylogenetic tree, and (3) be limited in MGE content to those which are necessary for systemic survival (*i.e.*, immune system evasion). Based on the results of these analyses, Tager 104 has been found to have all of these characteristics. Tager 104 has been maintained from primary freezer stocks since its isolation in the late 1940's. Tager 104 shows ancestral phylogeny similar to other methicillin-resistant and methicillin-susceptible strains that have been characterized in the literature [179]. This clade is made up of two systemic isolates (6840 and SA957), one wound isolate (M013), one nasopharygenal isolate (SA40), and two ruminant isolates (ED133 and RF122). Interestingly, SA957 occurs later in the lineage than SA40 and has been associated with more severe septic infections and higher mortality rates [180]. This differentiation was hypothesized to be due to the loss of the β-hemolysin-interrupting phage.

Tager 104 shows a limited set of MGE content primarily focused on the evasion of host innate immunity. Tager 104 was shown to contain the *hlb*-interrupting phage described above, labeled as φTGR1, as well as two additional phages. One of these phages contained PVL, indicating the earliest acquisition of this factor in the literature. The other phage was shown to carry no additional genes aside from those necessary for phage construction and replication (*table S.II*). For comparison, prophage φTGR1 and φTGR2 were compared proteomically using BLAST matrix analysis with complete phage genomes downloaded from the GenBank server, and showed low homology to three phage genomes (*Supplemental Figure S.II*). In addition, Tager 104 was shown to contain the νSaα and νSaβ islands, found in all *S. aureus* genomes [9]. Although Tager

104 was also detected to contain four additional potential genomic islands, their gene content consisted solely of hypothetical proteins. Therefore, the virulence-associated genomic island composition of Tager 104 is limited to those which are found in all genomes (νSaα, νSaβ), the *hlb*-interrupting phage found in most all human or animal pathogenic *S. aureus* (φTGR1), and the PVL-carrying phage strains.

The *S. aureus* Tager 104 genome also indicates that this strain pre-dates the acquisition of the SCC*mec* cassette and may serve to bridge certain clinical MRSA and MSSA strains (*figure S.5* and *supplemental figure S.1*). Supportive to this hypothesis is the recent observation of an ST49-t208 strain that has become methicillin-resistant [181], potentially through the acquisition of the *mecALGA251* cassette [182]. These results indicate that Tager 104 represents an intermediate departure in the evolution of multi-drug resistant *S. aureus*. Antibiotic susceptibility of *S. aureus* Tager 104 presented here using clinically approved E-test analysis corroborates genomic data (*figure S.8*) and indicates that Tager 104 displays a borderline vancomycin intermediate *S. aureus* phenotype (*figure 8B* and *8E*). In fact, current vancomycin guidelines would prohibit use of vancomycin in patients where the isolated strain MIC for vancomycin is equal to or over 2 μg/mL making any potential enhancement to vancomycin resistance or small colony variant formation by Tager 104 could be of significant importance to the understanding of acquired *S. aureus* resistance.

Interestingly, Tager 104 also shows an intermediate adaptation to the nosocomial environment. Tager 104 proteome analysis (*figure S.4*) showed an equivalent homology to both community acquired strain SA268 (84.6 %) and nosocomial strain 04-02981 (84.3%). Therefore, we investigated further the νSaβ genomic island, which has been previously implicated in the shift to hospital settings. Our analysis (*figure S.7*) revealed that Tager 104 has lost the genes necessary

for competition for resources in the environment, but had yet to gain those necessary for spread in a clinical setting at its time of isolation.

It has been recently suggested that the acquisition of these MGEs may be driven by "glycocodes" encoded by the teichoic acid structure of *S. aureus*, as these structures are recognized by bacteriophages during transduction events [183]. With this in mind, we investigated the locus of teichoic acid biosynthesis in *S. aureus* Tager 104, COL (as a representative of early MRSA strains) and JH1 (as a representative of early VRSA strains) with the hypothesis that homology in these strains indicate a potential phage-mediated acquisition of MGEs. The results indicate that the genomic makeup of this biosynthesis cluster is identical in these three strains (Supplemental *figure S.3*). Therefore, a strain ancestral to Tager 104 acquired resistance elements from bacteriophages leading to the evolution of more recent clinical MRSA and VRSA strains, in agreement with this phylogenetic analysis (*figure S.5* and *supplemental figure S.1*). As expected, the PS187 genome described previously showed a very distinct profile, furthering the previous conclusion that this strain is distantly related to other known *S. aureus* lineages. Further analysis will be required to investigate the origin of resistance transfer into Tager 104 and its contribution to *S. aureus* virulence.

Identification of a sufficient reference for systemic pathogenesis by *S. aureus* and acquisition of multi-drug resistance are crucial to give context and scope to single nucleotide polymorphisms present in modern *S. aureus* isolates that may provide adaptive advantages to these strains *in vivo*. Within, we have demonstrated that Tager 104 displays a virulent phenotype during infections *in vivo*. Phylogenetic analysis, as well as a set of MGE-encoded factors limited to that which is necessary for systemic survival, suggest that Tager 104 can be used as a reference strain for future studies of *S. aureus* systemic virulence.

Availability of Supporting Data

The complete Tager 104 genome is available on GenBank as accession number CP012409. Previous scaffolds mentioned in the text may be found on GenBank as accession number AVBR00000001. Phylogenetic data is available at the following URL: http://purl.org/phylo/treebase/phylows/study/TB2:S18780.

Abbreviations

S. aureus: Staphylococcus aureus; MGE: Mobile Genetic Elements; SCCmec: Staphylococcal Cassette Chromosome *mec*; PVL: Panton-Valentine Leukocidin; MSSA: Methicillin-Sensitive *S. aureus*; MRSA: Methicillin-Resistant *S. aureus*; VRSA: Vancomycin-Resistant *S. aureus*; BHI: Brain-Heart Infusion; PBS: Phosphate Buffered Saline; O.D.: Optical Density, OCT: Optimal Cutting Temperature; H&E: Hematoxylin and Eosin; HGAP: Hierarchical Genome Assembly Process; SSPACE: SSAKE-based Scaffolding of Pre-Assembled Contigs after Extension; BLAST: Basic Local Alignment Search Tool; RAST: Rapid Annotated using Subsystem Technology; SPAdes: St. Petersburg genome Assembler; MLST: Multi-Locus Sequence Typing; ST: Sequence Type; LCB: Locally Collinear Blocks; CIPRES: Cyberinfrastructure for Phylogenetic Research; PEG: Protein-Encoding Gene; BRIG: BLAST Ring Image Generator; TSA: Trypticase Soy Agar; ER: Erythromycin; LZ: Linezolid; OX: Oxacillin; VA: Vancomycin; CA-MRSA: Community Acquired MRSA; HA-MRSA: Hospital Acquired MRSA; MIC: Minimum Inhibitory Concentration.

Competing Interests

The authors report no competing interests.

Authors Contribution

RD, MN, PEB, MRL, DM, and PP drafted the manuscript. RD carried out genomic construction and characterization. ADB carried out MLST analysis and aided in tree construction. PP, MRL, and MJH participated in the design of the study. SM, ML and DM constructed the Lucigen NxSeq libraries and sequenced these libraries, as well as aiding in the design of genomic construction. All authors read and approved the final manuscript.

Acknowledgements

Supported by the National Institutes of Health through grants provided by the National Heart, Lung, and Blood Institute, R00HL094533 (to P.P.), R01HL114477 (to P.P. and M.N.), R01 HL071544 (to P.E.B). Support also provided by the National Institute of Allergy and Infectious Diseases grant 2R44AI085840-02 (to D.M., P.P. and M.R.L.). The authors also wish to thank the Alabama Supercomputer Authority for access to the Alabama Supercomputer.

Table S.I: Bacterial Strains Used In This Study:

Strain	Date	Location	Host	Infection	ST	References
04-02981	2004	Germany	Human	Not provided	225	[184]
08BA02176	2008	Canada	Human	Wound	398	[140]
11819-97	1997	Denmark	Human	Skin	80	[185]
2395_USA500	1994	USA	Human	Wound	8	[179, 186]
502A	1963	USA	Human	Nasal	5	[187]
55/2053	N/A	N/A	N/A	N/A	30	Unpublished
6850	1987	USA	Human	Skin abscess	50	[188]
71193	2004	USA	Human	Colonization		[189, 190]
ATCC 25923	1945	USA	Human	Not provided	243	[191]
BAA1680_25b_MRSA	2003	USA	Human	Skin	8	[192]
BAA1680_26b_MRSA	2003	USA	Human	Skin	8	[192]
BAA1680_27b_MRSA	2015	Laboratory	N/A	N/A	8	[192]
BAA1680_29b_MRSA	2015	Laboratory	N/A	N/A	8	[192]
BAA1680_31b_MRSA	2015	Laboratory	N/A	N/A	8	[192]
BAA1680_33b	2015	Laboratory	N/A	N/A	8	[192]
Bmb9393	1993	Brazil	Human	Bloodstream	239	[193]
CA-15	2007	Colombia	Human	Not provided	8*	[194]
CA-347	2005	USA	Human	Bloodstream	45	[195]
CN1	2006	South Korea	Human	Necrotizing fasciitis	72	[180]
COL	1960	UK	Human	Surgical	250	[196]
DSM 20231	1884	Germany	Human	Pleural fluid	8	[197]
ECT-R2	2004	Sweden	Human	Not provided	5	[198]
ED133	1997	France	Ovine	Mastitis	133	[100, 199]
E-MRSA-15	N/A	UK	Human	Bloodstream	22	[200]
FCFHV36	2015	Brazil	Human	Bone	105	[201]
FORC_001	N/A	South Korea	N/A	N/A (soy bean)	30	[202]
GR2	2006	Greece	Human	Nasal	728*	[203]
Gv69	N/A	N/A	N/A	N/A	239	Unpublished
HO 5096 0412	2005	UK	Human	Neonatal	22	[204]
HOU1444-VR	2012	Brazil	Human	Bloodstream	5	[205]
ILRI_Eymole1/1	N/A	N/A	N/A	N/A	30	Unpublished
JH1	2001	United States	Human	Bloodstream	105	[206]
JH9	2001	United States	Human	Bloodstream	105	[206]
JKD6008	2003	New Zealand	Human	Bloodstream	239	[207]
JKD6159	2004	Australia	Human	Sepsis	93	[208]
JS395	N/A	N/A	N/A	N/A	1093	Unpublished
M013	2002	Taiwan	Human	Wound	59	[209]
M121	2006	Colombia	Not provided	Not provided	8	[194]
MRSA252	1997	UK	Human	Sepsis	36	[210]
MSHR1132	2006	Australia	Human	Necrotizing fasciitis		[211]
MSSA476	1998	UK	Human	Bone	1	[210]
Mu3	1996	Japan	Human	Pneumonia	5	[212, 213]
Mu50	1997	Japan	Human	Surgical	5	[152]
MW2	1998	USA	Human	Septicemia	1	[148]

N315	1982	Japan	Human	Throat	5	[152]
NCTC8325	1960	UK	Human	Conjunctiva	8	[214]
Newman	1954	UK	Human	Osteomyelitis	254	[9]
NRS 100	1960	UK	Human	Surgical	250	Unpublished
RF122	1993	Ireland	Bovine	Mastitis	151	[11, 215]
RKI4	2008	Germany	Human	Gastric	27	[216]
S0385	2006	Netherlands	Human	Endocarditis	395**	[101]
SA268	2012	China	Human	Sepsis	59	[217]
SA40	2005	Taiwan	Human	Nasal	59*	[180]
SA564	2013	Switzerland	Human	Bloodstream	5	[218]
SA957	2000	Taiwan	Human	Bloodstream	59	[180]
ST228_10388	2001	Switzerland	Human	Not provided	228	[219]
ST228_10497	2001	Switzerland	Human	Not provided	228	[219]
ST228_15532	2006	Switzerland	Human	Not provided	228	[219]
ST228_16035	2006	Switzerland	Human	Not provided	228	[219]
ST228_16125	2006	Switzerland	Human	Not provided	228	[219]
ST228_18341	2008	Switzerland	Human	Not provided	228	[219]
ST228_18412	2008	Switzerland	Human	Not provided	228	[219]
ST228_18583	2008	Switzerland	Human	Not provided	228	[219]
DAR4145	2009	India	Human	Abscess	772	[220, 221]
T0131	2006	China	Human	Not provided	239	[222]
Tager 104	1947	USA	Human	Impetigo	49	This paper
TCH60	2008	USA	Human	Skin	30*	ATCC
TW20	2003	UK	Human	Bacteremia	239	[223]
UA-S391_USA300	N/A	USA	N/A	N/A	8	[200]
USA300_2014.C01	2014	USA	Human	Wound	8	[224]
USA300_2014.C02	2014	USA	Human	Wound	8	[224]
USA300_FPR3757	2004	USA	Human	Abscess	8	[151, 225]
USA300_TCH1516	2004	USA	Human	Bacteremia	8	[226, 227]
USA300-ISMMS1	2014	USA	Human	Bacteremia	8	[106]
VC40	2002	Laboratory	N/A	N/A	8	[228]
Z172	2010	Taiwan	Human	Bacteremia	239	[229]

**denotes strain genomes was completed by Oct. 2015 but ST was not determined by automated CLC software.*

***denoted strain genomes was not completed by Oct. 2015 and ST was not determined by automated CLC software.*

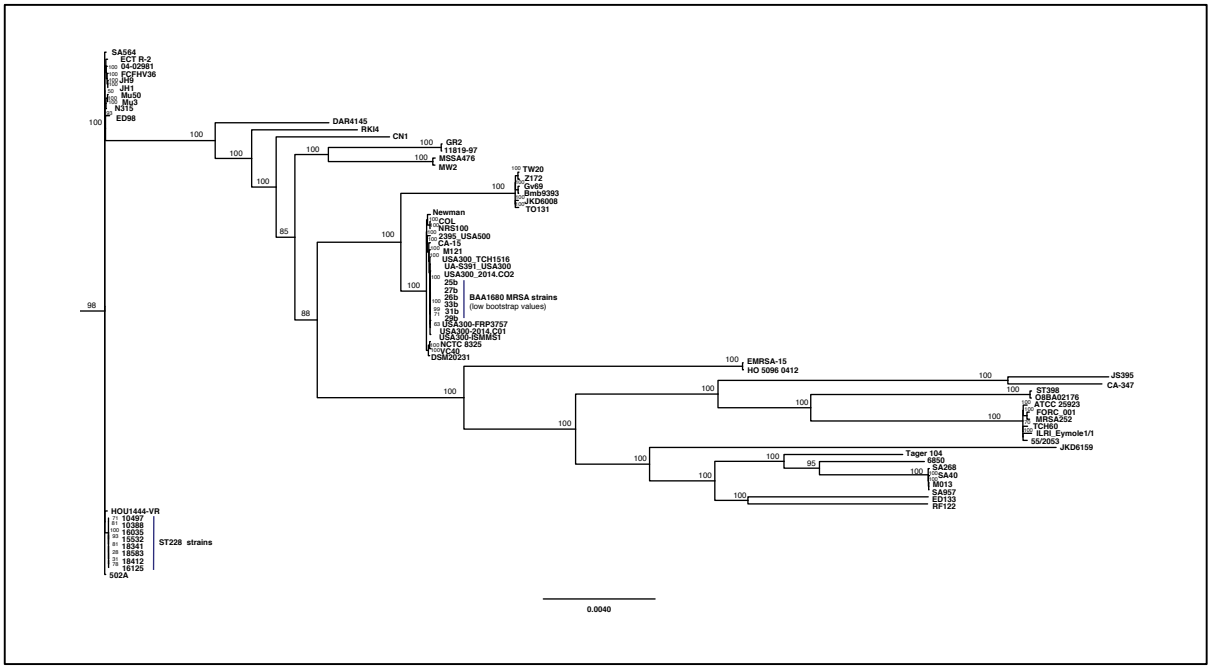

Figure S.I. Complete Phylogenetic Tree of *S. aureus* Reference Strains. Whole-genome phylogenetic analysis of all *S. aureus* reference strains from Fig. 5. Related branches, such as BAA1680 and the eight ST228 strains had lower bootstrap values, as would be expected given their derivations and regional isolation, respectively. Bootstrap values represent the result of 100 trials. (PDF 180 kb).

For high resolution download, see the following webpage:
https://static-content.springer.com/esm/art%3A10.1186%2Fs12864-016-2433-8/MediaObjects/12864_2016_2433_MOESM1_ESM.docx

Table S.II: Genomic Islands and Prophages in the Tager 104 Genome:

Genomic Location	Name	BLAST Result	Gene Annotations
GENOMIC ISLANDS			
1,165,336 - 1,170,248	TGR1	SA268, SA40, SA957, M013	ORF031
			ORF021
			Phage lysin, N-acetylmuramoyl-L-alanine amidase (EC 3.5.1.28)
			Phage holin
			Phage protein
			Tail fiber protein [SA bacteriophages 11, Mu50B]
			Phage lysin, N-acetylmuramoyl-L-alanine amidase (EC 3.5.1.28)
			Phage protein
			Hypothetical protein, phi-ETA orf58 homolog [SA bacteriophages 11, Mu50B]
			Phage protein
			FIG01108548: hypothetical protein
			Putative major teichoic acid biosynthesis protein C
			Phage minor structural protein
			phi 11 orf43 homolog [SA bacteriophages 11, Mu50B]
			Phage tail length tape-measure protein
			phi 11 orf41 homolog [SA bacteriophages 11, Mu50B]
			Phage protein
			Phage tail protein
			Phage protein
			Phage protein
			Phage protein
			Phage transcriptional terminator
			Phage major capsid protein
			Phage capsid and scaffold
1,192,427 - 1,201,074	TGR2	6850	FIG01108790: hypothetical protein
			FIG01108566: hypothetical protein
			FIG01107981: hypothetical protein
			Integrase, superantigen-encoding pathogenicity islands SaPI
			FIG01108853: hypothetical protein
			FIG01108840: hypothetical protein
			hypothetical protein
			hypothetical protein

			hypothetical protein
			hypothetical protein
			hypothetical protein
			hypothetical protein
			Putative terminase, superantigen-encoding pathogenicity islands SaPI
			Hypothetical SAV0799 homolog in superantigen-encoding pathogenicity islands SaPI
1,285,693 - 1,291,359	TGR3	SA40, SA957, M013	FIG01108751: hypothetical protein
			FIG01108312: hypothetical protein
			FIG01108876: hypothetical protein
			FIG01107881: hypothetical protein
			Lmo0069 homolog within ESAT-6 gene cluster
			Lmo0069 homolog within ESAT-6 gene cluster
			FIG01108656: hypothetical protein
			FIG01108452: hypothetical protein
			FtsK/SpoIIIE family protein, putative EssC component of Type VII secretion system
1,523,588 - 1,529,604	TGR4	SA957	acetyltransferase (GNAT) family protein
			HTH-type transcriptional regulator LrpC
			hypothetical protein
			hypothetical protein
			Bipolar DNA helicase HerA
			FIG036446: hypothetical protein
			hypothetical protein
2,170,899 - 2,174,905	TGR5	FORC_001, MRSA252	FIG01107943: hypothetical protein
			FIG01107943: hypothetical protein
			FIG01107943: hypothetical protein
			Transcriptional regulator, Cro/CI family protein transposon-related
			FIG01107943: hypothetical protein
			FIG01107943: hypothetical protein
			FIG01107943: hypothetical protein

PROPHAGES			
447,213 - 490,078	ϕTGR1	ϕNM1-4	ORF031
			ORF021
			Phage lysin, N-acetylmuramoyl-L-alanine amidase (EC 3.5.1.28)
			Phage holin
			Phage protein
			Tail fiber protein [SA bacteriophages 11, Mu50B]

	Phage lysin, N-acetylmuramoyl-L-alanine amidase (EC 3.5.1.28)
	Phage protein
	Hypothetical protein, phi-ETA orf58 homolog [SA bacteriophages 11, Mu50B]
	Phage protein
	FIG01108548: hypothetical protein
	Putative major teichoic acid biosynthesis protein C
	Phage minor structural protein
	phi 11 orf43 homolog [SA bacteriophages 11, Mu50B]
	Phage tail length tape-measure protein
	phi 11 orf41 homolog [SA bacteriophages 11, Mu50B]
	Phage protein
	Phage tail protein
	Phage protein
	Phage protein
	Phage protein
	Phage transcriptional terminator
	Phage major capsid protein
	Phage capsid and scaffold
	Phage protein
	Phage protein
	Phage portal protein
	Phage terminase, large subunit
	Phage terminase, small subunit
	Integrase regulator RinA
	Phage protein
	Transcriptional activator rinB, phage associated
	Hypothetical protein, SAV0877 homolog [SA bacteriophages 11, Mu50B]
	hypothetical protein
	ORF058
	Phage protein
	ORF077
	Phage antirepressor protein
	Cro-like repressor [SA bacteriophages 11, Mu50B]
	Phage repressor
	hypothetical protein within prophage
	Hypothetical protein, SAV0849 homolog [SA bacteriophages 11, Mu50B]
	Phage excisionase
	Phage DNA invertase

2,308,294 - 2,313,700	ϕPVL or other	Acetylornithine deacetylase (EC 3.5.1.16)
		Leukocidin LukS-PV
		Leukocidin LukF-PV
		Beta-hemolysin
		Phage integrase
2,313,771 - 2,320,128	ϕTGR2 ϕNM3	Phage integrase
		Phage protein
		glycosyl transferase
		hypothetical protein within prophage
		Phage protein
		DNA helicase, phage-associated
		Phage repressor
		DNA-binding protein, phage associated
		hypothetical protein within prophage
		hypothetical protein within prophage
		Phage antirepressor protein

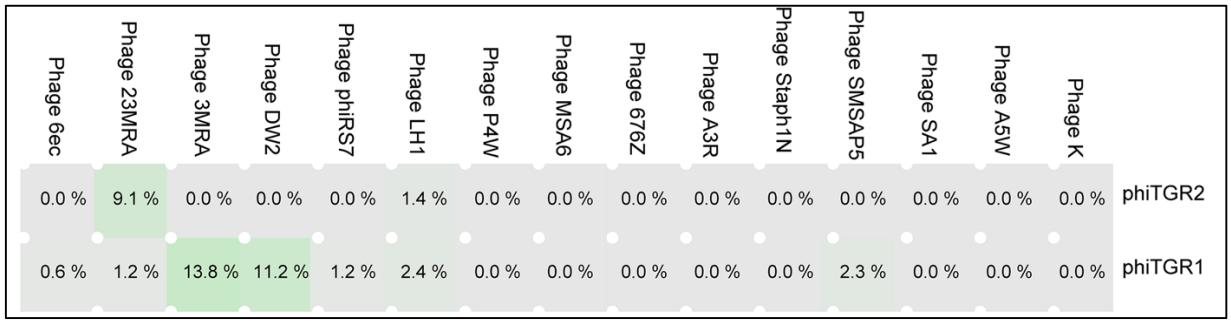

Phage 6ec	Phage 23MRA	Phage 3MRA	Phage DW2	Phage phiRS7	Phage LH1	Phage P4W	Phage MSA6	Phage 676Z	Phage A3R	Phage Staph1N	Phage SMSAP5	Phage SA1	Phage A5W	Phage K	
0.0 %	9.1 %	0.0 %	0.0 %	0.0 %	1.4 %	0.0 %	0.0 %	0.0 %	0.0 %	0.0 %	0.0 %	0.0 %	0.0 %	0.0 %	phiTGR2
0.6 %	1.2 %	13.8 %	11.2 %	1.2 %	2.4 %	0.0 %	0.0 %	0.0 %	0.0 %	0.0 %	2.3 %	0.0 %	0.0 %	0.0 %	phiTGR1

Figure S.II. Homology of *Staphylococcal* Phage Proteomes to the Tager 104 Prophages. Complete genome sequences were obtained from GenBank for *Staphylococcal* phages and protein content was predicted using saco_convert on CMG-Biotools 4.3.24. The lists of prophage-encoded proteins for φTGR1 and φTGR2 were obtained from IslandViewer 3. These lists were submitted to BLAST matrix construction on the CMG-Biotools system.

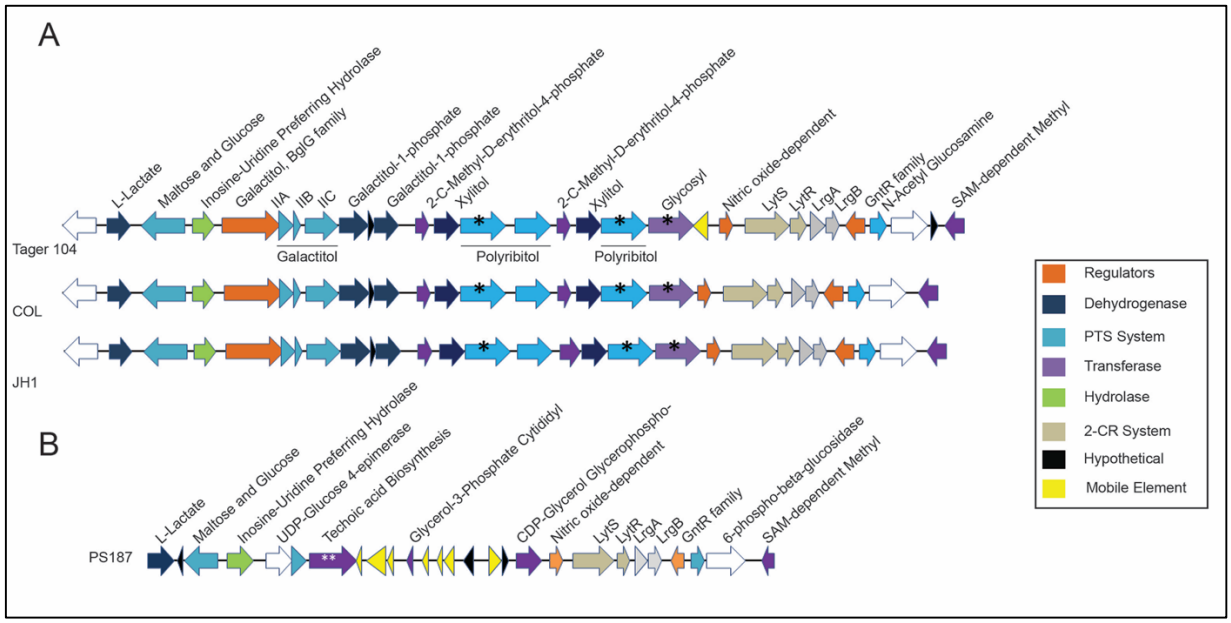

Figure S.III. Homologous Teichoic Acid Biosynthesis Genes in *S. aureus* Indicate Potential Bacteriophage Interactions. Teichoic acid structure may serve as the mechanism by which phages can recognize and transfer genomic elements. Therefore, investigation of the Tager 104 teichoic acid gene cluster revealed homology to the COL and JH1 strains, confirming the potential of phage-mediated acquisition of genomic elements to radiate into modern clinical strains. Putative proteins are indicated with an asterisk (*). The teichoic acid biosynthesis gene for PS187, which shows homology to transferase genes, is indicated with a double asterisk (**).

References

1. Iida, N., et al., *Commensal bacteria control cancer response to therapy by modulating the tumor microenvironment.* Science, 2013. **342**(6161): p. 967-70.
2. Trinchieri, G., *Cancer Immunity: Lessons From Infectious Diseases.* J Infect Dis, 2015. **212 Suppl 1**: p. S67-73.
3. Glickman, M.S. and C.L. Sawyers, *Converting cancer therapies into cures: lessons from infectious diseases.* Cell, 2012. **148**(6): p. 1089-98.
4. Goldszmid, R.S., A. Dzutsev, and G. Trinchieri, *Host immune response to infection and cancer: unexpected commonalities.* Cell Host Microbe, 2014. **15**(3): p. 295-305.
5. McGonigle, P. and B. Ruggeri, *Animal models of human disease: challenges in enabling translation.* Biochem Pharmacol, 2014. **87**(1): p. 162-71.
6. Ledford, H., *Translational research: 4 ways to fix the clinical trial.* Nature, 2011. **477**(7366): p. 526-8.
7. Mak, I.W., N. Evaniew, and M. Ghert, *Lost in translation: animal models and clinical trials in cancer treatment.* Am J Transl Res, 2014. **6**(2): p. 114-8.
8. Friedrich, R., et al., *Staphylocoagulase is a prototype for the mechanism of cofactor-induced zymogen activation.* Nature, 2003. **425**(6957): p. 535-9.
9. Baba, T., et al., *Genome sequence of Staphylococcus aureus strain Newman and comparative analysis of staphylococcal genomes: polymorphism and evolution of two major pathogenicity islands.* J Bacteriol, 2008. **190**(1): p. 300-10.
10. Russell, W.M.S. and R.L. Burch, *The principles of humane experimental technique*. 1959, London,: Methuen. 238 p.

11. Herron-Olson, L., et al., *Molecular correlates of host specialization in Staphylococcus aureus.* PLoS One, 2007. **2**(10): p. e1120.

12. Koda-Kimble, M.A. and B.K. Alldredge, *Applied therapeutics : the clinical use of drugs*. 10th ed. 2013, Philadelphia: Wolters Kluwer/Lippincott Williams & Wilkins. xxxix, 2519 p.

13. Zhu, G., et al., *Secretory phospholipase A(2) responsive liposomes.* J Pharm Sci, 2011. **100**(8): p. 3146-59.

14. Gabizon, A., *Liposomes as a drug delivery system in cancer chemotherapy.* Horiz Biochem Biophys, 1989. **9**: p. 185-211.

15. Weinstein, J.N. and L.D. Leserman, *Liposomes as drug carriers in cancer chemotherapy.* Pharmacol Ther, 1984. **24**(2): p. 207-33.

16. Egler, R.A., S.P. Ahuja, and Y. Matloub, *L-asparaginase in the treatment of patients with acute lymphoblastic leukemia.* J Pharmacol Pharmacother, 2016. **7**(2): p. 62-71.

17. Blair, J.M., et al., *Molecular mechanisms of antibiotic resistance.* Nat Rev Microbiol, 2015. **13**(1): p. 42-51.

18. Redgrave, L.S., et al., *Fluoroquinolone resistance: mechanisms, impact on bacteria, and role in evolutionary success.* Trends Microbiol, 2014. **22**(8): p. 438-45.

19. Bellamy, W.T., *P-glycoproteins and multidrug resistance.* Annu Rev Pharmacol Toxicol, 1996. **36**: p. 161-83.

20. Nielsen, D., C. Maare, and T. Skovsgaard, *Cellular resistance to anthracyclines.* Gen Pharmacol, 1996. **27**(2): p. 251-5.

21. Katz, M.L., et al., *Where have all the antibiotic patents gone?* Nat Biotechnol, 2006. **24**(12): p. 1529-31.

22. CDC, *Antibiotic resistance threats in the United States, 2013*. 2013: p. 77-78.

23. Appelbaum, P.C., *2012 and beyond: potential for the start of a second pre-antibiotic era?* J Antimicrob Chemother, 2012. **67**(9): p. 2062-8.

24. Issacson J, C.B., *Report.* Mouse News Lett, 1962. **27**(31).

25. Ito, R., et al., *Current advances in humanized mouse models.* Cell Mol Immunol, 2012. **9**(3): p. 208-14.

26. Shultz, L.D., F. Ishikawa, and D.L. Greiner, *Humanized mice in translational biomedical research.* Nat Rev Immunol, 2007. **7**(2): p. 118-30.

27. Flanagan, S.P., *'Nude', a new hairless gene with pleiotropic effects in the mouse.* Genet Res, 1966. **8**(3): p. 295-309.

28. Bosma, G.C., R.P. Custer, and M.J. Bosma, *A severe combined immunodeficiency mutation in the mouse.* Nature, 1983. **301**(5900): p. 527-30.

29. McCune, J., et al., *The SCID-hu mouse: a small animal model for HIV infection and pathogenesis.* Annu Rev Immunol, 1991. **9**: p. 399-429.

30. Zhang, L., et al., *Current humanized mouse models for studying human immunology and HIV-1 immuno-pathogenesis.* Sci China Life Sci, 2010. **53**(2): p. 195-203.

31. Koyanagi, Y., et al., *Humanized mice for human retrovirus infection.* Curr Top Microbiol Immunol, 2008. **324**: p. 133-48.

32. Heuts, F., et al., *CD4+ cell-dependent granuloma formation in humanized mice infected with mycobacteria.* Proc Natl Acad Sci U S A, 2013. **110**(16): p. 6482-7.

33. Calderon, V.E., et al., *A humanized mouse model of tuberculosis.* PLoS One, 2013. **8**(5): p. e63331.

34. Song, J., et al., *A mouse model for the human pathogen Salmonella typhi.* Cell Host Microbe, 2010. **8**(4): p. 369-76.

35. Libby, S.J., et al., *Humanized nonobese diabetic-scid IL2rgammanull mice are susceptible to lethal Salmonella Typhi infection.* Proc Natl Acad Sci U S A, 2010. **107**(35): p. 15589-94.

36. Mian, M.F., et al., *Humanized mice for Salmonella typhi infection: new tools for an old problem.* Virulence, 2011. **2**(3): p. 248-52.

37. Leung, C., et al., *Infectious diseases in humanized mice.* Eur J Immunol, 2013. **43**(9): p. 2246-54.

38. Kerbel, R.S., *Human tumor xenografts as predictive preclinical models for anticancer drug activity in humans: better than commonly perceived-but they can be improved.* Cancer Biol Ther, 2003. **2**(4 Suppl 1): p. S134-9.

39. Richmond, A. and Y. Su, *Mouse xenograft models vs GEM models for human cancer therapeutics.* Dis Model Mech, 2008. **1**(2-3): p. 78-82.

40. Panizzi, P., et al., *In vivo detection of Staphylococcus aureus endocarditis by targeting pathogen-specific prothrombin activation.* Nature Medicine. Sep2011, 2011. **17**(9): p. 1142.

41. Chiavolini, D., G. Pozzi, and S. Ricci, *Animal models of Streptococcus pneumoniae disease.* Clin Microbiol Rev, 2008. **21**(4): p. 666-85.

42. Tseng, C.W., et al., *Subcutaneous infection of methicillin resistant Staphylococcus aureus (MRSA).* J Vis Exp, 2011(48).

43. Buras, J.A., B. Holzmann, and M. Sitkovsky, *Animal models of sepsis: setting the stage.* Nat Rev Drug Discov, 2005. **4**(10): p. 854-65.

44. Saito, M., et al., *Delayed onset of systemic bacterial dissemination and subsequent death in mice injected intramuscularly with Streptococcus pyogenes strains.* Microbiol Immunol, 2001. **45**(11): p. 777-86.

45. Euhus, D.M., et al., *Tumor measurement in the nude mouse.* J Surg Oncol, 1986. **31**(4): p. 229-34.

46. Puaux, A.L., et al., *A comparison of imaging techniques to monitor tumor growth and cancer progression in living animals.* Int J Mol Imaging, 2011. **2011**: p. 321538.

47. Ayers, G.D., et al., *Volume of preclinical xenograft tumors is more accurately assessed by ultrasound imaging than manual caliper measurements.* J Ultrasound Med, 2010. **29**(6): p. 891-901.

48. Cassat, J.E., et al., *A secreted bacterial protease tailors the Staphylococcus aureus virulence repertoire to modulate bone remodeling during osteomyelitis.* Cell Host Microbe, 2013. **13**(6): p. 759-72.

49. Razansky, D., A. Buehler, and V. Ntziachristos, *Volumetric real-time multispectral optoacoustic tomography of biomarkers.* Nat Protoc, 2011. **6**(8): p. 1121-9.

50. Klerk, C.P., et al., *Validity of bioluminescence measurements for noninvasive in vivo imaging of tumor load in small animals.* Biotechniques, 2007. **43**(1 Suppl): p. 7-13, 30.

51. Keyaerts, M., V. Caveliers, and T. Lahoutte, *Bioluminescence imaging: looking beyond the light.* Trends Mol Med, 2012. **18**(3): p. 164-72.

52. Kirschmann, D.A., et al., *Molecular pathways: vasculogenic mimicry in tumor cells: diagnostic and therapeutic implications.* Clin Cancer Res, 2012. **18**(10): p. 2726-32.

53. Maniotis, A.J., et al., *Vascular channel formation by human melanoma cells in vivo and in vitro: vasculogenic mimicry.* Am J Pathol, 1999. **155**(3): p. 739-52.

54. Seftor, R.E., et al., *Tumor cell vasculogenic mimicry: from controversy to therapeutic promise.* Am J Pathol, 2012. **181**(4): p. 1115-25.

55. Jacques, S.L., *Optical properties of biological tissues: a review.* Phys Med Biol, 2013. **58**(11): p. R37-61.

56. Tomayko, M.M. and C.P. Reynolds, *Determination of subcutaneous tumor size in athymic (nude) mice.* Cancer Chemother Pharmacol, 1989. **24**(3): p. 148-54.

57. Jensen, M.M., et al., *Tumor volume in subcutaneous mouse xenografts measured by microCT is more accurate and reproducible than determined by 18F-FDG-microPET or external caliper.* BMC Med Imaging, 2008. **8**: p. 16.

58. Mazurchuk, R., D. Glaves, and D. Raghavan, *Magnetic resonance imaging of response to chemotherapy in orthotopic xenografts of human bladder cancer.* Clin Cancer Res, 1997. **3**(9): p. 1635-41.

59. Bouchard, R., O. Sahin, and S. Emelianov, *Ultrasound-guided photoacoustic imaging: current state and future development.* IEEE Trans Ultrason Ferroelectr Freq Control, 2014. **61**(3): p. 450-66.

60. Vinegoni, C., et al., *Imaging of molecular probe activity with Born-normalized fluorescence optical projection tomography.* Opt Lett, 2010. **35**(7): p. 1088-90.

61. Pizzonia, J., et al., *Multimodality animal rotation imaging system (Mars) for in vivo detection of intraperitoneal tumors.* Am J Reprod Immunol, 2012. **67**(1): p. 84-90.

62. Chu, Z., et al., *In vivo optical imaging of brain tumors and arthritis using fluorescent SapC-DOPS nanovesicles.* J Vis Exp, 2014(87).

63. Grice, E.A. and J.A. Segre, *The skin microbiome.* Nat Rev Microbiol, 2011. **9**(4): p. 244-53.

64. Ki, V. and C. Rotstein, *Bacterial skin and soft tissue infections in adults: A review of their epidemiology, pathogenesis, diagnosis, treatment and site of care.* Can J Infect Dis Med Microbiol, 2008. **19**(2): p. 173-84.

65. Iwatsuki, K., et al., *Staphylococcal cutaneous infections: Invasion, evasion and aggression.* J Dermatol Sci, 2006. **42**(3): p. 203-214.

66. Delgado, S., et al., *Characterization of Staphylococcus aureus strains involved in human and bovine mastitis.* FEMS Immunol Med Microbiol, 2011. **62**(2): p. 225-35.

67. Jones, G.M.B., T.L., Jr, *Understanding the Basics of Mastitis.* Virginia Cooperative Extension, 2009(Publication 404-233): p. 5.

68. Fowler, V.G., et al., *Staphylococcus aureus endocarditis - A consequence of medical progress.* Jama-Journal of the American Medical Association, 2005. **293**(24): p. 3012-3021.

69. Panizzi, P., et al., *In vivo detection of Staphylococcus aureus endocarditis by targeting pathogen-specific prothrombin activation.* Nat Med, 2011. **17**(9): p. 1142-U153.

70. Davis, R.W., et al., *Complete genome of Staphylococcus aureus Tager 104 provides evidence of its relation to modern systemic hospital-acquired strains.* BMC Genomics, 2016. **17**.

71. FDA, *Guidance for Industry.*

72. Wardyn, S.E., et al., *Swine Farming Is a Risk Factor for Infection With and High Prevalence of Carriage of Multidrug-Resistant Staphylococcus aureus.* Clin Infect Dis, 2015. **61**(1): p. 59-66.

73. Smith, T.C., et al., *Methicillin-resistant Staphylococcus aureus in pigs and farm workers on conventional and antibiotic-free swine farms in the USA.* PLoS One, 2013. **8**(5): p. e63704.

74. Oppliger, A., et al., *Antimicrobial resistance of Staphylococcus aureus strains acquired by pig farmers from pigs.* Appl Environ Microbiol, 2012. **78**(22): p. 8010-4.

75. Denis, O., et al., *Methicillin-resistant Staphylococcus aureus ST398 in swine farm personnel, Belgium.* Emerg Infect Dis, 2009. **15**(7): p. 1098-101.

76. Voss, A., et al., *Methicillin-resistant Staphylococcus aureus in pig farming.* Emerg Infect Dis, 2005. **11**(12): p. 1965-6.

77. Chowdhury, S.P., et al., *Biocontrol mechanism by root-associated Bacillus amyloliquefaciens FZB42 - a review.* Front Microbiol, 2015. **6**: p. 780.

78. Wu, L.M., et al., *Novel Routes for Improving Biocontrol Activity of Bacillus Based Bioinoculants.* Front Microbiol, 2015. **6**.

79. Ran, C., et al., *Identification of Bacillus Strains for Biological Control of Catfish Pathogens.* PLoS One, 2012. **7**(9).

80. Hamdache, A., et al., *Non-peptide metabolites from the genus Bacillus.* J Nat Prod, 2011. **74**(4): p. 893-9.

81. Stein, T., *Bacillus subtilis antibiotics: structures, syntheses and specific functions.* Mol Microbiol, 2005. **56**(4): p. 845-57.

82. Mannanov, R.N., *The use of natural bio-agents for the control of cotton phytopathogens.* Meded Rijksuniv Gent Fak Landbouwkd Toegep Biol Wet, 2001. **66**(3a): p. 183-6.

83. Chen, X.H., et al., *More than anticipated - production of antibiotics and other secondary metabolites by Bacillus amyloliquefaciens FZB42.* J Mol Microbiol Biotechnol, 2009. **16**(1-2): p. 14-24.

84. Ongena, M. and P. Jacques, *Bacillus lipopeptides: versatile weapons for plant disease biocontrol.* Trends Microbiol, 2008. **16**(3): p. 115-25.

85. Cook, R.J., et al., *Molecular mechanisms of defense by rhizobacteria against root disease.* Proc Natl Acad Sci U S A, 1995. **92**(10): p. 4197-201.

86. Kloepper, J.W., et al., *Enhanced plant growth by siderophores produced by plant growth-promoting rhizobacteria.* Nature, 1980. **286**(5776): p. 885-886.

87. Ahmed, S.T., et al., *Effects of Bacillus amyloliquefaciens as a probiotic strain on growth performance, cecal microflora, and fecal noxious gas emissions of broiler chickens.* Poult Sci, 2014. **93**(8): p. 1963-71.

88. Gonzalez-Ortiz, G., et al., *Effects of dietary supplementation of Bacillus amyloliquefaciens CECT 5940 and Enterococcus faecium CECT 4515 in adult healthy dogs.* Arch Anim Nutr, 2013. **67**(5): p. 406-15.

89. Casula, G. and S.M. Cutting, *Bacillus probiotics: spore germination in the gastrointestinal tract.* Appl Environ Microbiol, 2002. **68**(5): p. 2344-52.

90. Krober, M., et al., *Effect of the strain Bacillus amyloliquefaciens FZB42 on the microbial community in the rhizosphere of lettuce under field conditions analyzed by whole metagenome sequencing.* Front Microbiol, 2014. **5**: p. 252.

91. Lee, S.Y., et al., *Draft genome sequence of the biocontrol bacterium Bacillus amyloliquefaciens strain M27.* J Bacteriol, 2012. **194**(24): p. 6934-5.

92. Geeraerts, S., et al., *Bacillus amyloliquefaciens as prophylactic treatment for Clostridium difficile-associated disease in a mouse model.* J Gastroenterol Hepatol, 2015. **30**(8): p. 1275-80.

93. Nasrin, s., *Discovery and Characterization of Antibacterial Compounds Expressed by Soil Microorganisms using Culture-Dependent and -Independent Approaches*, in *Biological Sciences*. 2015, Auburn University. p. 188.

94. Ravu, R.R., et al., *Bacillusin A, an Antibacterial Macrodiolide from Bacillus amyloliquefaciens AP183.* J Nat Prod, 2015. **78**(4): p. 924-928.

95. DeSantis, T.Z., et al., *Greengenes, a chimera-checked 16S rRNA gene database and workbench compatible with ARB.* Appl Environ Microbiol, 2006. **72**(7): p. 5069-72.

96. Mantelin, S., et al., *Emended description of the genus Phyllobacterium and description of four novel species associated with plant roots: Phyllobacterium bourgognense sp. nov., Phyllobacterium ifriqiyense sp. nov., Phyllobacterium leguminum sp. nov. and Phyllobacterium brassicacearum sp. nov.* Int J Syst Evol Microbiol, 2006. **56**(Pt 4): p. 827-39.

97. Cohen, P.R., *Community-acquired methicillin-resistant Staphylococcus aureus skin infections: a review of epidemiology, clinical features, management, and prevention.* Int J Dermatol, 2007. **46**(1): p. 1-11.

98. Avni, T., et al., *Prophylactic antibiotics for burns patients: systematic review and meta-analysis.* BMJ, 2010. **340**: p. c241.

99. Tager, M. and H.B. Hales, *Quantitative coagulase and toxin production by staphylococci in relation to the clinical source of the organisms.* Yale J Biol Med, 1947. **20**(1): p. 41-9.

100. Guinane, C.M., et al., *Evolutionary genomics of Staphylococcus aureus reveals insights into the origin and molecular basis of ruminant host adaptation.* Genome Biol Evol, 2010. **2**: p. 454-66.

101. Schijffelen, M.J., et al., *Whole genome analysis of a livestock-associated methicillin-resistant Staphylococcus aureus ST398 isolate from a case of human endocarditis.* BMC Genomics, 2010. **11**: p. 376.

102. Lowder, B.V., et al., *Recent human-to-poultry host jump, adaptation, and pandemic spread of Staphylococcus aureus.* Proc Natl Acad Sci U S A, 2009. **106**(46): p. 19545-50.

103. Haraldsson, I. and P. Jonsson, *Histopathology and pathogenesis of mouse mastitis induced with Staphylococcus aureus mutants.* J Comp Pathol, 1984. **94**(2): p. 183-96.

104. Jonsson, P., et al., *Virulence of Staphylococcus aureus in a mouse mastitis model: studies of alpha hemolysin, coagulase, and protein A as possible virulence determinants with protoplast fusion and gene cloning.* Infect Immun, 1985. **49**(3): p. 765-9.

105. Holden, M.T., et al., *Genome sequence of a recently emerged, highly transmissible, multi-antibiotic- and antiseptic-resistant variant of methicillin-resistant Staphylococcus aureus, sequence type 239 (TW).* J Bacteriol, 2010. **192**(3): p. 888-92.

106. Altman, D.R., et al., *Transmission of methicillin-resistant Staphylococcus aureus via deceased donor liver transplantation confirmed by whole genome sequencing.* Am J Transplant, 2014. **14**(11): p. 2640-4.

107. Durack, D.T., *Infective and Noninfective Endocarditis*. The Heart: Arteries and Veins, ed. J.w. Hurst, Sonnenblick, E.H., Wenger, N.K. Vol. 63. 2001, New York: McGraw-Hill.

108. Korzeniowski, O.K., D., *Infective Endocarditis*. Heart Disease. A Textbook of Cardiovascular Medicine, ed. E. Braunwald. 1992, Philadelphia: W.B. Saunders.

109. Sawai, T., et al., *Role of coagulase in a murine model of hematogenous pulmonary infection induced by intravenous injection of Staphylococcus aureus enmeshed in agar beads.* Infect Immun, 1997. **65**(2): p. 466-71.

110. McAdow, M., et al., *Preventing Staphylococcus aureus sepsis through the inhibition of its agglutination in blood.* PLoS Pathog, 2011. **7**(10): p. e1002307.

111. Chapman, G.H., et al., *Coagulase and Hemolysin Tests as Measures of the Pathogenicity of Staphylococci.* J Bacteriol, 1934. **28**(4): p. 343-63.

112. Panizzi, P., et al., *The staphylocoagulase family of zymogen activator and adhesion proteins.* Cell Mol Life Sci, 2004. **61**(22): p. 2793-8.

113. Kroh, H.K., P. Panizzi, and P.E. Bock, *Von Willebrand factor-binding protein is a hysteretic conformational activator of prothrombin.* Proc Natl Acad Sci U S A, 2009. **106**(19): p. 7786-91.

114. Wood, J.P., et al., *Prothrombin activation on the activated platelet surface optimizes expression of procoagulant activity.* Blood, 2011. **117**(5): p. 1710-8.

115. Krishnaswamy, S., *The transition of prothrombin to thrombin.* J Thromb Haemost, 2013. **11 Suppl 1**: p. 265-76.

116. Khan, A.R. and M.N. James, *Molecular mechanisms for the conversion of zymogens to active proteolytic enzymes.* Protein Sci, 1998. **7**(4): p. 815-36.

117. Bode, W. and R. Huber, *Induction of the bovine trypsinogen-trypsin transition by peptides sequentially similar to the N-terminus of trypsin.* FEBS Lett, 1976. **68**(2): p. 231-6.

118. Panizzi, P., et al., *Fibrinogen substrate recognition by staphylocoagulase.(pro)thrombin complexes.* J Biol Chem, 2006. **281**(2): p. 1179-87.

119. Kroh, H.K., et al., *Active site-labeled prothrombin inhibits prothrombinase in vitro and thrombosis in vivo.* J Biol Chem, 2011. **286**(26): p. 23345-56.

120. Panizzi, P., et al., *Binding of the COOH-terminal lysine residue of streptokinase to plasmin(ogen) kringles enhances formation of the streptokinase.plasmin(ogen) catalytic complexes.* J Biol Chem, 2006. **281**(37): p. 26774-8.

121. Chen, C., et al., *Secreted proteases control autolysin-mediated biofilm growth of Staphylococcus aureus.* J Biol Chem, 2013.

122. Bjerketorp, J., K. Jacobsson, and L. Frykberg, *The von Willebrand factor-binding protein (vWbp) of Staphylococcus aureus is a coagulase.* FEMS Microbiol Lett, 2004. **234**(2): p. 309-14.

123. Bjerketorp, J., et al., *A novel von Willebrand factor binding protein expressed by Staphylococcus aureus.* Microbiology, 2002. **148**(Pt 7): p. 2037-44.

124. Peter, P., et al., *Staphylocoagulase.* 2013: p. 575-590.

125. Baddour, L.M., *A trojan horse mechanism in the pathogenesis of infective endocarditis: a hypothesis.* Zentralbl Bakteriol, 1996. **283**(3): p. 266-70.

126. Baddour, L.M., et al., *Virulence of coagulase-deficient mutants of Staphylococcus aureus in experimental endocarditis.* J Med Microbiol, 1994. **41**(4): p. 259-63.

127. Moreillon, P., et al., *Role of Staphylococcus aureus coagulase and clumping factor in pathogenesis of experimental endocarditis.* Infect Immun, 1995. **63**(12): p. 4738-43.

128. Stutzmann Meier, P., et al., *Study of Staphylococcus aureus pathogenic genes by transfer and expression in the less virulent organism Streptococcus gordonii.* Infect Immun, 2001. **69**(2): p. 657-64.

129. Raus, J. and D.N. Love, *Comparison of the affinities to bovine and human prothrombin of the staphylocoagulases from Staphylococcus intermedius and Staphylococcus aureus of animal origin.* J Clin Microbiol, 1991. **29**(3): p. 570-2.

130. Loeb, J., *The influence of certain bacteria on the coagulation of the blood.* J. Med. Res., 1908. **10**: p. 407-419.

131. Bush, L.A., R.W. Nelson, and E. Di Cera, *Murine thrombin lacks Na+ activation but retains high catalytic activity.* J Biol Chem, 2006. **281**(11): p. 7183-8.

132. Friedrich, R., et al., *Structural basis for reduced staphylocoagulase-mediated bovine prothrombin activation.* J Biol Chem, 2006. **281**(2): p. 1188-95.

133. Fenton, J.W., 2nd, M.J. Fasco, and A.B. Stackrow, *Human thrombins. Production, evaluation, and properties of alpha-thrombin.* J Biol Chem, 1977. **252**(11): p. 3587-98.

134. Mann, K.G., et al., *Prothrombin.* Methods Enzymol, 1981. **80 Pt C**: p. 286-302.

135. Pace, C.N., et al., *How to measure and predict the molar absorption coefficient of a protein.* Protein Sci, 1995. **4**(11): p. 2411-23.

136. Cheng, A.G., et al., *Contribution of coagulases towards Staphylococcus aureus disease and protective immunity.* PLoS Pathog, 2010. **6**(8): p. e1001036.

137. Vesth, T., et al., *CMG-biotools, a free workbench for basic comparative microbial genomics.* PLoS One, 2013. **8**(4): p. e60120.

138. Phan, J., et al., *Structural basis for the substrate specificity of tobacco etch virus protease.* J Biol Chem, 2002. **277**(52): p. 50564-72.

139. De Cristofaro, R. and E. Di Cera, *Phenomenological analysis of the clotting curve.* J Protein Chem, 1991. **10**(5): p. 455-68.

140. Golding, G.R., et al., *whole-genome sequence of livestock-associated st398 methicillin-resistant staphylococcus aureus Isolated from Humans in Canada.* J Bacteriol, 2012. **194**(23): p. 6627-8.

141. Zubair, S., et al., *Complete genome sequence of Staphylococcus aureus, strain ILRI_Eymole1/1, isolated from a Kenyan dromedary camel.* Stand Genomic Sci, 2015. **10**: p. 109.

142. Garcia-Alvarez, L., et al., *Meticillin-resistant Staphylococcus aureus with a novel mecA homologue in human and bovine populations in the UK and Denmark: a descriptive study.* Lancet Infect Dis, 2011. **11**(8): p. 595-603.

143. Herron, L.L., et al., *Genome sequence survey identifies unique sequences and key virulence genes with unusual rates of amino Acid substitution in bovine Staphylococcus aureus.* Infect Immun, 2002. **70**(7): p. 3978-81.

144. Davis, R., et al., *Complete Genome Sequence of Staphylococcus aureus Tager 104, a Sequence Type 49 Ancestor.* Genome Announc, 2013. **1**(5).

145. Prevention, C.f.D.C.a., *Antibiotic Resistance Threats in the United States, 2013*. 2013. p. 1-114.

146. Fowler, V.G., Jr., et al., *Staphylococcus aureus endocarditis: a consequence of medical progress.* JAMA, 2005. **293**(24): p. 3012-21.

147. Malachowa, N. and F.R. DeLeo, *Mobile genetic elements of Staphylococcus aureus.* Cell Mol Life Sci, 2010. **67**(18): p. 3057-71.

148. Baba, T., et al., *Genome and virulence determinants of high virulence community-acquired MRSA.* Lancet, 2002. **359**(9320): p. 1819-27.

149. Brussow, H., C. Canchaya, and W.D. Hardt, *Phages and the evolution of bacterial pathogens: from genomic rearrangements to lysogenic conversion.* Microbiol Mol Biol Rev, 2004. **68**(3): p. 560-602, table of contents.

150. Plano, L.R., *Staphylococcus aureus exfoliative toxins: how they cause disease.* J Invest Dermatol, 2004. **122**(5): p. 1070-7.

151. Diep, B.A., et al., *Complete genome sequence of USA300, an epidemic clone of community-acquired meticillin-resistant Staphylococcus aureus.* Lancet, 2006. **367**(9512): p. 731-9.

152. Kuroda, M., et al., *Whole genome sequencing of meticillin-resistant Staphylococcus aureus.* Lancet, 2001. **357**(9264): p. 1225-40.

153. Tager, M.H., B., *Quantitative Coagulase and Toxin Production by Staphylococcus in Relation to the Clinical Source of the Organisms.* Yale J Biol Med., 1947. **20**(1): p. 41-49.

154. Tager, M., *Studies on the coagulase-reacting factor; the reaction of staphylocoagulase with the components of human plasma.* Yale J Biol Med, 1948. **20**(4): p. 369-80.

155. Tager, M. and M.C. Drummond, *Staphylocoagulase.* Ann N Y Acad Sci, 1965. **128**(1): p. 92-111.

156. Tager, M., *Concentration, partial purification, properties, and nature of staphylocoagulase.* Yale J Biol Med, 1948. **20**(5): p. 487-501.

157. Tager, M. and A.L. Lodge, *Influence of the physiological blood clotting process on the coagulation of blood by staphylocoagulase.* J Exp Med, 1951. **94**(1): p. 73-85.

158. Tager, M. and A.L. Lodge, *Changes in the properties of the coagulase-reacting factor of plasma after separation from prothrombin by Seitz filtration.* J Immunol, 1951. **67**(1): p. 63-9.

159. Panizzi, P., et al., *Novel fluorescent prothrombin analogs as probes of staphylocoagulase-prothrombin interactions.* J Biol Chem, 2006. **281**(2): p. 1169-78.

160. Chin, C.S., et al., *Nonhybrid, finished microbial genome assemblies from long-read SMRT sequencing data.* Nat Methods, 2013. **10**(6): p. 563-9.

161. Hunt, M., et al., *A comprehensive evaluation of assembly scaffolding tools.* Genome Biol, 2014. **15**(3): p. R42.

162. Aziz, R.K., et al., *The RAST Server: rapid annotations using subsystems technology.* BMC Genomics, 2008. **9**: p. 75.

163. Brettin, T., et al., *RASTtk: a modular and extensible implementation of the RAST algorithm for building custom annotation pipelines and annotating batches of genomes.* Sci Rep, 2015. **5**: p. 8365.

164. Overbeek, R., et al., *The SEED and the Rapid Annotation of microbial genomes using Subsystems Technology (RAST).* Nucleic Acids Res, 2014. **42**(Database issue): p. D206-14.

165. Nurk, S., et al., *Assembling single-cell genomes and mini-metagenomes from chimeric MDA products.* J Comput Biol, 2013. **20**(10): p. 714-37.

166. Kurtz, S., et al., *Versatile and open software for comparing large genomes.* Genome Biol, 2004. **5**(2): p. R12.

167. Darling, A.E., B. Mau, and N.T. Perna, *progressiveMauve: Multiple Genome Alignment with Gene Gain, Loss and Rearrangement.* PLoS One, 2010. **5**(6): p. e11147.

168. Alikhan, N.F., et al., *BLAST Ring Image Generator (BRIG): simple prokaryote genome comparisons.* BMC Genomics, 2011. **12**: p. 402.

169. Panizzi, P., J.R. Stone, and M. Nahrendorf, *Molecular Imaging of Endocarditis.* Journal of Nuclear Cardiology, 2014.

170. Feil, E.J., et al., *eBURST: inferring patterns of evolutionary descent among clusters of related bacterial genotypes from multilocus sequence typing data.* J Bacteriol, 2004. **186**(5): p. 1518-30.

171. Vann, J.M. and R.A. Proctor, *Ingestion of Staphylococcus aureus by bovine endothelial cells results in time- and inoculum-dependent damage to endothelial cell monolayers.* Infect Immun, 1987. **55**(9): p. 2155-63.

172. Powers, M.E. and J. Bubeck Wardenburg, *Igniting the fire: Staphylococcus aureus virulence factors in the pathogenesis of sepsis.* PLoS Pathog, 2014. **10**(2): p. e1003871.

173. Kos, V.N., et al., *Comparative genomics of vancomycin-resistant Staphylococcus aureus strains and their positions within the clade most commonly associated with Methicillin-resistant S. aureus hospital-acquired infection in the United States.* MBio, 2012. **3**(3).

174. Howden, B.P., et al., *Reduced vancomycin susceptibility in Staphylococcus aureus, including vancomycin-intermediate and heterogeneous vancomycin-intermediate strains: resistance mechanisms, laboratory detection, and clinical implications.* Clin Microbiol Rev, 2010. **23**(1): p. 99-139.

175. Centers for Disease, C. and Prevention, *Four pediatric deaths from community-acquired methicillin-resistant Staphylococcus aureus - Minnesota and North Dakota, 1997-1999.* MMWR Morb Mortal Wkly Rep, 1999. **48**(32): p. 707-10.

176. Panizzi, P., Nahrendorf M, Figueiredo JL, Panizzi JR, Marinelli B, Iwamoto Y, Keliher E, Maddur AA, Waterman P, Kroh HK, Leuschner F, Aikawa E, Swirski FK, Pittet MJ, Hackeng TM, Fuenes-Prior P, Schneedwind O, Bock PE, and Weissleder R. , *In Vitro*

Detection of Staphylococcus aureus Endocarditis by Targeting Pathogen-Specific Prothrombin Activation. Nature Medicine, 2011. **17**(9): p. 1142-1146.

177. Woods, C.W., et al., *Endocarditis caused by Staphylococcus aureus with reduced susceptibility to vancomycin.* Clin Infect Dis, 2004. **38**(8): p. 1188-91.

178. Koren, S., et al., *Hybrid error correction and de novo assembly of single-molecule sequencing reads.* Nat Biotechnol, 2012. **30**(7): p. 693-700.

179. Benson, M.A., et al., *Evolution of hypervirulence by a MRSA clone through acquisition of a transposable element.* Mol Microbiol, 2014. **93**(4): p. 664-81.

180. Chen, C.J., et al., *Characterization and comparison of 2 distinct epidemic community-associated methicillin-resistant Staphylococcus aureus clones of ST59 lineage.* PLoS One, 2013. **8**(9): p. e63210.

181. Overesch, G., et al., *The increase of methicillin-resistant Staphylococcus aureus (MRSA) and the presence of an unusual sequence type ST49 in slaughter pigs in Switzerland.* BMC Vet Res, 2011. **7**: p. 30.

182. Paterson, G.K., et al., *The newly described mecA homologue, mecALGA251, is present in methicillin-resistant Staphylococcus aureus isolates from a diverse range of host species.* J Antimicrob Chemother, 2012. **67**(12): p. 2809-13.

183. Winstel, V., et al., *Wall teichoic acid structure governs horizontal gene transfer between major bacterial pathogens.* Nat Commun, 2013. **4**: p. 2345.

184. Nubel, U., et al., *A timescale for evolution, population expansion, and spatial spread of an emerging clone of methicillin-resistant Staphylococcus aureus.* PLoS Pathog, 2010. **6**(4): p. e1000855.

185. Stegger, M., et al., *Genome sequence of Staphylococcus aureus strain 11819-97, an ST80-IV European community-acquired methicillin-resistant isolate.* J Bacteriol, 2012. **194**(6): p. 1625-6.

186. Roberts, R.B., et al., *Molecular epidemiology of methicillin-resistant Staphylococcus aureus in 12 New York hospitals. MRSA Collaborative Study Group.* J Infect Dis, 1998. **178**(1): p. 164-71.

187. Parker, D., et al., *Genome Sequence of Bacterial Interference Strain Staphylococcus aureus 502A.* Genome Announc, 2014. **2**(2).

188. Fraunholz, M., et al., *Complete Genome Sequence of Staphylococcus aureus 6850, a Highly Cytotoxic and Clinically Virulent Methicillin-Sensitive Strain with Distant Relatedness to Prototype Strains.* Genome Announc, 2013. **1**(5).

189. Bhat, M., et al., *Staphylococcus aureus ST398, New York City and Dominican Republic.* Emerg Infect Dis, 2009. **15**(2): p. 285-7.

190. Uhlemann, A.C., et al., *Identification of a highly transmissible animal-independent Staphylococcus aureus ST398 clone with distinct genomic and cell adhesion properties.* MBio, 2012. **3**(2).

191. Treangen, T.J., et al., *Complete Genome Sequence of the Quality Control Strain Staphylococcus aureus subsp. aureus ATCC 25923.* Genome Announc, 2014. **2**(6).

192. Daum, L.T., et al., *Whole-Genome Sequence for Methicillin-Resistant Staphylococcus aureus Strain ATCC BAA-1680.* Genome Announc, 2015. **3**(2).

193. Qu, J.Q., et al., *Complete mitochondrial genome of Costaria costata shows conservative evolution in Laminariales.* Mitochondrial DNA, 2015. **26**(6): p. 919-20.

194. Planet, P.J., et al., *Parallel Epidemics of Community-Associated Methicillin-Resistant Staphylococcus aureus USA300 Infection in North and South America.* J Infect Dis, 2015. **212**(12): p. 1874-82.

195. Stegger, M., et al., *Genome Sequence of Staphylococcus aureus Strain CA-347, a USA600 Methicillin-Resistant Isolate.* Genome Announc, 2013. **1**(4).

196. Gill, S.R., et al., *Insights on evolution of virulence and resistance from the complete genome analysis of an early methicillin-resistant Staphylococcus aureus strain and a biofilm-producing methicillin-resistant Staphylococcus epidermidis strain.* J Bacteriol, 2005. **187**(7): p. 2426-38.

197. Shiroma, A., et al., *First Complete Genome Sequences of Staphylococcus aureus subsp. aureus Rosenbach 1884 (DSM 20231T), Determined by PacBio Single-Molecule Real-Time Technology.* Genome Announc, 2015. **3**(4).

198. Lindqvist, M., et al., *Detection and characterisation of SCCmec remnants in multiresistant methicillin-susceptible Staphylococcus aureus causing a clonal outbreak in a Swedish county.* Eur J Clin Microbiol Infect Dis, 2012. **31**(2): p. 141-7.

199. Ben Zakour, N.L., et al., *Genome-wide analysis of ruminant Staphylococcus aureus reveals diversification of the core genome.* J Bacteriol, 2008. **190**(19): p. 6302-17.

200. Sabirova, J.S., et al., *Complete Genome Sequences of Two Prolific Biofilm-Forming Staphylococcus aureus Isolates Belonging to USA300 and EMRSA-15 Clonal Lineages.* Genome Announc, 2014. **2**(3).

201. McCulloch, J.A., et al., *Complete Genome Sequence of Staphylococcus aureus FCFHV36, a Methicillin-Resistant Strain Heterogeneously Resistant to Vancomycin.* Genome Announc, 2015. **3**(4).

202. Lim, S., et al., *Comparative genomic analysis of Staphylococcus aureus FORC_001 and S. aureus MRSA252 reveals the characteristics of antibiotic resistance and virulence factors for human infection.* J Microbiol Biotechnol, 2015. **25**(1): p. 98-108.

203. Sabat, A.J., et al., *Whole-genome analysis of an oxacillin-susceptible CC80 mecA-positive Staphylococcus aureus clinical isolate: insights into the mechanisms of cryptic methicillin resistance.* J Antimicrob Chemother, 2015. **70**(11): p. 2956-64.

204. Holden, M.T., et al., *A genomic portrait of the emergence, evolution, and global spread of a methicillin-resistant Staphylococcus aureus pandemic.* Genome Res, 2013. **23**(4): p. 653-64.

205. Panesso, D., et al., *Methicillin-Susceptible, Vancomycin-Resistant Staphylococcus aureus, Brazil.* Emerg Infect Dis, 2015. **21**(10): p. 1844-8.

206. Sieradzki, K., et al., *Evolution of a vancomycin-intermediate Staphylococcus aureus strain in vivo: multiple changes in the antibiotic resistance phenotypes of a single lineage of methicillin-resistant S. aureus under the impact of antibiotics administered for chemotherapy.* J Clin Microbiol, 2003. **41**(4): p. 1687-93.

207. Howden, B.P., et al., *Complete genome sequence of Staphylococcus aureus strain JKD6008, an ST239 clone of methicillin-resistant Staphylococcus aureus with intermediate-level vancomycin resistance.* J Bacteriol, 2010. **192**(21): p. 5848-9.

208. Chua, K., et al., *Complete genome sequence of Staphylococcus aureus strain JKD6159, a unique Australian clone of ST93-IV community methicillin-resistant Staphylococcus aureus.* J Bacteriol, 2010. **192**(20): p. 5556-7.

209. Huang, T.W., et al., *Complete genome sequence of Staphylococcus aureus M013, a pvl-positive, ST59-SCCmec type V strain isolated in Taiwan.* J Bacteriol, 2012. **194**(5): p. 1256-7.

210. Holden, M.T., et al., *Complete genomes of two clinical Staphylococcus aureus strains: evidence for the rapid evolution of virulence and drug resistance.* Proc Natl Acad Sci U S A, 2004. **101**(26): p. 9786-91.

211. Holt, D.C., et al., *A very early-branching Staphylococcus aureus lineage lacking the carotenoid pigment staphyloxanthin.* Genome Biol Evol, 2011. **3**: p. 881-95.

212. Hiramatsu, K., et al., *Dissemination in Japanese hospitals of strains of Staphylococcus aureus heterogeneously resistant to vancomycin.* Lancet, 1997. **350**(9092): p. 1670-3.

213. Liu, C. and H.F. Chambers, *Staphylococcus aureus with heterogeneous resistance to vancomycin: epidemiology, clinical significance, and critical assessment of diagnostic methods.* Antimicrob Agents Chemother, 2003. **47**(10): p. 3040-5.

214. Herbert, S., et al., *Repair of global regulators in Staphylococcus aureus 8325 and comparative analysis with other clinical isolates.* Infect Immun, 2010. **78**(6): p. 2877-89.

215. Fitzgerald, J.R., et al., *Fine-structure molecular epidemiological analysis of Staphylococcus aureus recovered from cows.* Epidemiol Infect, 1997. **119**(2): p. 261-9.

216. Stevens, M.J., R. Stephan, and S. Johler, *Complete and Assembled Genome Sequence of Staphylococcus aureus RKI4, a Food-Poisoning Strain Exhibiting a Novel S. aureus Pathogenicity Island Carrying seb.* Genome Announc, 2015. **3**(4).

217. Qu, T., et al., *Whole genome analysis of a community-associated methicillin-resistant Staphylococcus aureus ST59 isolate from a case of human sepsis and severe pneumonia in China.* PLoS One, 2014. **9**(2): p. e89235.

218. Giraud, C., et al., *The C-terminal region of the RNA helicase CshA is required for the interaction with the degradosome and turnover of bulk RNA in the opportunistic pathogen Staphylococcus aureus.* RNA Biol, 2015. **12**(6): p. 658-74.

219. Vogel, V., et al., *Short term evolution of a highly transmissible methicillin-resistant Staphylococcus aureus clone (ST228) in a tertiary care hospital.* PLoS One, 2012. **7**(6): p. e38969.

220. Steinig, E.J., et al., *Single-molecule sequencing reveals the molecular basis of multidrug-resistance in ST772 methicillin-resistant Staphylococcus aureus.* BMC Genomics, 2015. **16**: p. 388.

221. Manoharan, A., et al., *An outbreak of post-partum breast abscesses in Mumbai, India caused by ST22-MRSA-IV: genetic characteristics and epidemiological implications.* Epidemiol Infect, 2012. **140**(10): p. 1809-12.

222. Li, Y., et al., *Complete genome sequence of Staphylococcus aureus T0131, an ST239-MRSA-SCCmec type III clone isolated in China.* J Bacteriol, 2011. **193**(13): p. 3411-2.

223. Harris, S.R., et al., *Evolution of MRSA during hospital transmission and intercontinental spread.* Science, 2010. **327**(5964): p. 469-74.

224. Johnson, R.C., et al., *Recurrent Methicillin-Resistant Staphylococcus aureus Cutaneous Abscesses and Selection of Reduced Chlorhexidine Susceptibility during Chlorhexidine Use.* J Clin Microbiol, 2015. **53**(11): p. 3677-82.

225. Diep, B.A., et al., *Emergence of multidrug-resistant, community-associated, methicillin-resistant Staphylococcus aureus clone USA300 in men who have sex with men.* Ann Intern Med, 2008. **148**(4): p. 249-57.

226. Highlander, S.K., et al., *Subtle genetic changes enhance virulence of methicillin resistant and sensitive Staphylococcus aureus.* BMC Microbiol, 2007. **7**: p. 99.

227. Gonzalez, B.E., et al., *Severe Staphylococcal sepsis in adolescents in the era of community-acquired methicillin-resistant Staphylococcus aureus.* Pediatrics, 2005. **115**(3): p. 642-8.

228. Schaaff, F., A. Reipert, and G. Bierbaum, *An elevated mutation frequency favors development of vancomycin resistance in Staphylococcus aureus.* Antimicrob Agents Chemother, 2002. **46**(11): p. 3540-8.

229. Chen, F.J., et al., *Complete Genome Sequence of Staphylococcus aureus Z172, a Vancomycin-Intermediate and Daptomycin-Nonsusceptible Methicillin-Resistant Strain Isolated in Taiwan.* Genome Announc, 2013. **1**(6).